University of Miami
Scholarly Repository

Open Access Dissertations | Electronic Theses and Dissertations

2016-04-22

Part 1: Lagrangian Coherent Structures in a Coastal Upwelling Envirnonment; Part 2: Near-Inertial Oscillations in the Northeastern Gulf of Mexico

Matthew Kenneth Gough
University of Miami, mgough@rsmas.miami.edu

Follow this and additional works at: https://scholarlyrepository.miami.edu/oa_dissertations

Recommended Citation
Gough, Matthew Kenneth, "Part 1: Lagrangian Coherent Structures in a Coastal Upwelling Envirnonment; Part 2: Near-Inertial Oscillations in the Northeastern Gulf of Mexico" (2016). *Open Access Dissertations*. 1612.
https://scholarlyrepository.miami.edu/oa_dissertations/1612

This Open access is brought to you for free and open access by the Electronic Theses and Dissertations at Scholarly Repository. It has been accepted for inclusion in Open Access Dissertations by an authorized administrator of Scholarly Repository. For more information, please contact repository.library@miami.edu.

UNIVERSITY OF MIAMI

PART 1: LAGRANGIAN COHERENT STRUCTURES IN A COASTAL UPWELLING ENVIRONMENT; PART 2: NEAR-INERTIAL OSCILLATIONS IN THE NORTHEASTERN GULF OF MEXICO

By

Matthew Kenneth Gough

A DISSERTATION

Submitted to the Faculty
of the University of Miami
in partial fulfillment of the requirements for
the degree of Doctor of Philosophy

Coral Gables, Florida

May 2016

©2016
Matthew Kenneth Gough
All Rights Reserved

UNIVERSITY OF MIAMI

A dissertation submitted in partial fulfillment of
the requirements for the degree of
Doctor of Philosophy

PART 1: LAGRANGIAN COHERENT STRUCTURES IN A COASTAL UPWELLING ENVIRONMENT; PART 2: NEAR-INERTIAL OSCILLATIONS IN THE NORTHEASTERN GULF OF MEXICO

Matthew Kenneth Gough

Approved:

_____
Ad Reniers, Ph.D.
Professor of Free Surface Waves
Delft University of Technology

_____
Brian Haus, Ph.D.
Professor of Ocean Sciences

_____
Josefina Olascoaga, Ph.D.
Associate Professor of Ocean Sciences

_____
Guillermo Prado, Ph.D.
Dean of the Graduate School

_____
Jamie MacMahan, Ph.D.
Associate Professor of Oceanography
Naval Postgraduate School

_____
Jeffrey D. Paduan, Ph.D.
Professor of Oceanography
Naval Postgraduate School

GOUGH, MATTHEW KENNETH (Ph.D., Applied Marine Physics)

Part 1: Lagrangian Coherent Structures in a Coastal Upwelling Environment; Part 2: Near-Inertial Oscillations in the Northeastern Gulf of Mexico. (May 2016)

Abstract of a dissertation at the University of Miami.

Dissertation supervised by Professors Brian Haus and Ad Reniers.
No. of pages in text. (118)

Part I: Time evolving 2-D observations of near-surface flow with high frequency (HF) radar are well-suited for calculating Lagrangian Coherent Structures (LCSs) which are a valuable tool for observing turbulent flow. By comparing the evolving HF radar-derived LCS fields with satellite sea surface temperature imagery, the evolving structure of upwelling fronts, filaments, retention zones, and eddy-like recirculation are captured in the upwelling environment off the California coast.

Part II: The inertial frequency is nearly diurnal at 30°N latitude which transects the northeastern Gulf of Mexico (NeGoM). At this latitude, near-surface inertial oscillations can amplify due to resonance with diurnal wind forcing. Diurnal oscillations have also been attributed to diurnal tidal forcing in this region. Because tidal forcing, wind forcing, and inertial oscillations are nearly diurnal, a unique series of comparative analyses are required to determine their relative influence on surface circulation. By comparing surface currents obtained by HF radar to predictions of the inertial response to wind forcing and barotropic tidal currents, it is found that diurnal oscillations in the NeGoM were predominantly due to wind-forced inertial oscillations in June 2010. The analyses provide a unique spatiotemporal perspective of inertial oscillations in the NeGoM where

there is evidence of propagation, frequency and phase shifts, and amplitude variability. Positive (negative) sub-inertial vorticity ζ in the ocean shifts the effective inertial frequency f_{eff} of near-inertial oscillations (NIOs) above (below) the local inertial frequency f according to the relationship $f_{eff} = f + \zeta/2$. It is found that NIO frequencies are consistent with f_{eff} determined from the vorticity field over the outer Mississippi Bight shelf and along the northern edge of the DeSoto Canyon during the last week of June 2010. Additionally, spatial NIO phase shifts associated with the frequency field of the NIOs are found to generate oscillatory divergence. In June 2010 oil from the Deepwater Horizon spill traversed through the NeGoM and it is speculated that the oil was exposed to mixing generated by the NIOs.

TABLE OF CONTENTS

Page

LIST OF FIGURES v

LIST OF TABLES vi

Chapter

1 INTRODUCTION 1
Lagrangian Coherent Structures in a Coastal Upwelling Environment 3
Resonant Near-Inertial Oscillations in the Northeastern Gulf of Mexico 4
The Influence of Vorticity on Near-Diurnal Inertial Oscillations in the Northeastern Gulf of Mexico 5

2 LAGRANGIAN COHERENT STRUCTURES IN A COASTAL UPWELLING ENVIRONMENT 6
Background 6
HF Radar Data Processing 11
Wind Data 13
Satellite SST Data 14
FTLE Calculations 15
Late March Observations of an Upwelling Jet, Front, and Filament 17
Late March Overview of Circulation 17
Late March 25 and 125 Hour FTLE Comparisons with SST 18
Late March HF radar-Derived Pseudo-Drifters 20
Early September Observations of and Eddy-Like Feature 21
Early September Overview of Circulation 22
Early September Pseudo-Drifter and 125 Hour FTLE Evolution 22
Late September Observations of Fronts and Filaments 25
Late September Overview of Circulation 25
Late September Pseudo-Drifter, FTLE, and SST Comparisons 27
Discussion on Late March Upwelling Front and Filament 28
Discussion on Late March Comparison of 125 and 25 hour FTLE Fields 29
Discussion on Late September FTLE Field Comparison with SST 31
Discussion on Retention Zone off Point Reyes 32
Discussion on Comparison of Moderate and Strong Upwelling 33
Summary 34

3 RESONANT NEAR-SURFACE INERTIAL OSCILLATIONS IN THE NORTHEASTERN GULF OF MEXICO 45
Background 45
HF Radar Data 50
Wind Stress 52

Slab Model of Inertial Oscillation Response to Wind Forcing 52
Tidal Current Predictions 55
June 2010 Mean Flow 56
Wind Forcing 57
HF Radar Observed Diurnal Surface Current Oscillations 58
Point-wise Comparisons between Slab Model and HF Radar Currents 60
Synoptic Slab Model Oscillations and HF Radar Surface Currents 61
Diurnal Complex Demodulation of *Zi* and HF Radar Surface Currents 62
Determination of Wind-Forced Inertial Oscillations 65
Spatiotemporal Variability of Inertial Oscillations 68
Summary and Concluding Remarks 72

4 THE INFLUENCE OF VORTICITY ON THE EFFECTIVE FREQUENCY OF NEAR-DIURNAL OSCILLATIONS IN THE NORTHEASTERN GULF OF MEXICO 85
Background 85
HF Radar Data 88
Diurnal Complex Demodulation of HF Radar Surface Current Velocities 89
Chlorophyll and Turbidity Satellite Imagery 90
Overview of Circulation, Vorticity, and Near-Inertial Oscillations 91
Frequency and Phase Shifts of NDIOs along the outer MBS and DC 92
Oscillatory Divergence between the MBS and DC 96
Summary and Discussion 97

5 CONCLUDING REMARKS 105

REFERENCES…… 106

LIST OF FIGURES

Chapter

2 Fig. 2.1 38
Fig. 2.2 38
Fig. 2.3 39
Fig. 2.4 40
Fig. 2.5 40
Fig. 2.6 41
Fig. 2.7 41
Fig. 2.8 41
Fig. 2.9 43
Fig. 2.10 43
Fig. 2.11 44

3 Fig. 3.1 76
Fig. 3.2 77
Fig. 3.3 77
Fig. 3.4 78
Fig. 3.5 79
Fig. 3.6 80
Fig. 3.7 81
Fig. 3.8 81
Fig. 3.9 82
Fig. 3.10 82
Fig. 3.11 83
Fig. 3.12 84
Fig. 3.13 84

4 Fig. 4.1 100
Fig. 4.2 100
Fig. 4.3 101
Fig. 4.4 101
Fig. 4.5 102
Fig. 4.6 102
Fig. 4.7 103
Fig. 4.8 103
Fig. 4.9 103
Fig. 4.10 104

LIST OF TABLES

Chapter

3 Table 3.1 75
Table 3.2 75

Chapter 1

Introduction

As indicated by the title, this manuscript is primarily comprised of two parts where part I is comprised of Chapter 2 and part II is comprised of Chapters 3 and 4. The titles of the following chapters are as follows: Chapter 2) Lagrangian Coherent Structures (LCSs) in a Coastal Upwelling Environment, Chapter 3) Resonant Near-Inertial Oscillations in the Northeastern Gulf of Mexico, and Chapter 4) The Influence of Vorticity on Near-Diurnal Near-Inertial Oscillations in the Northeastern Gulf of Mexico. Chapter 5 includes concluding remarks. Although the subject matter and study location in chapter 2 are not related to chapters 3 and 4, all three chapters are related in that coastal near-surface current velocities are obtained with HF radar technology. Additionally, the underlying goal in all three chapters is to contribute to the knowledge of how pollutants such as oil are transported, mixed, and dispersed off the coasts of California and the Gulf of Mexico. Chapters 2 and 4 have been submitted separately to scientific journals and are currently under review. A version of chapter 3 has been accepted by JGR-Oceans for publication.

Because HF radars measure near-surface currents over a majority of the coastal United States in near real time, they provide an excellent resource for search-and-rescue missions and oil spill mitigation (e.g. [*Abascal et al.*, 2011; *Abascal et al.*, 2009]). Re-analysis of surface current data obtained with HF radar can be implemented to gain a greater understanding of upper ocean dynamics that influence oil spills. Examples of HF radar data re-analysis includes studies on LCSs [*Coulliette et al.*, 2007; *Lekien et al.*, 2005; *Olascoaga et al.*, 2008; *Olascoaga et al.*, 2006], dispersion

[*Gildor et al.*, 2009; *Haza et al.*, 2010], and surface transport [*Kaplan and Largier*, 2006; *Zelenke et al.*, 2009].

LCS analyses determined from HF radar data in chapter 2 identify confluence and barriers in surface flow off the California coast which can be applied to prediction of oil spill accumulation. Similar studies on LCSs with HF radar have been previously performed [*Coulliette et al.*, 2007; *Lekien et al.*, 2005; *Olascoaga et al.*, 2006], although these studies focused on idealized case studies and on the potential application of LCSs determined from HF radar. Here, the focus is on applying LCSs to explain the coastal dynamics. This is exemplified in chapter 2 where LCSs extending off Point Reyes identify a retention zone associated with long-shore coastal upwelling jets and cold water filaments extending off shore. Additionally, LCSs identify confluence along an upwelling front which migrates offshore consistent with theoretical upwelling front migration. Overall, this study on LCSs provides a more general view of retention zones and confluence by investigating three scenarios of upwelling conditions off the California coast.

The spatiotemporal variability of NIOs discussed in chapters 3 and 4 can be applied to vertical mixing of oil in the northeastern Gulf of Mexico. NIOs potentially mix the upper ocean through the generation of shear below the mixed layer [*Zhang et al.*, 2009; *Zhang et al.*, 2010], and the generation of internal waves [*Kunze*, 1985]. *Zhang et al.* [2010] speculated that modeled inertial motions could generate enough shear below the mixed layer to eventually "mix out" the mixed layer. This could have a profound effect on oil at the surface which would be subjected to this type of vertical mixing. It is well known that internal waves promote mixing in the ocean [*Christopher Garrett and*

Munk, 1972]. The northeastern Gulf of Mexico is an ideal region for the generation of internal waves due to strong stratification and large amplitude NIOs. NIOs in a strongly stratified ocean can generate internal waves along a coastal boundary [*Millot and Crépon*, 1981] and by divergence from asynchronous oscillations [*Hyder et al.*, 2011]. It is speculated that large NIOs observed in chapters 3 and 4 in the vicinity of the Deepwater Horizon Spill mixed oil from shear below the mixed layer, the generation of internal waves along a coastal boundary, and through the generation of internal waves from asynchronous NIOs.

Lagrangian Coherent Structures in a Coastal Upwelling Environment

Finite Time Lyapunov Exponents (FTLEs), a type of LCS, and pseudo-drifter trajectories determined from near-surface current velocities obtained with HF radar provide a unique spatiotemporal perspective of the evolving structure of dynamic features such as fronts, filaments and eddy-like circulation in the upwelling environment off the California coast. Previous work by the author to capture these dynamic features off the California coast with time-averaged near-surface vorticity and divergence fields determined from Eulerian HF radar data has had limited success. The Lagrangian frame of the FTLE fields has an advantage over Eulerian time-averaging, which is typically applied to HF radar data, since the evolving nature of the dynamics can be more readily captured. Comparisons of the FTLE fields with satellite SST imagery provide FTLE field efficacy. During strong upwelling-favorable conditions in March 2009, FTLEs capture the surface signature of an upwelling jet and the offshore migration of an upwelling front. During two periods of moderate upwelling-favorable conditions in September 2009, FTLEs identify flow boundaries encircling an eddy-like feature, an upwelling front, and a

front associated with a cold water filament. A unique retention zone pattern is often observed where coastal jet pulses repeatedly deposit surface waters off Point Reyes. In one case, pseudo-drifters and FTLE ridges flow across a filament observed with satellite SST imagery. This is believed to be due to surface layer advection over the underlying filament structure.

Resonant Near-Inertial Oscillations in the Northeastern Gulf of Mexico

The inertial frequency is diurnal at 30°N which coincides with the latitude of the northeastern Gulf of Mexico (NeGoM). At this latitude diurnal wind forcing can induce resonant amplification of near-surface inertial oscillations as observed by *Jarosz et al.* [2007]. Over the inner Mississippi Bight Shelf (MBS) diurnal oscillations have been attributed to diurnal tidal forcing by *Seim et al.* [1987]. In between these two regions tidal forcing, wind forcing, and inertial oscillations are potentially important and nearly diurnal. A unique series of comparative analyses are therefore required to decipher the relative influence of these diurnal mechanisms. By comparing June 2010 HF radar surface currents to predictions of the inertial response to wind forcing and barotropic tidal currents it is found that, at this time, diurnal oscillations over the continental shelf between these two study sites were predominantly due to wind-forced inertial oscillations. The analyses provide a unique spatiotemporal view of inertial oscillations in the NeGoM where there is evidence of propagation, enhancement related to bathymetrically influenced flow, and abrupt spatial phase changes. Because inertial oscillations mix the ocean differently than tides, and their variability can induce vertical mixing, these results provide insight into how inertial oscillations potentially mixed oil from the Deepwater Horizon spill in June 2010 as the oil traversed the NeGoM

continental shelf. Near-diurnal oscillations during the winter are more strongly attributed to tidal forcing (particularly over the MBS) as wind-driven inertial oscillations are diminished due to a deeper mixed layer.

The Influence of Vorticity on the Effective Frequency of Near-Diurnal Inertial Oscillations in the Northeastern Gulf of Mexico

Positive (negative) sub-inertial vorticity ζ in the ocean shifts the effective inertial frequency f_{eff} of near-inertial oscillations (NIOs) above (below) the local inertial frequency f according to the relationship $f_{eff} = f + \zeta/2$. Because f_{eff} becomes the intrinsic frequency of NIOs, spatial variability in vorticity induces spatial variability in NIO frequency and phase shifts which leads to the generation of oscillatory divergence in the surface mixed layer. The oscillatory divergence in the mixed layer can enhance mixing by displacing the pychnocline and generating internal waves. Near-surface NIOs can be large in the northeastern Gulf of Mexico (NeGoM) where diurnal wind-forcing can resonate with f which is diurnal at 30°N and efficiently excite a typically shallow (5-10 m) surface mixed layer. From HF radar surface current velocities obtained in June 2010 it is found that NIO frequencies are consistent with f_{eff} determined from vorticity field over the outer Mississippi Bight shelf and along the northern edge of the DeSoto Canyon. Additionally, spatial NIO phase shifts associated with the frequency field of the NIOs are found to generate oscillatory divergence. During this time oil from the Deepwater Horizon spill traversed through this region and it is speculated that the oil was exposed to mixing due to oscillatory divergence generated by the NIOs.

Chapter 2

Lagrangian Coherent Structures in a Coastal Upwelling Environment

Background

The north-central California Coast between Point Arena (PA) and Point Reyes (PR) is known for strong coastal upwelling and associated ocean dynamic features such as upwelling fronts [*Austin and Lentz*, 2002], coastal jets [*Barth et al.*, 2000; *Brink*, 1992; *Davis*, 1985], filaments (also known as "meanders" or "squirts") [*Davis*, 1985; *Flament et al.*, 1985], and eddy-like circulation [*Halle and Largier*, 2011]. There have been numerous collaborative projects that have investigated the upwelling dynamics in this region: the Coastal Ocean Dynamics Experiment (CODE) [*Beardsley and Lentz*, 1987], Coastal Transition Zone Experiment (CTZ) [*Brink and Cowles*, 1991; *Huyer et al.*, 1991], Northern California Coastal Circulation Study (NCCS) [*Largier et al.*, 1993], the Eastern Boundary Current (EBC) experiment [*Brink et al.*, 2000], and the Wind Events and Shelf Transport (WEST) project [*Largier et al.*, 2006]. Directly to the south of PR, circulation in the Gulf of the Farallones (GoF) is less influenced by upwelling dynamics and more strongly influenced by tidal currents due to its proximity to the mouth of the San Francisco Bay [*Gough et al.*, 2010].

Persistent winds over the ocean with the coastline to the left of the wind orientation in the northern hemisphere (e.g. southward winds off a north-south oriented coastline to the east) develop offshore Ekman transport at the surface [*Ekman*, 1905], onshore transport along the bottom, and upwelling along the coast [*Austin and Lentz*, 2002; *Brink*, 1983; *Roughan et al.*, 2006; *Steger et al.*, 2000]. During this process the pycnocline is tilted upward along the coast and eventually intersects with the surface as

an upwelling front that migrates offshore if winds persist. Henceforth, winds that promote upwelling will be referred to as “upwelling-favorable”. Other mechanisms that promote vertical motion along the coast include wind stress curl [*Bakun and Nelson*, 1991; *Capet et al.*, 2004; *Pickett and Paduan*, 2003], variations in vorticity produced by strong winds over an oceanic jet resulting in surface divergence [*Niiler*, 1969], and a positive total time derivative of surface current vorticity [*Arthur*, 1965].

Based on wind data collected at NDBC buoy 46013, the Sonoma County coastline (SCC, the region between PA and PR) experiences some of the strongest upwelling-favorable winds along the U.S. west coast [*Dorman and Winant*, 1995]. Directly to the south of PR upwelling-favorable winds typically decrease in the GoF. Three distinct seasonal wind regimes along the northern California coast have been identified [*García-Reyes and Largier*, 2012; *Gough et al.*, 2010; *Largier et al.*, 1993]: Upwelling season (April-June) exemplified by strong upwelling-favorable winds, relaxation season (July-September) exemplified by diminished upwelling-favorable winds, and storm season (December-February) exemplified by strong wind shifts associated with storm passages. These are seasonal trends and wind events, such as upwelling-favorable winds during the relaxation season, can occur at any time during the year.

Coastal upwelling jets that develop off topographic promontories are complicated and include the influence of large scale circulation patterns, local winds, wind-stress curl, conservation of vorticity, thermal wind imbalance, and interaction with undercurrents [*Barth et al.*, 2000]. The coastal upwelling jet off PA has been observed to bifurcate, with one branch directed offshore (separated jet) and the other branch directed equatorward along the coastline (shelf jet) [*Davis*, 1985; *Halle and Largier*, 2011; *Kaplan et al.*, 2009;

Roughan et al., 2006]. The shelf jet can form the eastern boundary of an anti-cyclonic eddy-like recirculation feature south of the bifurcation which can extend the retention periods of water off the SCC from 2 days to up to 2 weeks [*Halle and Largier*, 2011]. Mean residence times of surface waters along the coastline associated with the shelf jet and within the eddy-like feature were 5 and 9 days, respectively. *Roughan et al.*[2006] speculated that the offshore jet could be influenced by interaction with California Current mesoscale eddy circulation impinging on the shelf.

The upwelling jet off PR, like PA, has been observed to bifurcate, with the main branch directed offshore and a weaker branch directed southward into the GoF [*Gough et al.*, 2010; *Kaplan et al.*, 2009; *Roughan et al.*, 2006]. Inter-annual variability in upwelling conditions can influence the across-shore position of the bifurcation, and the position of the upwelling jet, which has been linked to biological productivity and climatology [*Kaplan et al.*, 2009]. In addition to the complex coastline, circulation is also likely influenced by an abrupt widening of the shelf at Cordell Bank [*Kaplan et al.*, 2005; *Roughan et al.*, 2006]. Offshore deflection of an upwelling jet has been observed to be associated with coastal banks such as Heceta Bank, Oregon [*Barth et al.*, 2000]. Since the water directly north of PR typically contains newly-upwelled nutrient rich water, and water directly south of PR contains San Francisco Bay outflow water, the connection between these two regions has important biological implications such as meroplanktonic distributions [*S. R. Wing et al.*, 1995; *Stephen R. Wing et al.*, 1998].

Coastal ocean fronts have been studied using moored and shipboard ADCPs and CTD casts, satellite SST imagery [*Breaker*, 2005; *Castelao et al.*, 2006], numerical models [*Austin and Lentz*, 2002; *Foo*, 1981], or a combination of the above methods

[*Fontana*, 2013; *Pallàs-Sanz et al.*, 2010]. Identification of fronts using ADCPs and CTDs are limited to case studies of specific fronts (in the case of shipboard instrumentation) or limited by the concentration and distribution of the instruments (in the case of moored instrumentation). Satellite imagery studies are limited by cloud cover, which is particularly problematic along the U.S. west coast, and the frequency of overhead satellite passes. High frequency (HF) radar, which is not affected by cloud cover, provides a unique spatiotemporal view of coastal ocean surface currents and therefore should, in principle, be able to identify fronts and track their evolution in coastal regions. However, frontal identification by the author and *Fontana* [2013] with HF radar-derived convergence and vorticity time-averaged Eulerian calculations has had limited success. This is likely due to the inability of time-averaged Eulerian calculations to identify spatially migrating fronts. But, time-averaging is necessary because the vorticity and divergence spatial derivatives can be of the same order of magnitude as HF radar error. In addition, fronts can occur at scales too small to be resolved by HF radar as in the case of frontogenesis due to ageostrophic secondary circulation [*Fontana*, 2013; *Pallàs-Sanz et al.*, 2010] and/or cold filament intensification [*McWilliams et al.*, 2009]. This type of sub-mesoscale frontogenesis occurs at scales smaller than the baroclinic Rossby radius of deformation (*Ro*). *Ro* for a mixed surface layer depth, *h*, of 10 m (100 m) is approximately 3.5 km (11 km) where $Ro = \left(gh\Delta\rho/\rho\right)^{1/2}\Big/ f$ following *Fontana* [2013]. HF radar resolution would need to be 1.75 km (5.5 km) at best to capture these types of fronts. Course HF radar resolution (> 6 km) should be able to resolve frontogenesis associated with the sharpening of a horizontal density gradient due to horizontally confluent flow at scales larger than *Ro* which can occur in combination with

smaller scale frontogenesis due to ageostrophic secondary circulation [*McWilliams et al.*, 2009]. Frontal identification with HF radar data is therefore limited to scenarios when HF radar resolution is sufficiently fine or associated frontal currents are sufficiently strong in relation to HF radar error [*Cordero et al.*, 2009; *Gildor et al.*, 2009; *Haus et al.*, 2003].

The use of Finite-Time Lyapunov Exponent (FTLE) and Finite-Size Lyapunov Exponent (FSLE) field maxima to determine Lagrangian Coherent Structures (LCSs) has become a valuable tool for visualizing the complex structure of ocean circulation at various spatial and temporal scales [*Berta et al.*, 2014; *Coulliette et al.*, 2007; *Nencioli et al.*, 2011; *Olascoaga et al.*, 2006; *Reniers et al.*, 2010; *Shawn C. Shadden et al.*, 2009]. Since backward attracting FTLE-determined LCSs identify "transport barriers" in fluid motion, they are useful for mapping transport pathways and accumulation of ocean surface floating material such as pollution, oil, and algae [*Coulliette et al.*, 2007; *Lekien et al.*, 2005; *Olascoaga*, 2010; *Olascoaga et al.*, 2008; *Olascoaga et al.*, 2006]. Attracting FTLE field maxima occur in regions of Lagrangian confluence which should, in principle, identify convergent fronts. FTLE field maxima also occur along regions of abrupt shear, such as along a "shear jet" [*George Haller and Beron-Vera*, 2012], which should, in principle, identify "shear fronts" [*Fontana*, 2013] and coastal upwelling jet boundaries.

The time-varying Eulerian 2-D HF radar-derived current vector field permits the calculation of pseudo-drifter backward trajectories which can be used to calculate attracting FTLE and FSLE field maxima [*Berta et al.*, 2014; *Coulliette et al.*, 2007; *Olascoaga et al.*, 2006; *S. C. Shadden et al.*, 2005; *Shawn C. Shadden et al.*, 2009]. Advances in HF radar technology and LCS techniques have been simultaneously

developed over the last decade and are still in the process of being developed. HF radar currently measures ocean surface currents in near real-time over approximately 50% of the coastal U.S. and almost the entire U.S. west coast. The combined use of LCS techniques and HF radar technology therefore provides novel application opportunities. Additionally, the HF radar limitations in capturing migrating fronts with time-averaging are remedied because LCSs can determine migrating fronts.

Here, HF radar-determined LCSs along the northern California coast are used to identify and map unique dynamic features such as upwelling jets, fronts, filaments, and eddy-like circulation during three time periods (March, early September, and late September 2009). These three time periods were chosen based on favorable LCS representation of exemplary dynamic features and good satellite SST coverage. The LCSs are compared with the satellite SST imagery to determine the effectiveness of identifying the dynamic features.

We expand on previous studies on the eddy-like circulation off the SCC [*Halle and Largier*, 2011], surface retention and fronts off PR [*Fontana*, 2013; *Stephen R. Wing et al.*, 1998], and the application of LCS techniques with HF radar data [*Coulliette et al.*, 2007; *Gildor et al.*, 2009; *Olascoaga et al.*, 2006; *S. C. Shadden et al.*, 2005; *Shawn C. Shadden et al.*, 2009]. Occasionally, inexact matches are observed when comparing satellite SST and corresponding FTLE fields. We offer explanations for the inexact matches and present some cautionary notes for the application of LCS techniques with HF radar.

HF Radar Data and Processing

Five ~12 MHz medium range (station names: COMM, FORT, MONT, SLID,

GCVE, BML1) and two ~5 MHz long-range (station names: PAFS, BMLR) HF radars have been measuring hourly 2-D sea surface currents in the coastal region between Pt. Arena and the Gulf of the Farallones (Figure 2.1) since May 2006 as part of the State Coastal Conservancy funded Coastal Ocean Currents Monitoring Program (COCMP). The HF radars were manufactured by CODAR Ocean Sensors (www.codar.com). The fundamentals in the application of HF radar for measuring surface currents are well documented [*D Barrick*, 1971; 1972; *D E Barrick and Lipa*, 1979b; *Stewart and Joy*, 1974]. 12 MHz (5 MHz) radars utilize the Doppler-shifted Bragg scatter of the electromagnetic signal off of 12.5 m (30 m) ocean gravity waves to measure the weight-averaged near-surface currents in the top ~1 m (~2.5 m) of the ocean. The near-surface current measured by each radar is approximately composed of the vector sum of a quasi-Eulerian current and a filtered (or partial) Stokes drift associated with waves of frequencies less than the Bragg frequency [*Ardhuin et al.*, 2009]. Hereafter, HF radar-measured "near-surface" currents will be referred to as "surface" currents.

Radial current data (sea surface velocities directed towards and away from the radars) were processed using CODAR Ocean Sensors software. These data were then processed and combined to create hourly total vector data (surface current velocity vectors) on a fixed 6 km grid using the HFRProgs matlab toolbox developed by David Kaplan and Mike Cook (https://cencalarchive.org/~cocmpmb/COCMPwiki/-index.php/HFR_Progs_download_page). Total vectors are decomposed into *u* (east-west) and *v* (north-south) directions. Radial data within a 10 km radius of the 6 km grid were averaged to calculate the total vectors. These data were further "processed", "cleaned", and screened using "nearest neighbor" statistics with a supplemental HFRProgs toolbox

developed by Chris Halle (http://www.bml.ucdavis.edu/boon/hfr_currents.html) [*Halle and Largier*, 2011]. Radial data from calibrated (measured) antenna patterns were used [*Kohut and Glenn*, 2003; *Lipa et al.*, 2006; *Paduan et al.*, 2006].

HF radar error and RMS differences between HF radar and other types of surface current measuring instrumentation has been found to range between 3 and 20 cm/s [*Carbajal and Pohlmann*, 2004; *Chapman et al.*, 1997; *Kaplan et al.*, 2005; *Kohut and Glenn*, 2003; *Long*, 2007; *Ohlmann et al.*, 2007; *Paduan et al.*, 2006; *Paduan and Rosenfeld*, 1996; *Wright*, 2008]. The error has been found to be random although changes in the local environment can create biases. Geometric Dilution of Precision (GDOP) error increases when the look angle between radar stations is large (in regions where two radars are looking at each other) or small (in regions far off the coast) [*Chapman and Graber*, 1997; *Chapman et al.*, 1997].

In order to perform FTLE calculations, gaps in the HF radar data were removed using spatial and temporal interpolation. Interpolation across large gaps in the data was avoided by choosing a boxed region that enclosed greater than 70 % temporal coverage (Figure 2.1). Interpolation to the coastline was performed by forcing coastline current velocities to zero. A 2-D gap-removal technique applicable to HF radar data, Open-Boundary Modal Analysis (OMA) [*Kaplan and Lekien*, 2007], was not implemented since spatial resolution with this technique is limited by the smallest spatial gap in the data set and we did not want to compromise spatial resolution beyond the 6 km HF radar grid in order to maximize our ability to resolve fronts.

Wind Data

Hourly wind speed and direction data at 5 m above sea level were obtained from

two NDBC buoys within the study region: Bodega Bay buoy 46013 and San Francisco buoy 46026 located at 38.24ºN, 123.30ºW and 37.75ºN, 122.82ºW, respectively. The neutral wind stress, $\vec{\tau} = \rho C_D |w| \vec{w}$, was calculated following *Large and Pond* [1981].

A simple linear regression analysis performed on the *u* and *v* component of the winds at buoys 46013 and 46026 for the entire year show good correlations with respective R^2 values of 0.66 and 0.80 and slopes of 1.13 and 0.87 ($P \approx 0$). This provided confidence in using the slopes and y-intersects from the linear regression analysis to reconstruct missing wind data from one buoy with data from the other buoy. Missing wind data at buoy 46013 from 3/1/2009 to 4/29/2009 were reconstructed with buoy 46026 data by applying the linear regression results (Figure 2.2).

Satellite SST Data

Day and night level 2 MODIS Advanced Very High Resolution Radiometer (AVHRR) 1 km resolution sea surface temperature (SST) data from satellites Aqua and Terra were obtained from the NASA Ocean Color archive (http://oceancolor.gsfc.nasa.gov). Additional AVHRR SST data were obtained from the NOAA CoastWatch archive (http://coastwatch.noaa.gov). The CoastWatch data are created from imagery calculated from a composite of multiple sensors averaged over 24 hours [*Li et al.*, 1998]. The MODIS data was preferred over the CoastWatch data since the sensor and exact time of image capture was known. CoastWatch data was therefore only used when MODIS data was missing.

Chlorophyll satellite imagery was also obtained but we do not present chlorophyll imagery since it did not provide more information already provided by SST imagery when trying to find matches with LCSs. It was hoped that there would be a LCS field

match with chlorophyll imagery when there was a lack of a match with SST. This did not occur, which was somewhat surprising since chlorophyll is expected to be a better passive tracer than SST. It is likely that some chlorophyll accumulation can occur along frontal boundaries at scales too small to be resolved by the available HF radar or satellite imagery. In addition, the dynamic upwelling environment along the California coast may not allow consistent accumulation of phytoplankton as there is constant advection of phytoplankton and regions of newly-upwelled nutrient-rich water.

FTLE Calculations

The time-varying Eulerian 2-D HF radar-derived current vector field permits the calculation of pseudo-drifter backward trajectories which can subsequently be used to determine attracting FTLE field maxima [*Coulliette et al.*, 2007; *Olascoaga et al.*, 2006; *S. C. Shadden et al.*, 2005; *Shawn C. Shadden et al.*, 2009]. Attracting FTLEs are determined by calculating the spatial separation of a field of Lagrangian backward trajectories during a chosen period of time [*G. Haller*, 2002; *G. Haller and Poje*, 1998; *Harrison and Glatzmaier*, 2010; *S. C. Shadden et al.*, 2005]. More specifically, the FTLE is defined by

$$\sigma = \frac{1}{\tau}\ln(\lambda_{\max})^{1/2}$$

where τ is the integration period and $\lambda_{\max}$ is evaluated from the maximum eigenvector of the deformation gradient tensor [*Harrison and Glatzmaier*, 2010]. Positive ridges in the resulting 2-D FTLE field identify regions along which fluid motion tends to stretch and converge. The advantage LCSs have over Eulerian time-averaging is that the Lagrangian aspect of the LCS calculation captures evolving structure of the flow field. For example, a narrow convergent front that spatially migrates with time will likely not be adequately

resolved by time-averaged Eulerian HF radar observations. All FTLE calculations in this study were performed with the Mangen software package (www.mangen.org).

Choosing an appropriate integration period is critical to capturing desired dynamical features. For example, an integration period of 200 hours was used to identify a coastal jet LCS in Monterey [*Coulliette et al.*, 2007] whereas integration periods of 24-36 days were used to identify LCSs in the California Current System [*Harrison and Glatzmaier*, 2010]. Of the many integration periods experimented with, we chose to focus on the 125 hour integration period FTLE results based on the dynamical features exhibited by the FTLE field, domain escape time of backward trajectories in the FTLE calculation, typical synoptic wind-forcing timescales [*Kaplan et al.*, 2005; *Largier et al.*, 1993], and to minimize the influence of tidal currents. For the March 2009 analysis, a 25 hour integration period was also examined.

The primary problems with FTLE calculations from HF radar data include premature domain-escaping trajectories and trajectory collisions with the no-slip coastline. Both of these problems can create artifacts in the FTLE fields. Surface current velocities along the SCC, particularly during strong upwelling-favorable wind-forcing events, can reach over 100 cm/s. At this velocity trajectories can traverse the entire domain in less than 48 hours which is particularly problematic for the 125 hour integration period calculations. The escaping trajectory problem is avoided by first choosing case study time periods with brief and/or moderate upwelling-favorable wind conditions, although this could not be avoided during March 2009 when there were strong upwelling-favorable winds. Second, forward and backward pseudo-drifter trajectories are examined for premature escape times and collisions with the coastline.

FTLE ridges associated with pseudo-drifter coastal collisions and escape times greater than 1/3 of the integration period were neglected. Surprisingly, coastline collisions were not a serious problem as flow is typically along-shore and shoreline impacts with the coastline were mostly limited to PR and these FTLE ridge artifacts were relatively easy to identify. Only relevant FTLE ridges are identified in the figures and addressed in the text.

Late March Observations of an Upwelling Jet, Front, and Filament

In this section we examine HF radar surface-current-derived 125 hour and 25 hour integration period FTLE field evolution during strong upwelling-favorable conditions off the SCC between 23 and 31 March, 2009 (Figures 2.3 and 2.4). Both 125 hour and 25 hour integration periods are used since there is a match between the 25 hour FTLE and satellite SST fields from 23 to 28 March, and a match between the 125 hour FTLE and satellite SST fields from 28 to 31 March. Comparisons of the two chosen integration periods provide insight into the application of LCSs during strong upwelling-favorable conditions.

Late March Overview of Circulation

Leading up to 23 March 2009, there was period of wind relaxation during 11-22 March with brief mild upwelling-favorable winds on 14, 19, and 20 March (Figure 2.2). Despite wind relaxation, surface currents generally exhibited weak equatorward flow and a weak equatorward jet over the shelf along the SCC. Strong upwelling-favorable winds commenced on 22 March and continued until 30 March with the exception of brief relaxation on 28 March. Because March is a transition month between the storm and upwelling seasons, the timing of the onset of upwelling-favorable winds is not unusual. On 23 March a 20-30 km wide well-defined jet developed along the SCC (exemplified in

Figure 2.5), and a jet pulse within the jet is outlined by FTLE ridge 1 (Figure 2.3.a-c). West of the jet, a large anticyclonic eddy-like feature developed with its center at approximately 123.8ºW 38.2 ºN (Figure 2.5). The jet, outlined by FTLE ridge 4 on 28-31 March, widened from approximately 35 km to 50 km (Figure 2.3.f-i), veered westward at PR, and current velocity within the jet increased to 60-80 cm/s. Offshore of the jet surface current velocities remained relatively weak ranging between 5 and 25 cm/s. As the equatorward jet increased in width and velocity, poleward currents along the western flank of the eddy-like feature increased in magnitude. Equatorward currents along the northern edge of the domain off PA also increased at this time creating a region of convergence west of the center of the eddy-like feature.

Satellite SST field evolution for 23-31 March off the SCC reflects the classic understanding of coastal upwelling where cold water is upwelled along the coast and migrates offshore (Figure 2.3). The cold water off the SCC on 23 March is likely recently upwelled water since CoastWatch SST imagery from 11 and 19 March (not shown) do not exhibit a SST signature indicative of upwelling and there is little evidence from the HF radar data that the cold water along the coast was advected from the north. As the upwelling front migrates offshore it appears to become unstable on 27 March (Figure 2.3.e).

Late March 125 and 25 Hour FTLE Field Comparisons with SST

Initially there is a poor match between the backward-time 125 hour FTLE and SST fields for 23-27 March 2009 (Figure 2.3.a, b, and e), but eventually FTLE ridge 4 captures the offshore migration of the upwelling front for 28-31 March (Figure 2.3.f-i). The initial poor match is likely due to a mismatch between the FTLE integration period

in relation to the onset of wind-forcing. The integration period for the 23-27 March calculations spans backwards in time across two distinct wind-forcing patterns since strong upwelling-favorable winds initiated on 22 March (Figure 2.2). After the winds have developed surface flow for a period of time similar to the 125 hour integration period, which occurs on 28 March, FTLE ridges 1 and 4 follow the offshore migration of the upwelling front. FTLE ridges 1 and 4 do not capture the instabilities in the SST front. However, regions of intensification along ridges 1 and 4 can be seen where the instabilities extend westward (Figure 2.3.f-i). Attempts to capture the instabilities with shorter integration periods were unsuccessful which may be due to dynamics at smaller spatial scales in relation to HF radar resolution.

On 28 March, FTLE ridge 1, which had previously been well defined, begins to fade as ridge 4 begins to develop (Figure 2.3.f). By 31 March, ridge 1 has completely dissipated as ridge 4 takes its place. This is a pattern that was frequently observed throughout the year during upwelling-favorable conditions: a FTLE ridge develops along the coast (presumably outlining an upwelling jet pulse), veers offshore at PR, gradually dissipates, and is replaced by another FTLE ridge that develops in a similar fashion. This pattern can also be observed in the following sections during September 2009.

Even though FTLE ridge 2 formed along the northern edge of the domain where pseudo-drifters used in the FTLE calculations escape the domain before the 125 hour integration period, we feel compelled to address ridge 2 due to its strength and prevalence, and because drifters south of ridge 2 were retained for at least 9 days at the end of the month. FTLE ridges similar to ridge 2 are another common feature that can be observed during upwelling-favorable conditions. A strong FTLE ridge, like ridge 2,

typically forms in the strong convergent region southwest of PA where strong equatorward flow off PA meets poleward flow on the western edge of the anticyclonic eddy-like feature that frequently forms in this region. Although this is a very distinct feature, matches with SST and chlorophyll imagery were typically not observed and this was the case for the 23-31 March time period. The lack of a match is likely due to confluence within homogeneous water that has occurred too quickly for chlorophyll to accumulate.

Although the focus is on 125 hour FTLEs, a single 25 hour FTLE snapshot comparison with SST for 23 March is provided to highlight the relevance of the two integration time periods (Figure 2.4). FTLE ridges A1 and A2 in figure 4 identify the general shape of the hook-like filament off PR at a time when there was a relatively poor match between the 125 hour FTLE field and the SST structure (Figure 2.3.a). Ridges A1 and A2 are likely capturing circulation generated by the filament which is occurring at timescales similar to 25 hours rather than 125 hours. Later, when the 125 hour FTLE field begins to better match the SST structure on 28 March (Fig. 2.3.f-i), the 25 hour FTLE field dissolves and becomes incoherent (not shown). It should be noted that as the FTLE integration period is reduced, the FTLE field tends to be less defined and more discontinuous which is why ridges A1 and A2 are not as strand-like as those in the 125 hour FTLE field. Comparisons between 125 and 25 hour FTLEs are discussed further in section 4.2.

Late March HF Radar-Derived Pseudo-Drifters

Two pseudo-drifter deployments were necessary in late March due to strong advection transporting the drifters out of the domain. The deployments are on 23 March

(Figure 2.3.a) and 26 March (Figure 2.3.d). The drifters are used to ascertain flow characteristics associated with the FTLEs.

In the first deployment, black drifters deployed east of FTLE ridge 1 on 23 March rapidly advect equatorward and begin to accumulate along the southern extension of ridge 1 (Figures 2.3.a-c). Light grey drifters deployed west of ridge 1 rotated anti-cyclonically and diverged with half of the drifters congregating south of FTLE ridge 2 and the rest accumulating to the west of ridge 1. Dark grey drifters initially advected equatorward but stalled at the southern edge of ridge 1. Based on pseudo-drifter behavior, ridges 1 and 2 are attracting FTLE ridges. The black drifters show across-shore diffluence with moderate confluence along ridge 1 and along the coastline. This is consistent with numerical model results by *Austin and Lentz* [2002] which showed tracer accumulation along the upwelling front and along the inner shelf, and upwelling in between the two regions of tracer accumulation.

The second pseudo-drifter deployment on 26 March exhibited a continuation and enhancement of strong equatorward flow (Figures 2.3.d-i). Shear in the flow along ridge 1 is not as abrupt as first pseudo-drifter deployment. In this case, the black and light grey drifters indicate there is initially no noticeable confluence along ridge 1 off the SCC (Figure 2.3.e). But, as before, there is strong confluence along ridge 1 off PR and in the GoF (Figure 2.3.f). Surprisingly, despite the enhanced widespread equatorward flow, a significant portion of the light grey drifters remained in the domain south of ridge 2 (Figure 2.3.i).

Early September Observations of an Eddy-Like Feature

In this section we examine the 125 hour FTLE field evolution for 5-11 September

2009 (Figure 2.6). This period of time was chosen because of the distinctive eddy-like pattern in the circulation which is captured by the FTLE field, and the relatively long residence times of pseudo-drifters which affords greater confidence in the FTLE calculations. During this time only one SST satellite image is available to make comparisons with the FTLE field (Figure 2.7).

Early September Overview of Circulation

Leading up to 5 September, there was a relaxation of winds followed by weak upwelling-favorable winds that initiated on 4 September (Figure 2.8). By 5 September an anti-cyclonic eddy-like feature began to develop centered at approximately 123.5°W, 38.4°N which is represented by the 7 September daily averaged currents (Figure 2.9). The eddy does not close as a line of divergent flow can be seen to extend southeastward from its center. Between 5 and 10 September, there were multiple brief pulses of upwelling-favorable winds. The eddy-like feature responded to the wind variability by exhibiting discontinuities, periods of development, and periods of disintegration.

Early September Pseudo-Drifter and 125 Hour FTLE Field Evolution

Compared to the March example, the early September FLTE field reacts differently to wind-forcing in that the onset of moderate upwelling-favorable winds do not cause the FTLE ridges to become less defined. Initially, the 5 September FTLE field encircles the eddy-like feature but does not enclose it as there is a large gap between ridges 1b and 3 (Figure 2.6.a). As moderate upwelling-favorable winds commenced late on 6 September, the eddy-like feature in the FTLE field became more defined and the FTLE ridges, which outline the eddy-like feature, almost close on 7 September (Figure 2.6.b). Between 8 and 11 September the eddy-like feature breaks down and the FTLE

field is dominated by ridge 2 (Figure 2.6.c). Note that the FTLE field on 5 September (Figure 2.6.a) more closely captures the SST field on 7 September (Figure 2.7). This is most likely because the FTLE integration period spans backward in time across a period of relaxed winds which allows the subsurface temperature structure to influence the flow. By 7 September the winds have begun to influence the flow although remnants of the subsurface structure remain since the integration period spans across the two wind-forcing regimes.

Satellite SST imagery for 7 September exhibits a large semicircular bulge of relatively warm water (15-16ºC) impinging upon the SCC shelf (Figure 2.7). This bulge of water is bound by a thin strip of relatively cold water (10ºC) along the SCC and cold water filaments off PA and PR. The FTLE structure captures the general shape of the warm water bulge and region between ridges 1b and 3 where the pseudo drifters exited. However, close examination reveals discrepancies. FTLE ridges 1a and 2 are significantly west of the surface temperature front along the thin strip of cold water along the coast. It appears that ridges 1a and 2 are identifying barriers within the eddy-like circulation although there was no evidence of chlorophyll accumulation along these ridges in satellite imagery (not pictured). It is possible that the SST front along the northern SCC is not active at scales that can be resolved by HF radar, although there are many other possible reasons for the poor matches which include HF radar GDOP error near the coastline [*Chapman and Graber*, 1997], surface confluence within a region of homogeneous surface water not identified in satellite SST imagery, and/or FTLE calculation backward trajectory premature domain exits and collisions with the no-slip coastline.

The FTLE field on 5 September (Figure 2.6.a) matches the SST field for 7 September 21:00 better than the 7 September FTLE field (Figure 2.7). This is particularly evident when comparing ridge 3 in figure 2.6.a with the SST front at the western extent of the cold water filament off PR in figure 2.7. The match between the 5 September FTLE field and 7 September is likely because the FTLE integration period spans backwards in time over a period of moderate and weak wind-forcing. The 5 September FTLE field therefore reflects the flow associated with the relatively stationary filament. By comparison, the 7 September FTLE field reflects the influence of two forcing regimes: relaxation flow and subsequently moderate wind-forcing that initiated on 6 September.

FTLE ridge 5 which extends from the Bodega Head in figures 2.6.b and 2.6.c separates the equatorward flow of the jet from poleward (and stationary) flow off PR. *Kaplan and Largier* [2006] observed a similar pattern. This jet weakens, yet remains, despite relaxation of upwelling-favorable winds from 9 to 11 September. Examination of other FTLE charts throughout the year show that a FTLE ridge often extends from the Bodega Bay region during weak upwelling and/or relaxation conditions.

Four sets of pseudo-drifters deployed on 5 September capture the complexity of the circulation, the origin and destination of surface water, and the influence of the LCSs (Figure 2.6.a). Dark grey drifters deployed along the northern edge of FTLE ridge 1a become constrained between ridges 1a and 2, and eventually collect along the entire length of strongly attracting ridge 2. The black drifters show the destination of waters that originate along the SCC. These drifters, initially deployed east of the ridges 1a and 2 which define the western edge of the eddy-like feature, rapidly advect equatorward along

the coast before veering offshore in a narrow jet. The southern boundary of this jet is identified by ridge 5 that extends from the coast just north of the Bodega Bay. The northern boundary of this jet is identified by FTLE ridge 2. As winds relax on 9 September, the black drifters suddenly stall, collect north of newly-formed ridge 6 in the northern GoF, and never leave the domain. The light grey drifters initially rotate anti-cyclonically before diverging and quickly exiting the domain through a gap in the FTLE field north of ridge 2. Drifters originating off PR, indicated by grey stars, slowly advected equatorward into the northern GoF and some of these pseudo-drifters accumulated along the southern edge of ridge 6. Overall, the flow is quite complex and the LCSs are certainly helpful in identifying flow barriers within the eddy-like feature and the retention zone off PR. This would not be possible with SST imagery, mean and hourly flow from HF radar, or tracking a field of pseudo-drifters.

Late September Observations of Fronts and Filaments

In this section we examine the 125 hour FTLE field evolution for 25-30 September 2009 in conjunction with an upwelling front off the SCC and a distinctive front at the southern boundary of a cold water filament off PR. Comparisons between FTLE ridges and SST fronts in this section illustrate the effectiveness and shortcomings of implementing HF radar-derived FTLE fields to identify SST fronts in an upwelling environment.

Late September Overview of Circulation

Leading up to 25 September, there was wind relaxation on 21-23 September, and a moderate pulse of upwelling-favorable winds on 24 September (Figure 2.8). The wind relaxed again on 25-28 September, and there was moderate upwelling-favorable wind-

forcing on 28-30 September (Figure 2.8). An equatorward jet developed on 24-25 September, continued to the end of the month, and followed along the SCC continental slope. The general characteristics of the jet are reflected in the daily averaged flow for 27 September (Figure 2.10). The jet ranged between 20 and 40 km wide and currents within the jet averaged about 30 cm/s. On either side of the jet (i.e. the inner shelf and beyond the continental slope) surface currents were weak and were intermittently poleward over the inner shelf.

SST imagery on 26 and 27 September shows a narrow strip of relatively cool (10-13ºC) water along the SCC and cold water filaments extending off PA and PR (Figure 2.11.b-c) which is similar to the SST pattern observed on 7 September (Figure 2.7). The front associated with the narrow strip of cool water remained stationary between 26-27 September which agrees with the lack of wind-forcing at this time. With the onset of upwelling-favorable winds on 28 September there was a westward migration of the SST front along the SCC from 28-30 September indicative of active coastal upwelling (Figure 11.d-e). During this time the front migrated approximately 30 km offshore. Although the front migrated offshore with the onset of winds, the cold water filament off PR remained stationary from 25 to 30 September suggesting that wind-forcing was not directly forcing the filament. There was a uniform decrease in the SST field between 27 and 30 September which was presumably due to widespread mixing at the surface due to wind-forcing.

A sharp SST gradient at the southern edge of the filament off PR remained relatively stationary from 26-30 September (Figure 2.11). The front has the appearance of warm water from the south colliding with the southern edge of the cold water filament. It

is conceivable that the filament is colliding with the relatively warm water associated with California Undercurrent at this location and that the two water masses do not override each other due to density similarities despite their temperature difference. *Flament et al.*[1985] examined a cold water filament extending from PA immediately north of relatively warm high salinity water where the densities of the two water masses were relatively similar even though there was a steep sea surface temperature gradient between them. The influence of the California Undercurrent on off-shore directed cold water filaments is believed to be important [*Barth et al.*, 2000] and there is evidence that the California Undercurrent surfaces (or nearly surfaces) in the northern GoF [*Noble and Ramp*, 2000] and off PR [*Roughan et al.*, 2006].

Late September Pseudo-Drifter, FTLE, and SST Comparisons

Despite wind relaxation between 25 and 27 September, the grey pseudo-drifters advected equatorward in the jet outlined by ridges 1a and 2 (Figure 2.11.a-c). The black pseudo-drifters did not rapidly advect equatorward and accumulated south of ridge 1a. There was abrupt shear at ridge 1a which can be determined from the relative motions of the black and grey pseudo-drifters. There was excellent agreement between the FTLE field and SSTs during this time. Ridge 4 matched the SST front along the SCC, ridge 3 matched the SST front at the western extend of the cold water filament, ridge 2 reflected apparent confluence in a region of relatively homogeneous SST, and ridge 1a appeared to resolve the separation of the jet off BB (Figures 2.11a-d). As upwelling-favorable winds developed on 28 September, ridge 1b strengthened, elongated off PR, and acted as an attracting barrier for the grey pseudo-drifters. The black drifters accumulated directly south of FTLE ridge 1b. A “sandwich effect” developed as grey pseudo-drifters along

ridge 1b are deposited directly north of the stalled black pseudo-drifters.

The match between the FTLE and SST fields on 28 September suddenly broke down by 30 September (Figure 2.11e). FTLE ridge 1b appears related to the cold water filament but is shifted to the south. A disconnect between surface circulation and the SST structure is further demonstrated by the black and grey drifters that advected through SST gradients associated with the filament. It is speculated that the surface forced layer observed by HF radar is riding over the underlying filament (see section 4.3).

Discussion on Late March Upwelling Front and Filament

It was shown in section 3.1.2 that FTLE ridge 4, which identified a coastal SST front, migrated offshore between 38-31 March (Figure 2.3.f-i). The offshore migration is consistent with an upwelling front. If it can be shown that the migration speed is consistent with a predicted upwelling front migration speed, then we can have greater confidence that the FTLE ridge is identifying an upwelling front. *Austin and Lentz* [2002] established a method for determining the cross-shore velocity of an upwelling front induced by Ekman transport associated with along-shore wind stress by implementing an idealized 2-D numerical model with a relatively shallow (10 m) continuously stratified pycnocline. They provided two methods for calculating the cross-shore front velocity based on depth of the mixed layer (D_{ML}) relative to the depth of the Ekman layer (δ_{E}). For $D_{\mathrm{ML}} < \delta_{\mathrm{E}}$, the front velocity ($u_F$) due solely to Ekman transport was found to be

$u_F = \dfrac{\tau^S}{\rho_0 f \delta_E}$ where $\delta_{\mathrm{E}} \approx Z_0 + \Delta Z/2$, τ^S is the surface wind stress, ρ_0 is the reference density, f is the local Coriolis parameter, Z_0 is the initial depth of the mixed layer, and $\Delta Z/2$ is an additional portion of the pycnocline also referred to as the “transition layer” in

Lentz [1992]. For the second method, $D_{ML} > \delta_E$, the same formula for the frontal speed is used except $\delta_E \cong \kappa\sqrt{\tau^S \rho_0^{-1}} \cdot f^{-1}$ where κ is the Von Kármán constant. Using $\tau^S = 0.16$ N/m^2, the average wind stress between 28 and 31 March, the first (second) method estimated the front velocity to be 8.9 cm/s (3.2 cm/s). This is consistent with the observed front speed between 28 and 31 March which is objectively estimated to be 5.8 cm/s from observations of satellite SST imagery and FTLE ridges 1 and 4. We do not have a 3-D view of the ocean so we can only speculate on the depth of the Ekman layer, depth of the mixed layer, and the density gradient across the pycnocline. *Lentz* [1992] observed that offshore flow associated with Ekman transport typically extended below the surface mixed layer even during strong wind-stress events. *Austin and Lentz* [2002] did not observe the mixed layer to extend deeper than the Ekman layer in their model.

The strong SST front identified by ridge A2 at the western extent of the cold water filament extending offshore from PR on 23 March (Figure 2.4) migrated westward at approximately 14 cm/s between 23 and 27 March which is significantly greater than the predicted upwelling front speed estimated above. This indicates that the filament extension is due to processes other than, or in addition to, Ekman dynamics which is in agreement with *Flament et al.*[1985] who observed filament extension speeds different than theoretical Ekman transport speeds. Ridge A2 tracks with the front offshore but further tracking was not possible as the front migrated outside of the FTLE domain on 25 March.

Discussion on Late March Comparison of 125 and 25 hour FTLE Fields

The importance of matching FTLE integration periods with forcing timescales is exemplified when comparing the 125 and 25 hour FTLE fields with SST imagery

between 23-31 March. As previously mentioned, the 125 hour FTLE does not match the SST field between 23-27 March, but does match between 28-31 March (Figure 2.3). In contrast, the 25 hour FTLE matches the SST field between 23-27 March (exemplified in Figure 2.4) but does not match the FTLE field between 28-31 March (not shown).

The initial poor match between the SST and 125 hour FTLE field is likely due to a mismatch between the FTLE integration period and wind-forcing timescales. The backward-time 125 hour FTLE calculations for 23-27 March span across two distinct wind regimes: the wind relaxation before 22 March and the strong upwelling-favorable winds after 22 March. After the winds have developed surface flow for a time-period similar to the 125 hour integration period, which occurs on 28 March and thereafter, FTLE ridges 1 and 4 follow the offshore migration of the upwelling front. Likewise, since there was a long wind relaxation period before 22 March, the 125 hour FTLE field before 22 March (not pictured) identifies the distinctive hook-like cold water filament visible on 23 March.

For the 25 hour FTLE on 23 March (Figure 2.4) the upwelling-favorable winds have just commenced, the cold water filament influence on the surface currents have not been overwhelmed by the influence of wind-forcing, and confluence associated the hook-like filament is identified by the 25 hour FTLE field. Leading up to the brief relaxation of upwelling-favorable winds on 22 March there was moderate upwelling-favorable winds that sufficiently deepened the mixed layer to bring the SST signature of the filament to the surface. Because the relaxation of winds on 22 March was brief, the 25 hour FTLE is able to capture the influence of the filament through vertical momentum transfer without the influence of the wind stress. After strong upwelling favorable winds develop on 28

March, the 25 hour FTLE field ridges become less defined and no longer reflect the SST signature (not shown). At this time the FTLE field reflects subtle gradients in the wind field which are not steep enough to be captured by integrating across 25 hours.

Discussion on Late September FTLE Field Comparison with SST

The SST front captured by FTLE ridge 4 (Figure 2.11) is likely an upwelling front but without observations below the surface it is not possible to be certain. The front migrates offshore slowly at first when winds are weakly equatorward and migrates faster when upwelling-favorable winds initiate. Following method 1 (2) for predicting the upwelling front speed in section 6.1, the upwelling front speed for 28-30 September is estimated to be 15.2 cm/s (3.3 cm/s). This is consistent with an objectively estimated offshore migration speed of 9 cm/s determined from the SST front associated with FTLE ridge 4.

There are excellent matches between the SST and 125 hour FTLE fields between 26-28 September. But, on 30 September, after upwelling-favorable winds initiated, there is a sudden mismatch between the FTLE field and SST field (Figure 2.11.d). The 26-28 September good matches between the FTLE ridges and SST fronts appear to be related to light winds. This suggests that when winds are light, the FTLE field captures the surface circulation which reflects either the large scale circulation responsible for the SST structure or surface circulation driven by subsurface structure identified by the SST. In the latter case SST fronts can create shear due to thermal wind balance or convergence due to frontogenesis induced by ageostrophic secondary circulation. These processes, when constrained within the mixed layer, will likely occur at scales that cannot be resolved by 6 km resolution HF radar data. But, the subsurface structure is likely thicker

than the mixed layer suggesting a larger *Ro*. Associated circulation could then occur at scales resolvable by HF radar.

The mismatch on 30 September is not due to discrepancies between the FTLE integration period and forcing timescales since changing the integration period did not change the results. In addition, pseudo-drifters advected through the cold water filament and associated SST gradients suggesting SST is not behaving as a passive tracer and that the drifters are riding over the underlying structure revealed by SST observations. The mismatch could be due to the inability of HF radar, which measures current velocities over the top 2.5 m of water column in this case, to capture subsurface circulation such as subsurface fronts and filaments that may not behave passively to wind-forcing. It is also possible that HF radar is overestimating the alongshore currents. When the surface gravity wave field is traveling perpendicular to a HF radar beam the amplitude of the current in the direction of wave propagation can be overestimated [*Wyatt*, 1986]. Locally generated short period wind-swell propagating southward will travel perpendicular to HF radar beams from stations BMLR, BML1 and PREY although radar coverage is good and there are other radars that cover this region.

Discussion on Retention Zone off Point Reyes

Throughout the HF radar-derived LCS dataset, FTLE ridges can be observed to extend off PR identifying this region as a retention zone. This was particularly true for the two September examples. The surface circulation pattern for 5-11 September 2009 demonstrated that the region off PR can be a “meeting place” for surface waters from various origins. This is exemplified in figure 2.6 where all four sets of drifters converge off PR. Eventually the light grey pseudo-drifters exit the domain, but the remaining 3 sets

of drifters end up in close proximity along FTLE ridges 2 and 6 (Figure 2.6.c). A "sandwich effect" tends to occur where water is advected into the northern GoF (or off PR) by upwelling jet pulses. The jet pulses deposit successive zonal strands of pseudo-drifters along FTLE ridges extending off PR. Eventually, zonal bands of drifters off PR accumulate where the oldest drifters are to the south and younger drifters to the north. Had another set of pseudo-drifters been deployed off the SCC on 8 September, they would have been deposited directly north of the detained black drifters by the jet pulse outlined by ridges 2 and 5 (Figure 2.6.c). A similar sandwich effect occurs at the end of September where dark grey and black drifters accumulate along FTLE ridge 1b (Figure 2.11.e). This supports previous work on the identification of the northern GoF as retention zone which is important for larval dispersion and meroplankton recruitment [*Stephen R. Wing et al.*, 1998].

Discussion on Comparison of Moderate and Strong Upwelling-Favorable Conditions

Differences in the FTLE and SST fields during strong (moderate) upwelling-favorable conditions in March 2009 (September 2009) reflect the influence of wind stress, mixed layer depth, and subsurface flow. The depth of the mixed layer plays an important role in the vertical transfer of momentum from wind-forcing at the surface to subsurface structures and from subsurface structures to the surface. LCSs determined with HF radar current velocities can therefore reflect the wind field while also being influenced by subsurface flow structure. Likewise, characteristics of vertical momentum transfer associated with the mixed layer will influence the correspondence between HF radar-determined LCSs and satellite SST imagery.

For the entire month of September the filament off PR appeared to remain relatively stationary. SST imagery from early in the month exhibited a cold water filament off PR in the same location later in the month. This can be seen when comparing the SST in figure 2.7 to figure 2.11.b and c. For 23-27 September the mixed layer is likely deep enough to bring subsurface water temperatures to the surface but there is not sufficient wind-forcing to drive the subsurface flow. Once strong wind-forcing initiates, the wind-driven surface flow measured by HF radar overwhelms the influence of the background flow and the HF radar-derived FTLE field no longer reflects the SST structure. At this time the FTLE field reflects the wind field or surface flow features directly driven by wind-forcing. Eventually, if strong wind-forcing persists, the transfer of momentum from wind-stress will drive subsurface circulation such as cold water filament growth and upwelling fronts, as was the case for March 2009. The March 2009 filament grew in size, extended off shore, and migrated southwestward out of the domain (Figure 2.3). When the cold water filament and upwelling front migrated offshore, presumably due to strong wind-forcing, deep transfer of momentum, and Ekman processes, there was also a feedback of subsurface flow to the surface. This feedback of sub-surface flow to the surface likely allowed FTLE ridge 4 to resolve the upwelling front in late March (Figure 2.3.e-i).

Summary

The time-varying 2-D near-surface current vector field obtained with HF radar is well-suited for calculating LCSs. By implementing HF radar-derived LCSs, we have presented a unique spatiotemporal perspective of the evolving nature of upwelling jets, fronts, and filaments off the California coast between PA and the GoF. Three time

periods during 2009 were examined: late March, early September, and late September. In early March 2009, at the onset of relatively strong upwelling-favorable conditions, 25 and 125 hour FTLE ridges capture the evolving spatial structure of an upwelling jet, the offshore migration of an upwelling front, and the southward migration of a cold water filament (Figures 2.3 and 2.4). In early September 2009, during moderate upwelling-favorable conditions, FTLE ridges identified flow barriers within an eddy-like feature at a time when warm offshore waters impinged upon the continental shelf (Figures 2.6 and 2.7). In late September, also during moderate upwelling-favorable conditions, FTLEs identified an upwelling front that propagated offshore, and flow barriers associated with a cold water filament extending off PR.

All three time periods (March, early September, and late September) exhibited anti-cyclonic eddy-like recirculation centered near 124º W, 38º20′ N, but their characteristics were different. March 2009 exhibited a convergent line extending southwestward from the eddy-like center (Figure 2.5) identified by FTLE ridge 2 (Figure 2.3). Early September exhibited a divergent line extending southwestward from the eddy-like center (Figure 2.9). Late September exhibited a convergent line extending south of the eddy-like center (Figure 2.10) identified by FTLE ridge 3 which corresponded with a SST front at the western boundary of a cold water filament (Figure 2.11). These features were referred to as “eddy-like” because they do not typically close as observed by *Halle and Largier* [2011].

FTLE analyses revealed an interesting pattern regarding the spatiotemporal structure of the retention zone off PR in both September cases when there was moderate upwelling-favorable conditions (Figures 2.6 and 2.11). Initially, an equatorward jet forms

off the SCC outlined by a FTLE ridge and pseudo-drifters deployed within the jet advect equatorward. The drifters are eventually deposited along a FTLE ridge extending off PR. Subsequently, another jet forms and deposits drifters along the northern edge of the previously deployed drifters. This process repeats itself such that horizontal bands of water are deposited off PR where the most recently deposited waters are to the north.

Upwelling fronts observed in SST satellite imagery in March and late September were identified by FTLE ridges. In both cases the FTLE ridge migrated offshore along with the SST front (FTLE ridge 4 in figures 2.3 and 2.11). The observed migration speeds were found to be comparable to predicted upwelling front speeds.

It was speculated that vertical transfer of momentum from wind stress to subsurface flow and visa-versa played an important role in the behavior of LCSs derived from HF radar near-surface current velocities. In late March the 25 hour FTLE field initially captured flow likely driven by the hook-like filament during light winds. Later, after four days of strong persistent winds, the filament is forced southwestward out of the domain presumably due to deep transfer of momentum associated with a deep surface mixed layer. It is believed that an upward transfer of momentum from the subsurface structure allowed the FTLE ridge to identify the offshore migrating upwelling front. In early September, the FTLE field initially matched the SST field since weak wind-forcing allowed surface flow to be influenced by the underlying structure. After a period of moderate wind-forcing the FTLE field no longer resembled the SST field. In this case the wind-forcing was not deep or strong enough to drive the filament since it remained relatively stationary as the near-surface FTLE field resembled wind-forced circulation. Like early September, relatively weak winds in late September allowed the FTLE field to

identify fronts in the SST field. Later, the FTLE field no longer matched many of the SST fronts after moderate wind-forcing had initiated. During this time HF radar-derived pseudo-drifters advected over the underlying filament identified by satellite SST imagery which indicated that wind-forcing was effectively driving the surface layer but not the underlying filament structure.

Chapter 2 Figures

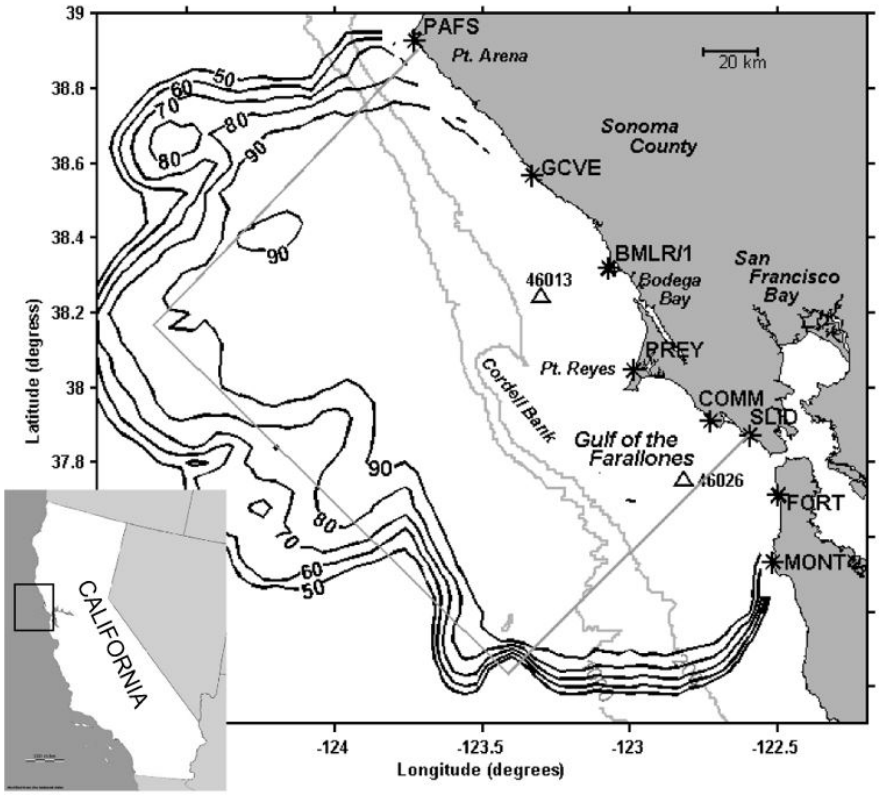

Figure 2.1. Location Map. The black box on the index map of California outlines the study area. The grey box on the primary map outlines the FTLE domain used in the following figures. Black contours show the HF radar percent temporal coverage. Grey lines off the coast denote the 200 and 1000 m isobaths. HF radar stations are denoted with stars. NDBC buoys 46013 and 46026 are denoted with triangles.

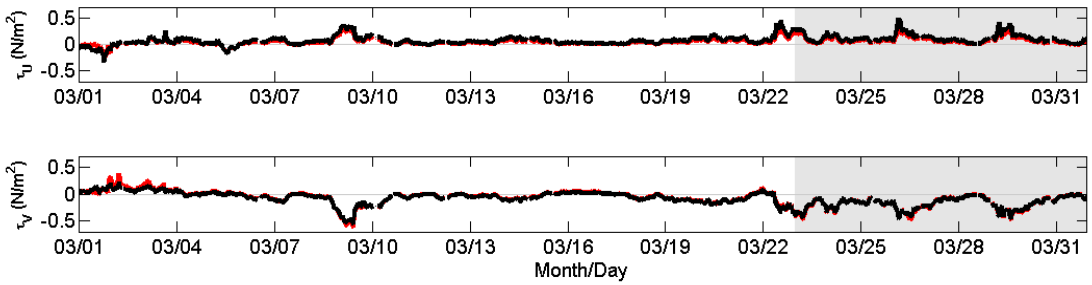

Figure 2.2. March 2009 time-series of *u* (top) and *v* (bottom) components of wind stress at Bodega Bay NDBC buoy 46013 (black line) reconstructed from San Francisco NDBC buoy 46026 (red line). Time period of interest, 23-31 March, is indicated by grey shading.

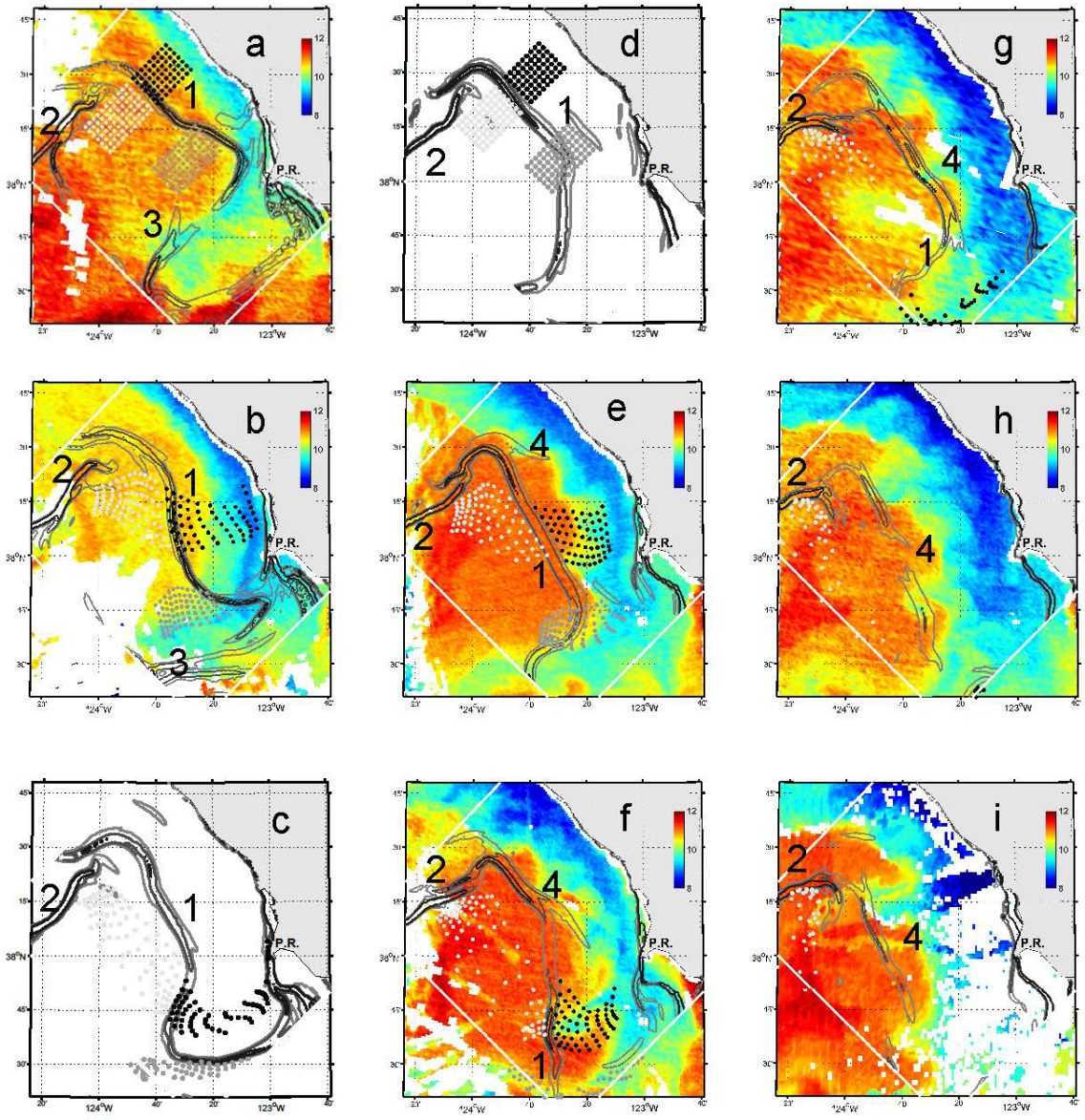

Figure 2.3. FTLE ridges (black and grey contours) overlaid on satellite SST (color contours, °C) evolution along with pseudo-drifters (black, grey and light grey dots) for (a - i) 23 – 31 March. FTLE ridges are numbered. MODIS SST imagery was used in all maps except for 31 March which used CoastWatch data. Pseudo-drifters were deployed twice (23 March and 26 March). The light grey box marks the boundary of the LCS field.

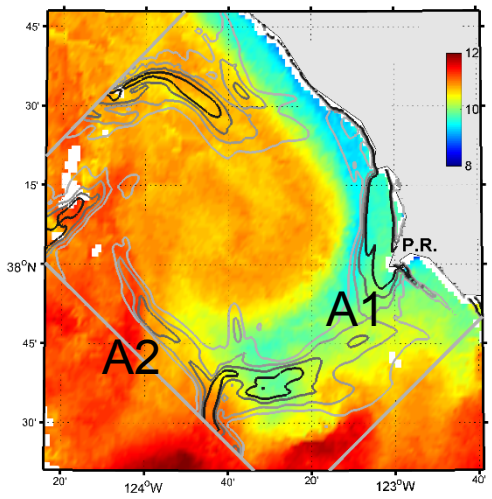

Figure 2.4. Coastwatch SST imagery with overlaid 25 hour FTLE field (black and grey contours) for 23 March, 2009.

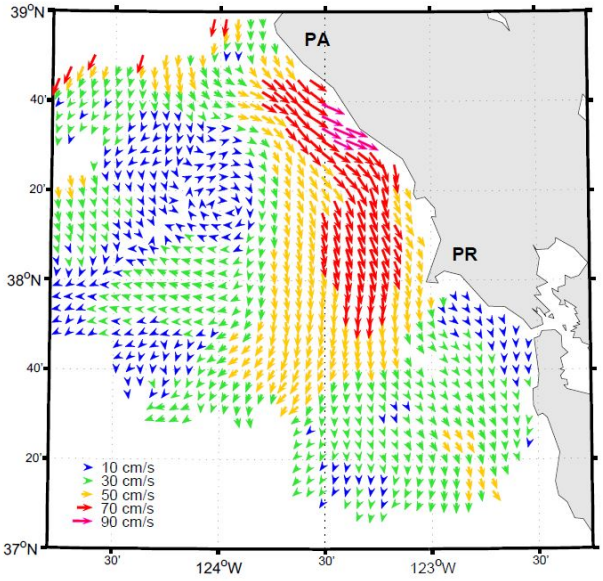

Figure 2.5. Mean HF radar surface current vectors for 25 March, 2009.

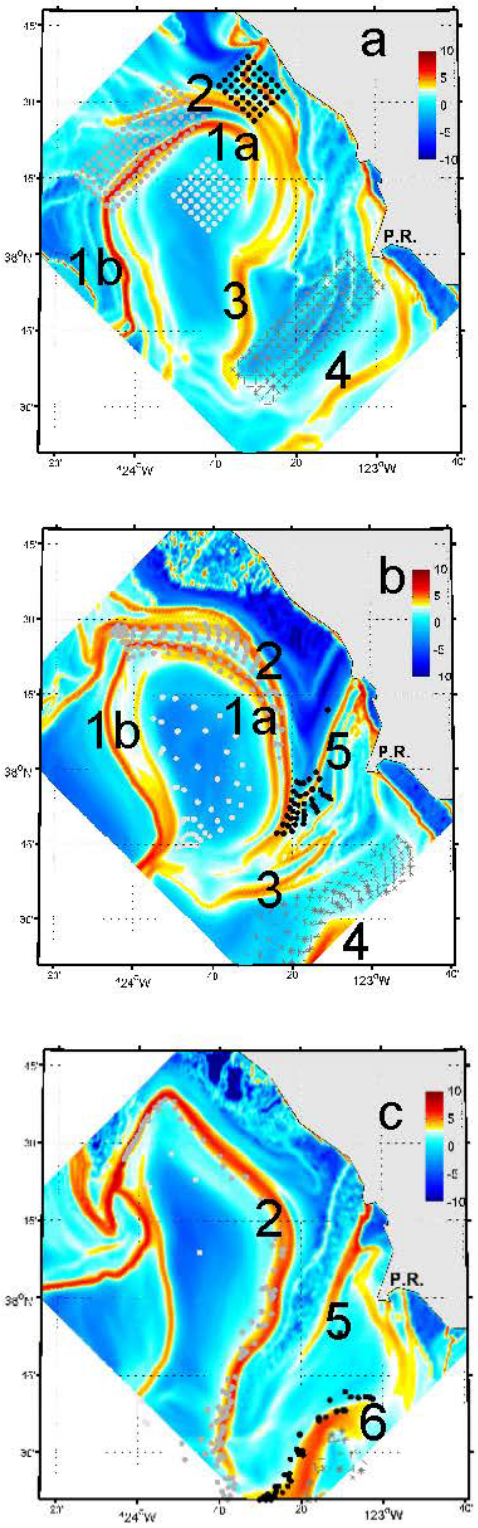

Figure 2.6. FTLE field evolution (color contours) and four sets of pseudo-drifters (black, grey, light grey dots, and grey stars) for (a-c) 5, 7 and 11 September.

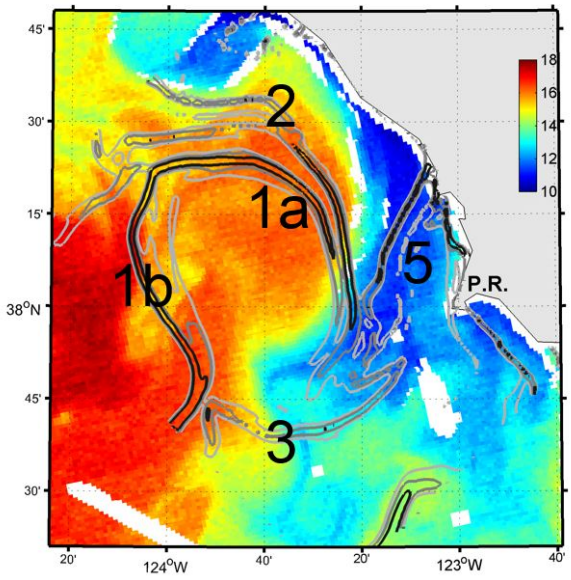

Figure 2.7. MODIS satellite SST color image with overlaid FTLE field (black and grey contour lines) for 7 September 21:00 UTC. This figure corresponds with Figure 8b.

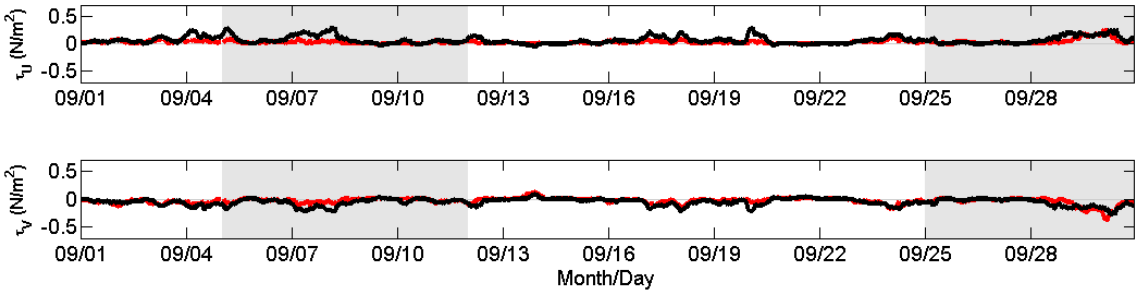

Figure 2.8. September 2009 time-series of U (top) and V (bottom) components of wind stress at Bodega Bay NDBC buoy 46013 (black line) and San Francisco NDBC buoy 46026 (red line). Time periods of interest are shaded grey.

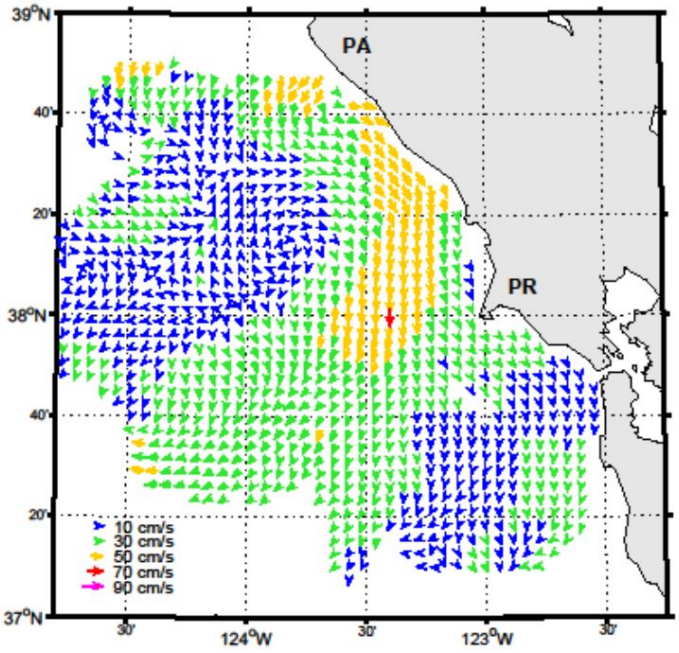

Figure 2.9. Mean HF radar surface current vectors for 7 September, 2009.

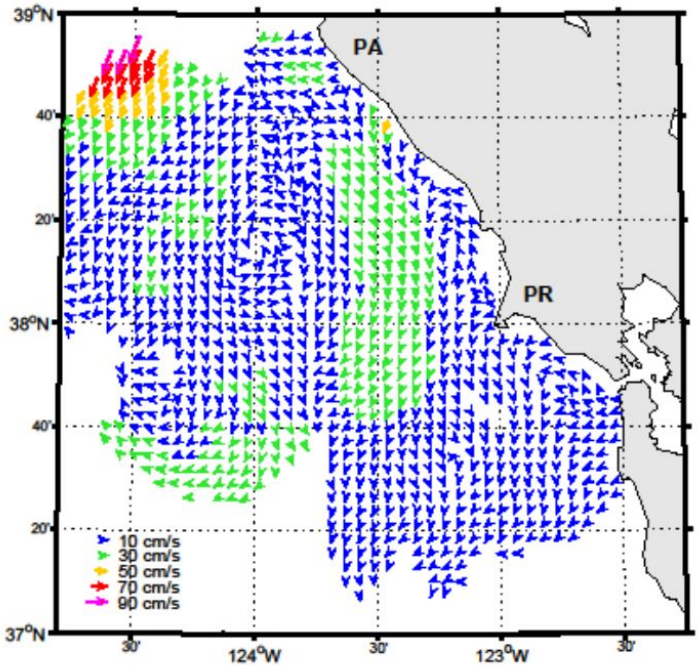

Figure 2.10. Mean HF radar surface current vectors for 27 September, 2009.

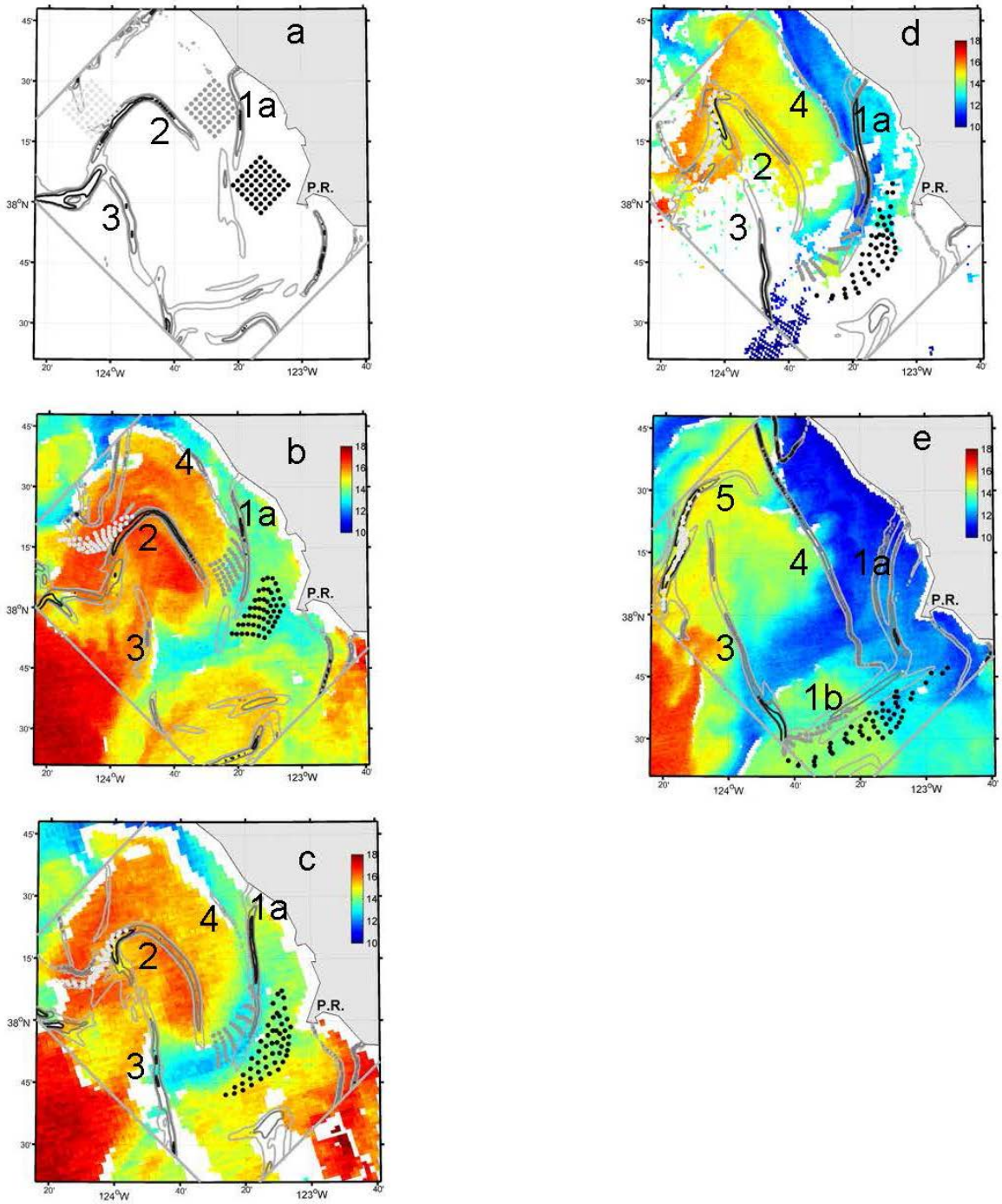

Figure 2.11. FTLE (black and grey contours) overlaid over satellite SST (color image)

Chapter 3

Resonant Near-Surface Inertial Oscillations in the Northeastern Gulf of Mexico

Background

Inertial motions are the oscillatory response of a fluid in motion due to the rotation of the Earth. They are commonly observed in the ocean as clockwise (counter-clockwise) oscillatory currents in the northern (southern) hemisphere superimposed on mean flow. They were originally derived by *Ekman* [1905] as the oscillatory part of the homogeneous ocean's response to wind-forcing on a rotating Earth, the other part being the generation of a depth-veering current with respect to the wind direction. Inertial motions are often found to be transient because they are typically generated by strong wind shifts associated with frontal passages and exponentially decay after the winds subside [*D'Asaro*, 1985; *D'Asaro et al.*, 1995; *Daddio et al.*, 1978; *Pollard*, 1970; *Pollard and Millard*, 1970; *Webster*, 1968]. Inertial motions can also be generated by resonance with relatively weaker forcing at frequencies near the local inertial frequency [*Hyder et al.*, 2011; *Jarosz et al.*, 2007; *Simpson et al.*, 2002; *Webster*, 1968; *Zhang et al.*, 2009; *Zhang et al.*, 2010]. The local frequency of the oscillations, $f(\phi) = 2\Omega sin\phi$, is dependent on latitude, ϕ, where Ω is angular rotation of the Earth.

The critical latitudes for inertial motions are 30° north and south where the local inertial frequency is diurnal (f_d). In the vicinity of these latitudes any near-diurnal forcing that acts upon the ocean can potentially constructively resonate with, and subsequently amplify, near-diurnal oscillations. Therefore, enhanced wind-forced diurnal inertial oscillations are readily observed near the critical latitudes [*Daddio et al.*, 1978; *DiMarco et al.*, 2000; *Hyder et al.*, 2011; *Simpson et al.*, 2002; *Zhang et al.*, 2009]. This

is particularly true in coastal regions where resonance with diurnal sea-breezes can occur. Additionally, diurnal sea-breezes are not just coastline localized phenomena as they have been observed up to 300 km offshore [*Simpson et al.*, 2002; *Zhang et al.*, 2009]. Diurnal tidal forcing can also resonate at the local inertial frequency [*Hendershott*, 1973; *Reid Jr*, 1962; *Seim et al.*, 1987].

By applying a simple model of wind-forced inertial motions that allowed the wind-stress to act solely upon the surface mixed layer, the amount of energy transferred into the inertial motions was found to be dependent on the timing of the winds, the depth of the forced homogeneous surface mixed layer, and the strength of the wind stress [*Pollard and Millard*, 1970]. The energy transferred into inertial motions was not strongly dependent on ocean depth, and surprisingly not strongly dependent on stratification or the horizontal scale of the wind stress. The most efficient transfer of wind energy occurs when the wind direction rotates with the inertial motions or when there is a sudden shift in wind direction provided that unidirectional winds are not sustained longer than half the inertial period. Realistically, not all of the wind energy is transferred into inertial motions of the mixed layer. Some energy is lost to friction, baroclinic instabilities, internal waves, and Ekman transport.

Inertial motions in the northern GoM exhibit seasonal variability where greater energy was observed in the diurnal-inertial band during the summer rather than the winter despite stronger periodic winds in the winter due to frontal passages [*DiMarco et al.*, 2000; *Jarosz et al.*, 2007; *Teague et al.*, 2014]. This was attributed to the relatively thin mixed layer (10 m) accompanied by diurnal wind-forcing in the summer as opposed to the relatively thicker layer (70 m) accompanied by intermittent atmospheric frontal wind-

forcing in the winter.

Because inertial oscillation amplitudes are tied to the depth of the mixed layer, spatial variability of the mixed layer due to freshwater discharge can have a profound effect on the oscillations. The NeGoM has multiple sources of freshwater discharge from inlets, rivermouths, and estuaries. The largest sources of freshwater discharge come from the Mississippi River Delta and the Mobile Bay River system. Discharge from these two sources is greater during the spring and summer compared to the fall and winter [*Morey et al.*, 2002; *Morey et al.*, 2003]. However, increased spatial coverage of discharge over the NeGoM was found to be due to mean northward wind-forcing driving eastward Ekman transport of river discharge and not due to the amount of discharge [*Morey et al.*, 2002].

Inertial oscillations are important for vertical mixing in the ocean by downward inertial wave propagation [*Kunze*, 1985], shear generation at the bottom of the mixed layer [*Zhang et al.*, 2009], creation of divergent and convergent flows from spatial inertial motion variability [*Hyder et al.*, 2011], and coupling with internal tidal currents [*Davies and Xing*, 2003]. The shear generated at the base of the mixed layer by diurnal wind-resonant inertial oscillations can be important for enhanced vertical mixing when moderate wind-forcing is not sufficient to erode strong stratification [*Zhang et al.*, 2009]. They also found that when diurnal sea-breeze driven inertial motions were strongest, the vertical shear increased significantly, the stratification decreased, and the bulk Richardson number decreased.

The tides in the NeGoM are dominated by the K_1 and O_1 diurnal tidal constituents and exhibit a form number of $F > 6$ [*Seim et al.*, 1987] with the exception of

the west Florida Shelf which is dominated by the M_2 tidal constituent. The form number is the ratio of the primary diurnal to semidiurnal constituent amplitudes. Since the K_1 tides are almost at the same frequency as the inertial frequency, the K_1 tidal motions are considered to be inertial at 30°N. Tidal currents along the continental slope and DeSoto Canyon region are observed to be relatively weak, < 5 cm/s [*Jarosz et al.*, 2007], which is in agreement with tidal modeling efforts [*Gouillon et al.*, 2010; *He and Weisberg*, 2002a; *Reid et al.*, 1981]. These tidal models show that over the Mississippi Bight shelf (MBS) tidal currents amplify to approximately 10 cm/s, spatially change phase, and become more elliptical. Harmonic tidal analyses performed on observed near-surface currents over the inner MBS revealed major axis tidal current amplitudes for the K_1 (O_1) to be between 6.0 and 11.9 cm/s (5.3 and 6.7 cm/s), and both the K_1 and O_1 tidal current ellipses rotated anti-cyclonically [*Seim et al.*, 1987]. Diurnal tidal current amplification over the shelf, where they reached 20-30 cm/s, were proposed to be the result of onshore propagating Sverdrup waves due to the similar amplitude of the major and minor axes, the exhibited anti-cyclonic rotation, and dispersive nature of the waves [*Seim et al.*, 1987]. Other causes for the diurnal tidal current amplitude increase over the region could be due to the effects of stratification [*He and Weisberg*, 2002a], the proximity to a large submarine canyon [*Carter*, 2010], and internal tides.

There have been a number of studies on inertial motions off the Louisiana-Texas coast in the western GoM [*Chen et al.*, 1996; *Chen and Xie*, 1997; *Daddio et al.*, 1978; *DiMarco et al.*, 2000; *Zhang et al.*, 2009; *Zhang et al.*, 2010] but there has been only one study that focused on inertial motions in the NeGoM [*Jarosz et al.*, 2007]. *Jarosz et al.* [2007] observed an increase in energy offshore from the shelf break in the DeSoto

Canyon region, although they did not have observations over the shelf or over deep water beyond the continental shelf. They proposed that the decrease in inertial energy at the shelf break could be due to the 30°N turning latitude for internal inertial motions and that the increase in inertial energy over the slope could be related to trapping of near-inertial energy by negative vorticity [*Hamilton et al.*, 2000], offshore propagating internal waves, and/or trapping of energy by fronts. In contrast, *Chen et al.* [1996] observed a maximum of inertial current energy at the shelf break and decreases in energy both offshore and towards shore off the Louisiana-Texas coast.

The region of interest in this study is bounded by the Chandeleur Islands and Mississippi River Head of Passes to the west, the Mississippi-Alabama-Florida coastline to the north, 86.5° W to the west, and 28.5° N to the south (Fig. 1). This includes the northern edge of the DeSoto Canyon and most of the DeSoto Canyon Head (DCH). The continental shelf is relatively broad off the Mississippi Bight where it extends about 100 km offshore to the 100 m isobath. The 100 m isobath then veers onshore to about 40 km offshore demarking the northern extent of the DCH. We identify the DeSoto Canyon as the region deeper than 800 m.

Here, the ubiquitous strong near-diurnal resonant surface currents near the critical latitude for inertial motions (30°N) over the NeGoM are investigated with high frequency (HF) radar-measured 2D near-surface current data obtained in June 2010. The HF radar spatial coverage spans the region between the areas investigated by *Seim et al.* [1987] who attributed diurnal oscillations to tidal currents over the inner shelf, and *Jarosz et al.* [2007] who attributed diurnal oscillations to inertial motions over the continental slope. The first goal is to determine if the diurnal oscillations observed with HF radar are due to

diurnal tidal forcing or the inertial response to wind-forcing. This is done by performing a series of comparative analyses between the predicted inertial response to wind-forcing, predicted tidal currents, and HF radar-observed currents. The inertial response to wind-forcing is calculated by inputting observed wind-stress into a simple "slab" model (see section 2.3). The extensive comparative analysis is necessary because tidal forcing, wind forcing, and inertial oscillations are all nearly diurnal. The near-diurnal oscillations over the MBS and DCH are shown to be predominantly due to wind-forced inertial oscillations and not due to diurnal tidal forcing. The distinction between the influence of inertial oscillations and tidal forcing is important because they vertically mix the water column differently. The second goal is to describe the near-surface spatiotemporal variability of the inertial motions which includes diurnal-inertial signal propagation, frequency shifts, and abrupt phase changes. The spatiotemporal variability of the inertial oscillations are important for inferring how they influence mixing in the NeGoM and how they potentially mixed oil from the Deepwater Horizon spill in June 2010. Relatively smaller near-diurnal oscillations observed in January 2011, presumably due to a deeper mixed layer, are presented as a comparison to summertime conditions and are believed to be due to tidal forcing.

HF Radar Data

Hourly horizontal (2D) near surface current velocities were obtained with three CODAR-type shore-based long-range (~5 MHz) HF radars (station names: HBSP, SGRV, and OBSP) maintained and operated by the University of Southern Mississippi as part of the Central Gulf of Mexico Ocean Observing System (CenGOOS). The radars cover the coastal region between the Mississippi Head, Panama City, and approximately

120 km offshore. HF radar datasets were obtained for June 2010 and January 2011. The focus is on June 2010 data which was during the Deepwater Horizon oil spill. Each radar measures near-surface current velocities towards and away the radar which are commonly referred to as "radials". In this study the radials are processed and objectively combined using CODAR Ocean Sensor software (www.codar.com) to generate "total vectors" which are the hourly $\boldsymbol{u}$ (east-west) and $\boldsymbol{v}$ (north-south) component of near-surface current velocities interpolated onto a 9 km Cartesian grid. The total vectors are the HF radar data used herein. Two points have been selected to represent the MBS and DCH regions of interest for more detailed time series analyses (Fig. 1, pts. A and B).

The fundamentals in the application of HF radar for measuring surface currents are described in numerous studies [*D Barrick*, 1971; 1972; *D Barrick and Lipa*, 1979a; *Stewart and Joy*, 1974]. 5 MHz HF radars measure weight-averaged currents over approximately the top 2.5 m of water. Hereafter, HF radar "near-surface" velocities are referred to as "surface" currents. HF radar measured surface velocities encompass the vector sum of the Eulerian current and the partial Stoke's drift associated with surface gravity waves less than half of the radar wavelength (or Bragg wavelength) [*Ardhuin et al.*, 2009]. Studies on HF radar velocity error have found RMS differences with other types of surface current measuring instruments to range between 3 and 20 cm/s [*Kaplan et al.*, 2005; *Ohlmann et al.*, 2007; *Paduan and Rosenfeld*, 1996]. HF radar error can increase in areas between two radars (baseline error) and areas far offshore due to geometric dilution of precision (GDOP) [*Chapman and Graber*, 1997]. Long-range hourly CODAR HF radar radial vector performance in a low energy environment over the West Florida shelf where the Bragg scatter echo is not strong, similar to the

environment over the NeGoM, was reported to be "quite good" with RMS differences of 6 to 10 cm/s with near-surface ADCP data [*Liu et al.*, 2010].

Wind Stress

Hourly wind velocities were obtained from NDBC buoys 42012 and 42040 that are at 5 and 10 m above sea level, and located within the HF radar domain (Fig. 3.1). Neutral wind stress is calculated using $\vec{\tau} = \rho C_d |w| \vec{w}$ where ρ is the density of air, C_d is the constant drag coefficient, and w is the wind speed at 10 m above sea level [*Large and Pond*, 1981]. Buoy 42012 winds are adjusted to 10 m for the neutral wind stress calculations using a log-layer correction factor. Again, the focus is on June 2010 winds during the Deepwater Horizon spill. Additional wind velocities are analyzed for May-August 2010, and January 2011.

Slab Model of Inertial Oscillation Response to Wind-Forcing

The sea surface inertial current response to wind-forcing is determined with a simple "slab" model following *Pollard and Millard* [1970]. This model has been applied in numerous studies and has exhibited good correlations with observed inertial oscillations [*D'Asaro*, 1985; *D'Asaro et al.*, 1995; *Jarosz et al.*, 2007; *Whitt and Thomas*, 2014]. The model transfers the momentum from wind stress to a vertically uniform surface layer (or "slab") that rides over a stationary layer. First, the horizontal momentum equations of the forced surface layer in the ***u*** and ***v*** direction are combined into complex form ($Z = u + iv$) and written as

$$\frac{dZ}{dt} + ifZ = \frac{T}{H} - rZ \qquad (1)$$

where the wind stress is represented as $T = (\tau_x + i\tau_y)/\rho$, the local Coriolis frequency at latitude Φ is $f = 2\Omega \sin \Phi$, ρ and H are the density and depth of the layer, and r is an

empirically derived "decay parameter". After separating Z into an inertial oscillation contribution and mean Ekman transport velocity contribution, $Z = Z_I + Z_E$, Eq.1 becomes

$$\frac{dZ_I}{dt} + \omega Z_I = -\frac{dZ_E}{dt} - \omega Z_E + \frac{T}{H} \qquad (2)$$

where *r* and *f* are combined as $\omega = r + if$ and the depth of the Ekman layer is assumed to be equal to the depth of the mixed layer. The Ekman transport velocity, $Z_E = \frac{T}{\omega H}$, is known and is removed. In addition the depth of the layer is assumed to remain constant such that $\frac{d}{dt}\left(\frac{1}{H}\right) \cong 0$. An expression for the complex inertial response due to wind forcing, Z_I, is attained by:

$$\frac{dZ_I}{dt} + \omega Z_I = -\frac{dT}{dt}\frac{1}{\omega H}. \qquad (3)$$

Z_I can then be solved iteratively by inserting the complex form of the hourly wind stress, *T(t)*, from buoys 42012 and 42040 into the following:

$$Z_I(t+1) = Z_I(t) - dt\left[\omega Z_I(t) + \frac{T(t+1) - T(t)}{dt}\frac{1}{\omega H}\right]. \qquad (4)$$

Hereafter, the calculated inertial response to wind stress obtained by buoy 42012 (42040) is referred to as Zi_{12} (Zi_{40}) where the subscripts 12 and 40 are the last two digits of the buoy numbers. *Zi* is used when referring to both Zi_{12} and Zi_{40}.

Typically the model is applied to the turbulent mixed layer developed by wind stress. We apply this model to a surface layer representing the lower density semi-freshwater discharge that typically extends over much of the NEGoM. Model simulations were performed with a time step of 15 minutes using a linear interpolation for the hourly wind stress. The damping term was set at $r = f/\pi$ which is consistent with previous work

that stipulate that $r<<f$, and that $1/r$ be between 1 and 10 days [*D'Asaro*, 1985; *Pollard and Millard*, 1970; *Whitt and Thomas*, 2014]. Using smaller time steps did not lead to significantly different results.

The depth of the surface forced layer, H, in the inertial oscillations model, is estimated to be approximately 8-10 m which is based on shipboard ADCP measurements and CTD casts obtained during the Grand Lagrangian Deployment (GLAD) in July 2012 [*Poje et al.*, 2014]. During GLAD across-shelf shipboard ADCP transects within the HF radar domain were performed, and multiple CTD casts beyond the continental shelf and over the DeSoto Canyon were obtained (not shown). Strong ADCP echo intensity vertical gradients identify the bottom of the turbid surface layer and strong shear identifies the bottom of the mixed layer (not shown). The depth of the two types of measurements consistently agreed indicating that the depth of the turbid discharge water is the same as the depth of the mixed layer. This was corroborated with the CTD casts. Thus, the turbid discharge layer is the surface mixed layer which represents the surface forced layer in the inertial model. The 8-10 m depth is also in agreement with climatology [*Dzwonkowski and Park*, 2012], and observations from Spring and Summer 1997 [*Jarosz et al.*, 2007]. It should be noted that inter-annual discharge variability can affect the depth of the forced layer and inertial oscillation amplitudes [*Zhang et al.*, 2009]. A source of error in the Zi calculations is associated with assuming the depth of the surface layer to be constant and equivalent to the depth of the Ekman layer. For example, the cause of Zi oscillation amplitudes to be greater than observed amplitudes could be due to an underestimation of Z_E which, in turn, could be due to an underestimation of H.

Tidal Current Predictions

Barotropic tidal currents are determined using the Oregon State University Tidal Inversion Software (OTIS) (http://volkov.oce.orst.edu/tides/). Tidal current predictions show spatial amplitude and phase variability likely due to the complex coastline and bathymetry. But, the complex bathymetry, particularly in the DeSoto Canyon region, brought the OTIS performance into question since a higher resolution tidal model may be required to more accurately resolve tidal motions here. It was therefore necessary to compare OTIS predictions with previous tidal model studies and nearby tidal observations. Overall, OTIS K_1 and O_1 tidal current phase and amplitude variability compares well with barotropic tidal model predictions [*Gouillon et al.*, 2010; *He and Weisberg*, 2002a; *Reid et al.*, 1981]. The tidal models models, including OTIS, exhibit an amplification of the O_1 and K_1 tidal currents over MBS where their respective amplitudes are approximately 5 cm/s and at the height of the spring tidal cycle they constructively interfere to attain amplitudes of approximately 10 cm/s. Further confidence in the OTIS tidal predictions came from comparisons with tide gauge sea level heights. Sea level height observations at NDBC stations 8760922 (Pilots Station East, SW Pass), 8735180 (Dauphin Island), and 8729210 (Panama City Beach) compared surprisingly well with OTIS despite their proximity to the coastline where OTIS prediction accuracy is expected to decline. Most importantly, amplitudes compared well but there were discrepancies with the phase.

Classical harmonic tidal analysis was performed on the HF radar data but is not reported since we suspect it to be ineffective in properly separating out the diurnal tidal motions from the diurnal inertial motions in the NeGoM. Firstly, because the time length

of our HF radar data is not long enough to separate out the K_1 and O_1 tidal frequencies. Secondly, in the two months investigated here, the inertial response to wind-forcing frequently aligned with the predicted spring tidal oscillations which would corrupt harmonic analyses.

June 2010 Mean Flow

Mean surface velocities exhibited general eastward flow, enhanced flow along the outer and inner continental shelf, and northward flow north of the DCH (Fig. 3.2). Weaker mean flow occurred over the middle of the MBS, eastern portions of the domain, and the southeastern DCH region. In general the HF radar velocities are in agreement with previous work on circulation in the region [*He and Weisberg*, 2002a; b; *Hsueh and Golubev*, 2001; *Smith and Jacobs*, 2005; *Wang et al.*, 2003; *Weisberg et al.*, 2005; *Yuan*, 2002] although these studies generally found jet-like surface flow to exit the region towards the southeast following the 100 m isobath. Daily mean flow patterns (not shown), along with mean flow for June 2010 (Fig. 3.2), reflect Ekman transport dynamics by exhibiting flow to the right of the wind direction. Thus, the June 2010 mean winds from the southeast enhance existing surface flow entering the domain from the southwest which follows the 50m isobaths just inside of the edge of the continental shelf and is directed across isobaths and onshore at the northern extent of the DCH. This flow pattern is corroborated by observed June 2010 surface oil from the Deepwater Horizon spill that was transported eastward along the continental slope and eventually across the shelf and onto the beaches north of the DCH [*Dietrich et al.*, 2012]. *Yuan* [2002] attributed cross-isobath onshore flow at the DCH to bottom-Ekman transport in response to strong along-isobath flow in combination with an off-shore pressure gradient (although, in their case

wind-forcing was from the north and during the winter). *Huh et al.* [1981] attributed onshore flow at the DCH to intrusions of the Loop Current.

Wind Forcing

Since the inertial oscillations are hypothesized to be wind driven, the temporal phasing of wind stress is of particular importance. This is true with the phasing of wind shifts associated with atmospheric frontal passages, and the frequency of periodic wind-forcing that can resonate with inertial oscillations. Additionally, the greatest resonant response to wind-forcing occurs when the winds rotate along with the inertial oscillations. Rotary spectral analysis [*Gonella*, 1972] is therefore useful in studying inertial motions because it separates the CW and CCW rotational frequency spectra of a complex velocity time series. Significant spring-summer diurnal CW and CCW wind energy peaks were found over the Texas-Louisiana shelf [*DiMarco et al.*, 2000] and over the DeSoto Canyon region [*Jarosz et al.*, 2007] using rotary spectra. Both of these studies observed greater diurnal energy in the CW direction and less diurnal energy during winter months that corresponded with less ocean current near-diurnal energy compared to the summer.

June 2010 winds at buoys 42012 and 42040 exhibited occasional wind shifts most likely associated with atmospheric frontal passages, and brief periods of near-diurnal pulses (not shown). Rotary spectra show greater energy in the CW direction, an increase in energy towards lower frequencies, and multiple peaks between 1 and 3 cpd (Fig. 3.a and b). Even though there is not a significant diurnal peak, there is still sufficient energy across the diurnal band to excite a resonant diurnal-inertial response of the ocean. Because a significant diurnal wind energy peak was not observed in June 2010, rotary

spectra was performed on wind stress from buoys 42012 and 42040 for an extended time period, May-August 2010 (not shown). These rotary spectra exhibited a significant CW peak at f_d as observed by *Jarosz et al.* [2007] indicating that diurnal wind energy was anomalously weaker than normal in June 2010.

Buoy 42040 winds, being 60 km from the Mississippi Head and 110 km from the Alabama coastline, exhibited similar diurnal energy as buoy 42012 which is only 20 km from the coastline. There was also evidence that diurnal winds can occasionally be strongest in the early morning. These observations counter the typical diurnal seabreeze convention that winds initiate in the afternoon and are localized along the shoreline. However, it is not unprecedented for diurnal winds to be observed far offshore [*Simpson et al.*, 2002; *Zhang et al.*, 2009], and that diurnal seabreeze timing be out of phase with convention south of 30°N in the northern hemisphere [*Rotunno*, 1983; *Yan and Anthes*, 1987; *Zhang et al.*, 2009].

HF Radar Observed Diurnal Surface Current Oscillations

As observed by *Jarosz et al.* [2007], large diurnal-inertial oscillations are expected in the NeGoM due to diurnal wind-forced resonance at the local inertial frequency. A good indicator of inertial oscillations in the NeGoM would therefore be large coherent CW-rotating near-diurnal motions. June 2010 surface currents were dominated by near-diurnal oscillations as diurnal band [0.89 – 1.11 cpd] variance accounted for at least 75% of the total variance over much of the domain (Fig. 3.2). Oscillation amplitudes typically ranged between 20-40 cm/s and notably large oscillations reached amplitudes of approximately 45-65 cm/s over the MBS on 4-5 June (Figs. 3.4 and 3.5) and 70 cm/s at the southern edge of the MBS on 11-16 June (Fig.

3.5.c). Over the DCH region north of 30°N, the ***v***-component of the oscillations exhibited large amplitudes of approximately 50 cm/s during the middle of the month (Fig. 3.6). Overall, mean flow was much smaller than the observed oscillations and ranged between 0-20 cm/s (Fig. 3.2). The oscillations predominantly rotated clockwise which is exemplified by the CW diurnal peak in rotary spectra at points A and B (Fig. 3.3.c and d). The DCH exhibited diurnal energy peaks in the both the CW and CCW directions although the CCW peak is an order of magnitude smaller (Fig. 3.3.d).

Because the oscillations are nearly diurnal and dominate the circulation in the NeGoM, percent of total variance ellipses in the diurnal band reflect the general shape of the oscillations. Following this reasoning, since Poincaré waves exhibit vector ellipses of major/minor axis ratio ω/f, frequency band variance ellipses can reflect the orientation of Poincaré waves as long as ω and f are within the frequency band. Likewise, circular variance ellipses can be used to identify and describe purely inertial motions. Variance ellipses were mostly circular indicating that the CW rotating current vectors were of equal magnitude in all directions (Fig. 3.2). Exceptions occurred over the inner shelf, particularly north of the DCH, where variance ellipses were elongated north-south, and the eastern region of the DeSoto Canyon where diurnal band variance decreased and ellipses were slightly elongated. The relatively greater cross-shore variance, compared to alongshore variance, along the inner shelf is influenced by periods of time when ***u***-direction oscillations were suppressed rather than a persistent suppression of ***u***-direction oscillations (Fig. 3.7.b). Over the middle of the MBS the circulation is uniquely dominated by CW rotating diurnal oscillations as mean flow was small while variance ellipses were circular and large.

Hövmöller diagrams are useful in identifying oscillatory signal propagation and abrupt spatiotemporal shifts. Considerable spatiotemporal variability in the diurnal oscillations can easily be observed the Hövmöller diagrams (Figs. 3.4, 3.5, and 3.6). We therefore focus on the most notable characteristics. With a few exceptions, there is a general offshore propagation of the diurnal oscillations between 11-20 June (Fig. 3.6). The MBS and DCH regions oscillated asynchronously on 13-15 June when the MBS oscillations in the ***u***-direction lagged behind the DCH region (box A, Fig. 3.4a), and on 24-27 June when MBS oscillations led the DCH region (box B, Fig. 3.4). The abrupt phase differences at the interface between the regions of asynchronous oscillations are delineated by approximately 87.5°W longitude.

Point-wise Comparisons between Slab Model Oscillations (*Zi*) and HF Radar Surface Currents

Comparisons between *Zi* and observed oscillations at pts. A and B (Figs. 3.7 and 3.8) are used to determine whether the diurnal oscillations are a response to wind forcing and gain insight into the performance of the slab model. Overall, Zi_{12} oscillations better represent the surface currents over the entire domain than Zi_{40} oscillations as linear regression results comparing HF radar currents at pts. A and B with Zi_{12} produced R^2 values between 0.24 and 0.60, and slopes ranged between 0.50 and 0.90 (Table 3.1). The best fit with Zi_{12} occurred at pt. B in the ***v***-direction and the best fit with Zi_{40} occurred at pt. A in the ***v***-direction. It is not surprising that Zi_{12} better represents the oscillations since buoy 42012 is near the middle of the domain and buoy 42040 is near the southwest edge. The linear regression results may seem poor despite the apparent similarities that can be observed between observed currents and *Zi* in figures 3.7 and 3.8, but it is important to

consider that linear regression analysis is sensitive to small phase differences when comparing oscillatory signals. In addition, since pt. A is between buoys 42040 and 42012 there are times when Zi_{40} best represents the oscillations over the MBS, and times when Zi_{12} best represent the oscillations over the MBS which is another reason why the HF radar surface current linear regression results with Zi_{12} and Zi_{40} at pt. A were mediocre. Running linear regression analyses (performed on overlapping 3-day sections of data every 1.5 days) between *Zi* and HF radar currents at pt.A show that at the beginning of the month linear fits were relatively good with Zi_{12} (Fig. 3.9.a and b) compared to Zi_{40} (Fig. 3.10.a and b), based on R^2 values and slopes. Near the end of the month linear fits with Zi_{40} were better than those observed with Zi_{12}. Over the middle of the month linear fits were good with both Zi_{12} and Zi_{40}, and at the very end of the month linear fits decreased with both Zi_{12} and Zi_{40} which was most likely due to strong wind shifts causing the *Zi* calculations to misrepresent the ocean response to wind-forcing.

Synoptic Slab Model Oscillations (*Zi*) and HF Radar Surface Currents Comparison

Spatial cross-correlation analysis provides insight into where and when correlations and time lags occur between *Zi* and observed near-diurnal surface current oscillations. Spatial variability of the time lags can also indicate propagation or spatial frequency variability of near-diurnal oscillations. June 2010 spatial normalized cross-correlations between Zi_{12} and HF radar surface currents ranged between 0.5 and 0.8 in the ***v***-direction and 0.1 and 0.7 in the ***u***-direction (Fig. 11.b and d), and surface currents generally led Zi_{12} by 0 to 3 hours (Fig. 11.a and c).

Over the DCH region there is a ***u***-direction (***v***-direction) progressive time lag difference of 2-3 hours from northwest to southeast (northeast to southwest) which is

indicative of diurnal oscillation propagation (Fig.11.a and c). The northeast and southeast corners of the domain exhibit sharp decreases in ***u***-direction correlations but not in the ***v***-direction.

Over the MBS, normalized correlations decreased to approximately 0.5 along the western edge of the HF radar domain (Fig. 11.c and d), and there is a ***u***-direction (***v***-direction) progressive time lag difference from the northwest corner of the MBS to the southeast (west to east) which is indicative of northwest to southeast propagation (Fig.11.a and d).

Cross-correlation analyses performed over three 10-day sections of time similar to figure 11 (not shown) captured the temporal evolution of the correlations. The reduced record length of the sections of time compromised confidence limits due to a decrease in the number of observed diurnal oscillations which reduce degrees of freedom (the 10% level of confidence was 0.5). Nonetheless, 10 day cross-correlations between Zi_{12} and Zi_{40} with HF radar observations provided valuable insight. For approximately the first 10 days of the month only Zi_{12} was well-correlated with observations where normalized correlations were above 0.7 over much of the domain and time lags ranged between 0 and $^{+}3$ hours. For the second 10 days, both Zi_{12} and Zi_{40} were well-correlated (mostly above 0.7) and time lags for Zi_{12} ranged between $^{-}1$ and $^{+}1$ while time lags for Zi_{40} ranged between $^{+}2$ and $^{+}4$. For the last 10 days Zi_{40} correlations were significant over most of the MBS (0.5 – 0.6, time lags of 0 – $^{+}2$ hours) but not over the DCH. In contrast, Zi_{12} correlations were good over most of the DCH (0.6 – 0.8, time lags of $^{+}2$ - $^{+}4$ hours) and diminished over the MBS.

Diurnal Complex Demodulation of *Zi* and HF Radar Measured Surface Currents

Complex demodulation has been used to successfully identify and describe near-inertial motions in previous studies including *Jarosz et al.* [2007], *Perkins* [1976], and

Simpson et al. [2002]. The method is well-described in *Emery and Thomson* [2001] and is applied by performing a least-squares fit between observed current vectors in complex form as a function of time, $u(t) + iv(t)$, and a fabricated fixed amplitude vector in complex form rotating CCW and CW in time ($A\ exp(i\omega t)$ and $A\ exp(-i\omega t)$) where A is the amplitude of the vector and ω is the frequency. The results return a phase and amplitude where the phase represents the phase difference between the two signals and the amplitude is used to determine when the phase is valid. By performing complex demodulation analysis on intervals of time along a complex vector time series, a record of the evolving phase difference can be used to determine the evolving frequency of the time series oscillations in relation to ω. A negative (positive) temporal trend in the phase implies an observed signal frequency greater (less) than ω. We performed diurnal complex demodulation on overlapping 24 hour sections of observed HF radar currents every 12 hours with a fixed amplitude vector that rotated diurnally ($\omega = f_d = 24^{-1}$ hrs^{-1}). A minimum threshold of 10 cm/s in the amplitude is arbitrarily used to determine when the phase is valid. Because the diurnal oscillations in the NeGoM are predominantly CW, CCW complex demodulation results are insignificant and therefore not reported.

June 2010 diurnal complex demodulation applied to Zi_{40} do not exhibit notable trends in the overall phase slope when amplitudes were significant indicating that the Zi_{40} frequency is nearly diurnal (Fig. 12.a and b). This was particularly true after 9 June. Note that abrupt phase shifts typically occurred when amplitudes decreased below the 10 cm/s threshold which is to be expected. Diurnal complex demodulation applied to Zi_{12} shows that the Zi_{12} frequency is also nearly diurnal for the first 8 days of the month, but a negative phase slope thereafter indicates that the frequency became shifted slightly higher

than f_d. The shifts toward higher frequencies for Zi_{12} are surprising for three reasons: 1) The local inertial frequency (f) used in the Zi_{12} calculation is very nearly diurnal, 2) there is no significant wind-stress energy peak in the rotary spectra slightly higher than f_d (Fig. 3.b), and 3) *Pollard and Millard* [1970] state that the *Zi* frequency response should be slightly lower than f when the forcing frequency spectra is flat. Note, however, that there is a small energy peak slightly higher than f_d at buoy 42012 (Fig. 3.b). As observed, the Zi_{40} frequency response is expected to be lower than Zi_{12} due to the latitudinal difference between the two buoys, but like Zi_{12}, it is higher than expected.

The temporal frequency variability in the HF radar surface current oscillations at points A and B generally mirrored that of Zi_{12} which is supported by their respective phase changes in figure 12. The negative phase slope for both *Zi12* and observed oscillations after 10 June is estimated to be -15°/day which translates to a frequency of 1.043 cpd (or a 4% super-inertial frequency shift from f_d). The super-inertial shift in the surface currents is corroborated by energy at frequencies slightly greater than *fd* in surface current rotary spectra (Fig. 3.a and b).. An observed global super-inertial frequency shift from the local f in inertial oscillations is well documented and attributed to the dispersive properties of freely propagating internal-inertial waves on a β-plane [*Elipot and Lumpkin*, 2008; *Elipot et al.*, 2010; *Fu*, 1981; *Chris Garrett*, 2001]. *Elipot et al.* [2010] observed a 2.5% super-inertial shift between 30° N(S) and the equator which was speculated to be due to the β-effect of internal-inertial waves constrained to equatorward propagation. They noted, however, that they were unable to discount the influence of local atmospheric forcing. The simultaneous super-inertial shift in Zi_{12} and surface oscillations after 10 June, along with the overall super-inertial shift from f in Zi_{12}

and Zi_{40}, suggests that wind forcing is contributing to the super-inertial shift in the surface oscillations at this time in the NeGoM.

Because the June 2010 super-inertial shift in Zi_{12} was unexpected, diurnal complex demodulation on *Zi* was extended to include May – August 2010 (not shown). The frequencies of *Zi*, particularly Zi_{12}, were found to not be fixed and exhibit periods of diurnal frequency response along with periods of super-inertial shifts as observed in June 2010. This shows that, as expected, there is a propensity for wind-forcing and the inertial response to wind-forcing at the critical latitude to exhibit an energy peak at f_d which is in agreement with *Jarosz et al.* [2007], but there is also a tendency for the oscillations to be shifted towards higher frequencies.

Determination of Wind-forced Inertial Oscillations

The ubiquitous summertime near-diurnal oscillations in the NeGoM must first be determined to be predominantly due to the inertial response to wind-forcing, rather than diurnal tidal forcing, before further investigation. This is performed through the following series of comparative analyses between observed HF radar surface currents, *Zi*, and OTIS tidal current predictions: objective time series comparisons, linear regression analyses, spatial cross-correlation analyses, and complex demodulation analyses. The analyses presented in sections 2 and 3 are necessary because the inertial, tidal, and wind-forcing frequencies are all nearly diurnal. Harmonic analyses alone cannot resolve such small frequency differences unless considerably longer time series are used. In addition, the OTIS predicted spring tide and the calculated *Zi* oscillations frequently align with the observed HF radar surface current oscillations, and as previously mentioned, a higher resolution tidal model may be required to resolve the tidal currents. If OTIS and the

results from previous tidal model studies are correct [*Gouillon et al.*, 2010; *He and Weisberg*, 2002a], then the barotropic tidal current amplitudes over the MBS (typically less than 12 cm/s) are relatively small compared to the surface current diurnal oscillations during the summer months. There are a numerous causes that can shift the phase or frequency of inertial oscillations and thus produce discrepancies between *Zi* and observed oscillations: errors in wind-stress calculations due to highly variable winds and atmospheric stratification, local wind-forcing recorded at the buoy from thunderstorms or wind-shifts along atmospheric fronts that are not representative of wind-forcing over the domain, HF radar error, phase shifts due to barotropic and baroclinic tidal forcing, frequency shifts due to relative vorticity and advective Doppler shift [*Kunze*, 1985; *Mooers*, 1975; *Perkins*, 1972; *Pollard and Millard*, 1970; *White*, 1972], the tendency for *Zi* to predict a frequency less than *f* while the true ocean response is influenced by the Brunt-Väisälä frequency which shifts the frequency higher than *f* [*Pollard and Millard*, 1970], near-diurnal Helmholtz resonance [*Platzman*, 1972; *Reid et al.*, 1981], internal waves generated at the coastline [*Millot and Crépon*, 1981], and a positive frequency shift due to the dispersive properties of freely propagating near-inertial waves.

Subjective visual comparisons of time series reveal some of the subtle similarities between *Zi* and surface current variability that are difficult to assess with objective methods. Overall, June 2010 *Zi* oscillatory time series variability compared favorably to HF radar data while OTIS tidal predictions drift in and out of phase and under-predict the amplitudes (Figs. 7 and 8). Oscillation matches between Zi_{12} and HF radar were better at pt.B than at pt.A (Fig. 7), which is reflected in linear regression fits in table 1. Minor discrepancies with Zi_{12} at pt.A in June 2010 occurred between days 17-21 and continued

to the end of the month when Zi_{12} oscillations decreased, which is reflected in the running linear regression analysis (Fig. 9). The decrease in the Zi_{12} oscillation amplitudes between 7-11 and 25-28 June matched the decrease observed over the DCH region at pt.B, particularly the ***v***-component (Fig. 7.b). The surface oscillation linear regression results at pt. A for Zi_{12} and Zi_{40} (Table 1) are not as high as expected due to the combined influence of wind forcing at the two buoys such that occasionally Zi_{12} better represented the oscillations over the MBS while at other times Zi_{40} better represented the oscillations. This can be seen in time series comparisons and running linear regression comparisons where Zi_{12} matches HF radar oscillations at the beginning of the month (Figs. 7.a and 9) and Zi_{40} matches HF radar oscillations near the end of the month (Figs. 8 and 10).

Normalized cross-correlations between Zi_{12} and HF radar surface currents were good, ranging between 0.6 and 0.8 over most of the domain with some exceptions (Fig. 11.c and d). By comparison, correlations with OTIS tidal predictions were relatively poor, ranging between 0.1 and 0.6 (not pictured).

The diurnal complex demodulation phase changes of HF radar surface currents and Zi_{12} are small at the beginning of June 2010 and simultaneously decrease at approximately -15°/day after 8 June (Fig. 12.a and c). The timing and magnitude of the negative phase slope in both Zi_{12} and surface currents indicate that the frequency shift is largely due to the inertial response to wind-forcing rather than the numerous other mechanisms that can shift the frequency. In contrast, diurnal complex demodulation phase change of the predicted tides (not shown) increases with time since the resulting tidal frequency of the K_1 and O_1 interference is slightly less than diurnal.. The phase change of Zi_{12} after June 8 is relatively constant in comparison to the phase changes

observed in the HF radar oscillations. These discrepancies are likely due to the numerous other mechanisms that can shift the frequency of inertial oscillations.

Due to a much deeper forced layer, winter wind-driven inertial oscillation magnitudes are expected to be smaller than those during the summer. With the influence of wind-driven oscillations diminished, insight into how well OTIS is predicting the tides is possible. January 2011 HF radar ***v***-component surface current time series at pt. A compare favorably to OTIS tidal current predictions (Fig. 13) and linear regression results returned $R^2 = 0.37$ and slope = 0.27. The oscillations are smaller than those observed during the summer and match the spring-neap cycle from O_1 and K_1 tidal interference. The reasoning here is that if OTIS is accurately predicting the amplitudes of the barotropic tidal currents during the winter when there is little influence from wind-driven inertial oscillations, then we can have greater confidence in the OTIS tidal predictions during June 2010. The observed ***u***-component oscillation amplitudes exhibited greater variability and did not match the small ***u***-component tidal currents predicted by OTIS. It is not clear why OTIS under-predicts the ***u***-component amplitudes. January 2011 spatial plots of the diurnal band percent total variance (not shown) exhibited the expected spatial tidal influence predicted by OTIS and previous modeling efforts [*Gouillon et al.*, 2010; *He and Weisberg*, 2002a] where ***v***-component diurnal band variance increases over the MBS west of 87.75°W.

Spatiotemporal Variability of Inertial Oscillations

There is little evidence from the June 2010 HF radar data of the sharp increase in CW diurnal band variance over the slope south of the MBS observed by *Jarosz et al.* [2007]. Due to drop-offs in HF radar coverage, diurnal band variance is not investigated

in this region. However, with diurnal band variance over the MBS reaching 80% (Fig. 2) it is unlikely that there would be a significant increase in variance over the slope. The sharp CW variance gradient south of the MBS observed by *Jarosz et al.* [2007] occurred at about 29.2°N. In this region, enhanced oscillations south of 29.5°N on 11-16 June, and at 29.2°N where oscillation amplitudes decreased to the north and south on 21-29 June can be observed in Figure 5.c. The enhanced oscillations on 11-16 June may simply be due to strong eastward flow coupled with the Coriolis response which does not necessarily imply an increase indiurnal band variance. The enhanced oscillations on 21-29 June are in agreement with *Chen et al.* [1996] who observed an inertial oscillation maximum at the Texas-Louisiana shelf break with decreases to the north and south. Over the DCH, the gradual offshore and onshore decrease in diurnal band variance from the 100-200 m isobaths (Fig. 2) is also in agreement with *Chen et al.* [1996], and in disagreement with *Jarosz et al.* [2007] who observed a gradual offshore increase in CW variance from the 200 m isobath. There are a number of reasons why our observations disagree with *Jarosz et al.* [2007]. Our analysis time interval is shorter, and there are occasional HF radar coverage drop-offs over the southern edge of the MBS. Strong shear at the bottom of the pycnocline generated by inertial oscillations could be responsible for discrepancies between HF radar observations, which measured the top 2.5 m of the water column, and the ADCPs used by *Jarosz et al.* [2007], which measured currents below 8-18 m. These ADCP measurements did not include most of the surface forced layer which is typically 8-10 m during the summer. Additionally, inter-annual or seasonal variability in the spatial extent of semi-freshwater discharge can influence the depth of the forced layer and subsequently influence spatial variability of the inertial oscillations.

Propagation of the diurnal-inertial oscillation signals can be identified by spatial changes in cross-correlation time lags, and by diurnal signal tilts in the Hövmöller diagrams. The cross-correlation time-lag analysis suggests that the ***u***-direction (***v***-direction) diurnal-inertial signal generally propagates from northwest to the southeast (west to east) over the MBS, and from northwest to southeast (northeast to southwest) over the DCH (Fig. 11.a and b). The propagation speeds of the diurnal-inertial signals are roughly estimated to range between 3-8 m/s from the cross correlation analyses. Propagation speeds were estimated to be 0-15 cm/s from the Hövmöller diagrams (Figs. 4-6). Propagation directions from these diagrams generally agreed with propagation directions in the cross-correlation analyses. Over the DCH region there is diurnal-inertial signal offshore propagation from the 100 m isobath between 11-20 June, which is connected to the enhanced inertial oscillations north of 30°N (Fig. 6). There is also an abrupt decrease in the offshore propagation speed at the 100 m isobath (at approximately 29.5°N) south of the MBS between 22-30 June (Fig. 5) which is associated with an abrupt phase change in the oscillations. Changes in the characteristics of the inertial motions along the 100 m isobath could be due to spatial stratification variability along with vorticity and/or Doppler-shift effects associated with strong eastward jet-like flow along the MBS break that gradually weakens and fans out over the DCH. The diurnal signal propagation implies Poincaré wave propagation where they are allowed to propagate freely south of 30°N [*Zhang et al.*, 2010] but it can also imply spatial variability in the inertial response to wind-forcing.

The enhanced diurnal inertial oscillations (amplitudes ≈ 50 cm/s) north of 30°N at the DCH are predominantly rectilinear, oriented across-shore (Fig. 6), and aligned with

the mean onshore transport in this region (Fig. 2). The enhanced amplitudes could be due to trapping of Poincaré waves north of 30°N [*Zhang et al.*, 2010], or trapping due to negative vorticity [*Kunze*, 1985] associated with inner-shelf alongshore flow. Both of these processes can potentially enhance vertical mixing in the region. They likely not tidal as the spring-neap cycle of K_1- O_1 interference is not observed, tidal currents are expected to be small [*He and Weisberg*, 2002a], and $\boldsymbol{v}$-component correlations with *Zi* are good (Figs. 7.b, 12, and Table 1).

Inertial oscillations over the MBS occasionally migrate out of phase with those over the DCH. This occurs on 12-16 June where there is an abrupt zonal shift in oscillations that occurs at approximately 87.5°W (Fig. 4.a, Box A), and on 22-30 June where there is a more gradual shift in the oscillations (Fig. 4, Box B). The processes responsible for the two cases are different. The former case is due to a discontinuity in the west-east diurnal signal propagation. Zi_{12} and Zi_{40} are in phase at this time (Figs. 7 and 8) which suggests homogeneous wind-forcing over the domain. The latter case is more likely due to spatiotemporal variability in wind-forcing and consequentially the inertial response. On 22-30 June, Zi_{12} and Zi_{40} are out of phase (Figs. 7 and 8). Not only are Zi_{12} and Zi_{40} are out of phase at this time, but Zi_{40} better describes the oscillations over the MBS (Fig. 8) and Zi_{12} better describes the oscillations over the DCH (Fig. 7.b) as indicated by linear regression R^2 and slope values (Figs. 9 and 10). Another influence on such abrupt inertial oscillation spatiotemporal variability could be due to spatial differences in stratification as the MBS is closer to larger sources of semi-freshwater discharge. Abrupt changes in inertial oscillation variability can initiate vertical motions due to surface divergence and convergence which can enhance vertical mixing [*Hyder et*

al., 2011]. Based on the above observations, this type of enhanced vertical mixing in June 2010 most likely occurred near 87.5°W, which roughly separates the MBS and DCH regions. The previously mentioned abrupt phase change at the southern edge of the MBS between 22-30 June (Fig. 5) is another region where this type of mixing occurred.

Periods of ***u***-component oscillation suppression over the northern DCH, while ***v***-component oscillations are not suppressed, suggests some other type of mechanism related to the inertial response to wind-forcing. These nearly rectilinear oscillations can be seen between 10-20 June at pt.B (Fig. 7.b (top)), in the Hövmöller diagrams from 9-14 and 26-30 June (Fig. 6.a), and are reflected in the ***u***-component correlation decrease along the eastern region of the domain (Fig. 11.c). The oscillations are likely not tidal because ***v***-component Zi_{12} oscillations clearly match observed oscillations (Fig. 7b (bottom)). However, the suppressed ***u***-component of the oscillations are not expected for inertial motions (or Poincaré waves). Poincaré waves exhibit eccentric surface current vector ellipses with major/minor axes represented by ω/f where $\omega \geq f$. In this case the episodic rectilinear oscillations were diurnal such that the major axes were represented by f. This would imply that $\omega < f$ which is not supported by the dispersion relationship for Poincaré waves. It is not known what is causing the ***u***-direction suppression of the oscillations although it could be related to internal waves generated by inertial motions impacting the coastline.

Summary and Concluding Remarks

We have demonstrated that the ubiquitous summer (June 2010) near-diurnal oscillations observed in the NeGoM are predominantly due to the inertial response to wind-forcing and not due to diurnal tidal currents. The distinction between these two

processes is important because they vertically mix the water column very differently. The unusually large inertial oscillations are due to resonance at the critical latitude for inertial motions in combination with a shallow forced layer associated with strong stratification. During the winter (January 2011), presumably when there is a deep mixed layer, the near-diurnal oscillations are more likely to be attributed to tidal forcing, particularly over the MBS. Additionally, we have presented a unique spatiotemporal view of the wind-driven inertial currents which are used to identify regions of potential mixing enhancement in the NeGoM. Three regions in the NeGoM were identified where oil from the Deepwater Horizon spill was potentially subjected to vertical mixing by inertial motions: North of 30°N at the DCH, along 87.5°W, and along the southern edge of the MBS at 29.7°N.

The inertial oscillations were large in comparison with mean flow and exhibited considerable spatiotemporal variability. The observed oscillation frequency was essentially diurnal for the first 10 days of June 2010 before shifting to approximately 1.043 cpd, thereafter. The shift was attributed, in part, to a shift in the inertial response to wind-forcing.

The MBS is characterized by large inertial motions, very little mean flow over the middle of the shelf, and high percent of total variance in the diurnal-inertial frequency band. Diurnal band variance ellipses are circular indicating that the oscillations are almost purely inertial. Some of the strongest diurnal oscillations occurred at the southern region of the MBS reaching amplitudes of 80 cm/s. The diurnal signal of the oscillations generally propagated from west to east.

Over the DCH there is a gradual decrease in diurnal band variance toward the north and south from the 100-200 m isobath region. The oscillations generally propagated

southward. Periods of north-south oriented rectilinear oscillations were observed over the northern extent of the DCH where mean flow was northward.

Although the diurnal oscillations were found to be predominantly due to the inertial response to wind-forcing, there are discrepancies. Changes in inertial motion characteristics, particularly where there is west-east flow along the 100 m isobath coupled with strong stratification, suggests that this region is well-suited for investigating the effects of vorticity, Doppler shift, and stratification on inertial waves. Another likely candidate for additional diurnal current variability is internal tides due to typically strong stratification in combination with a wide range of continental slope angles. Tidal focusing in the DeSoto Canyon and Sverdrup wave propagation over the MBS are also likely candidates. This illustrates the need for a comprehensive tidal model study in the region that can resolve the complex bathymetry and the strongly stratified shallow pycnocline.

Chapter 3 Tables

Table 1. Linear regression results for Zi_{12} vs. HF radar at pt.A and pt.B for June 2010.

	R^2	*Slope*	*P-value*
		pt.A	
u-direction	0.25	0.50	5.25×10^{-46}
v-direction	0.29	0.54	7.92×10^{-53}
		pt.B	
u-direction	0.38	0.79	4.78×10^{-73}
v-direction	0.60	0.88	1.64×10^{-130}

Table 2. Linear regression results for Zi_{12} vs. HF radar at pt.A and pt.B for June 2010.

	R^2	*Slope*	*P-value*
		pt.A	
u-direction	0.12	0.37	6.84×10^{-22}
v-direction	0.15	0.41	5.42×10^{-27}
		pt.B	
u-direction	0.03	0.26	1.38×10^{-6}
v-direction	0.05	0.27	1.83×10^{-9}

Chapter 3 Figures

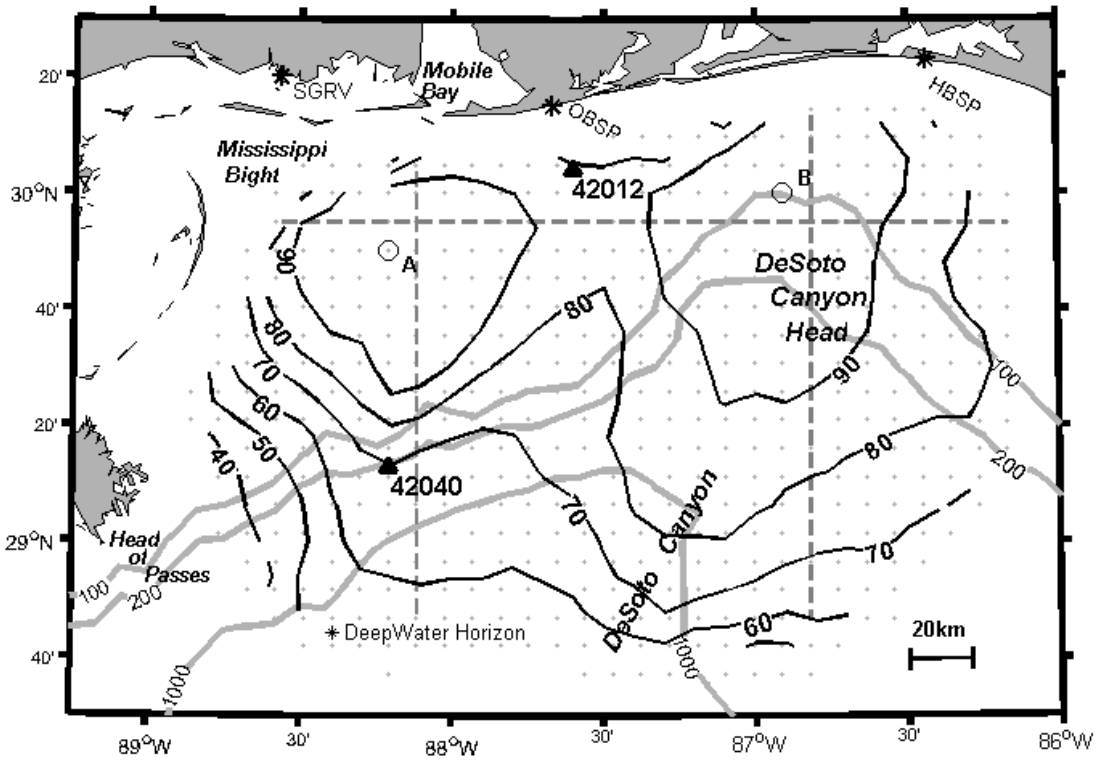

Figure 3.1. Northeastern Gulf of Mexico map with contours of HF radar percent coverage for June 2010. Thin grey lines represent the 100 m, 100 m, and 1000 m isobaths. Grey dots represent HF radar total vector 10 km grid data points for June 2010. Stars on coastline demark HF radar stations. Black triangles demark NDBC buoys 42012 and 42040. Grey west-east line and north-south dashed lines indicates transects for Hovmoller diagrams. Grey circles A and B indicate HF radar data points used in detailed timeseries analyses.

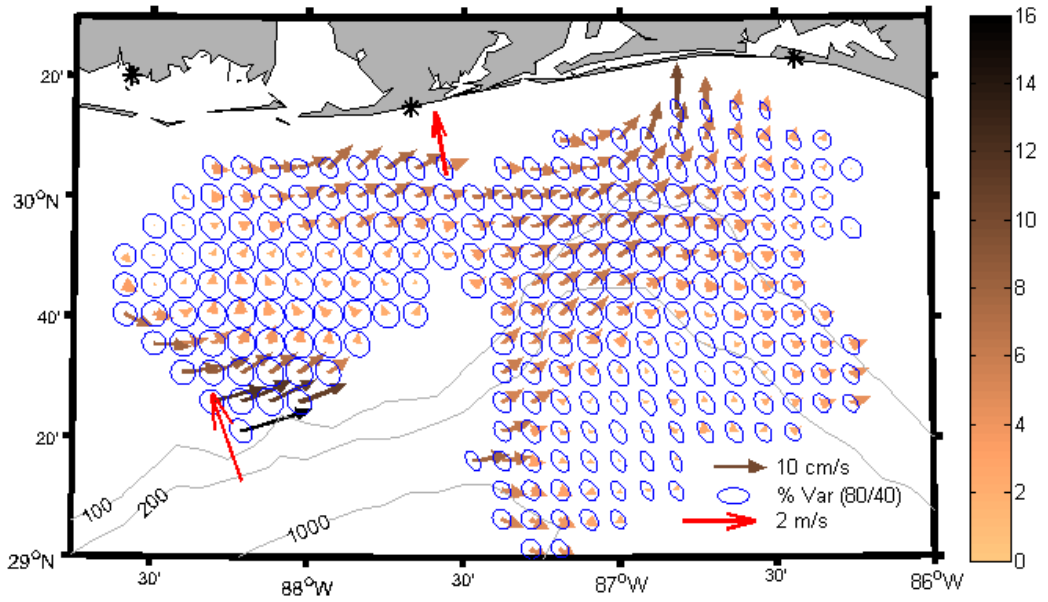

Figure 3.2. June 2010 HF radar measured mean flow (cm/s, size and color of arrows), mean wind speed at NDBC buoys 42012 and 42040 (m/s, red arrows), and percent of total variance in the diurnal band (0.89 – 1.11 cpd, blue ellipses). The ellipse in the legend indicates major (minor) axes of 80% (40%). Only coordinates with 80% HF radar temporal coverage are shown.

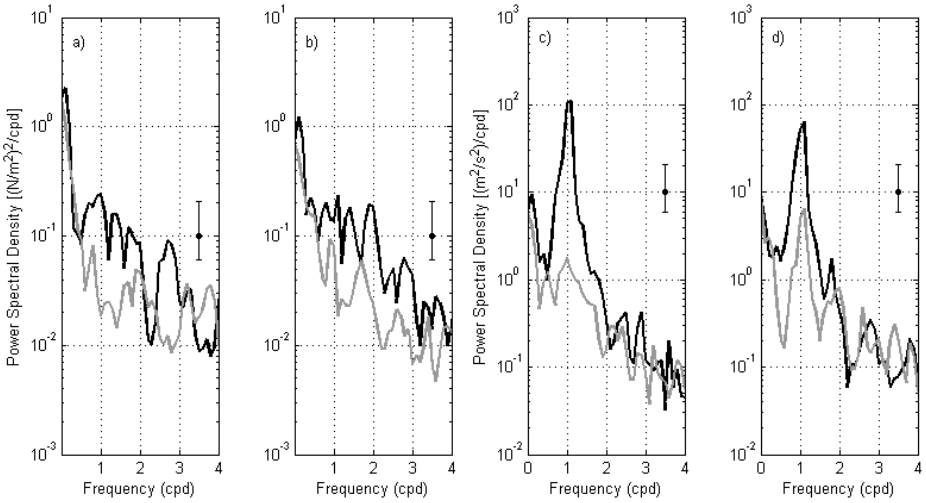

Figure 3.3. June 2010 Rotary spectra for wind-stress at buoys a) 42040 and b) 42012, and surface currents at c) pt.A and d) pt.B. Back (gray) lines identify CW (CCW) rotation. The 95% confidence interval is provided based on 15 degrees of freedom. Data were divided into three 240 hour windows. Frequency resolution is 0.096 cpd.

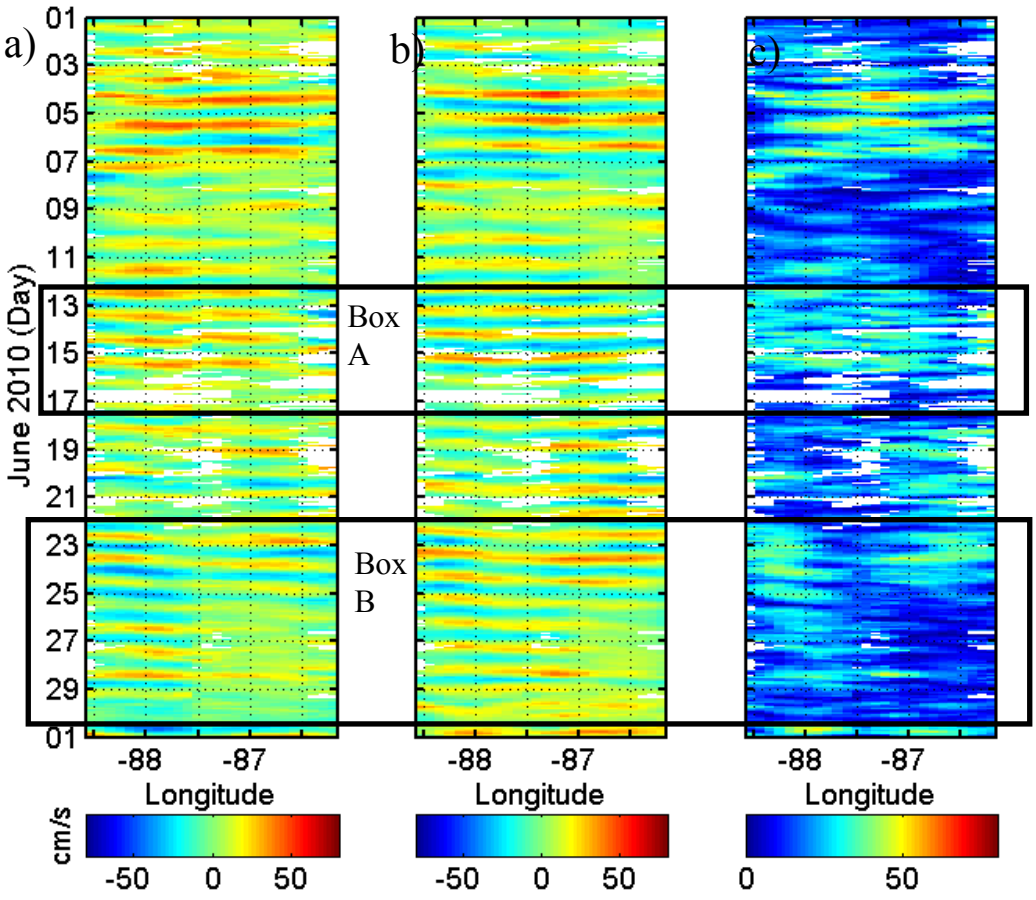

Figure 3.4. June 2010 surface current velocity along-shore transect (29.9°N) Hovmoller diagrams for a) ***u***-direction and b) ***v***-direction, and c) magnitude.

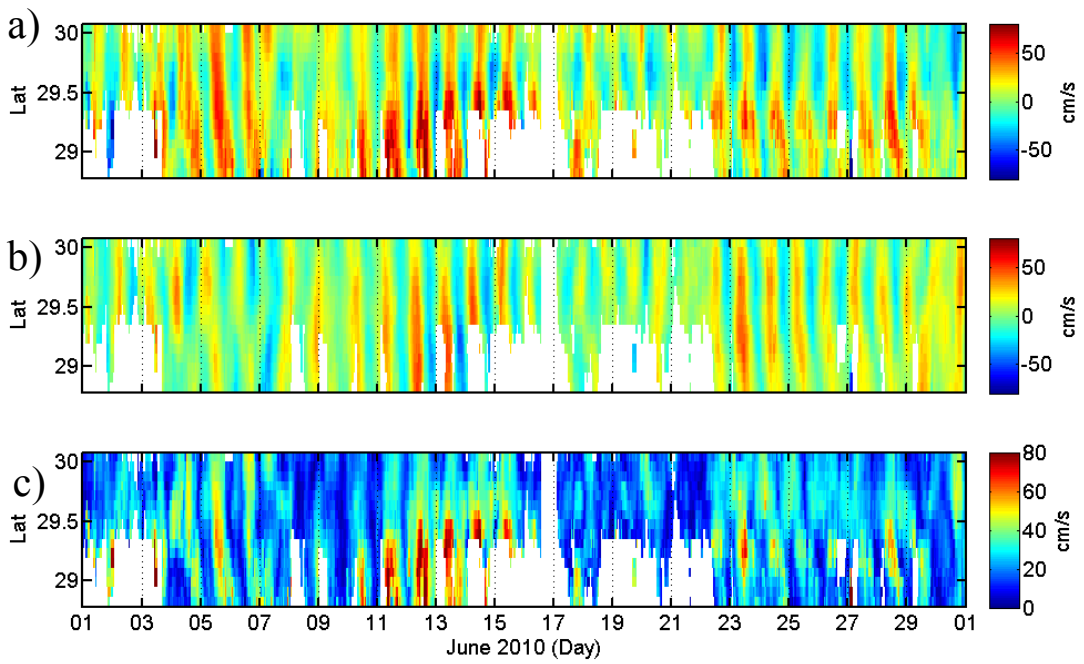

Figure 3.5. June 2010 surface current velocity MBS cross-shore transect (88.1°W) Hovmoller diagram for a) ***u***-direction and b) ***v***-direction, and c) magnitude.

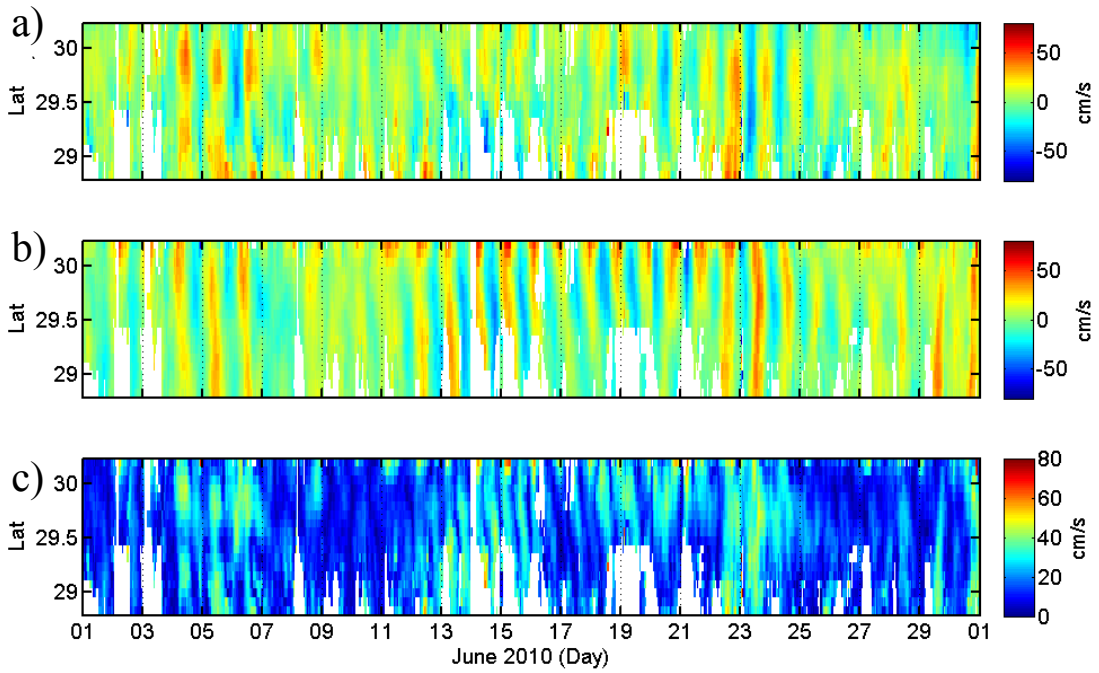

Figure 3.6. June 2010 surface current velocity DCH cross-shore transect (86.8°W) Hovmoller diagram for a) ***u***-direction and b) ***v***-direction, and c) is the surface current magnitude.

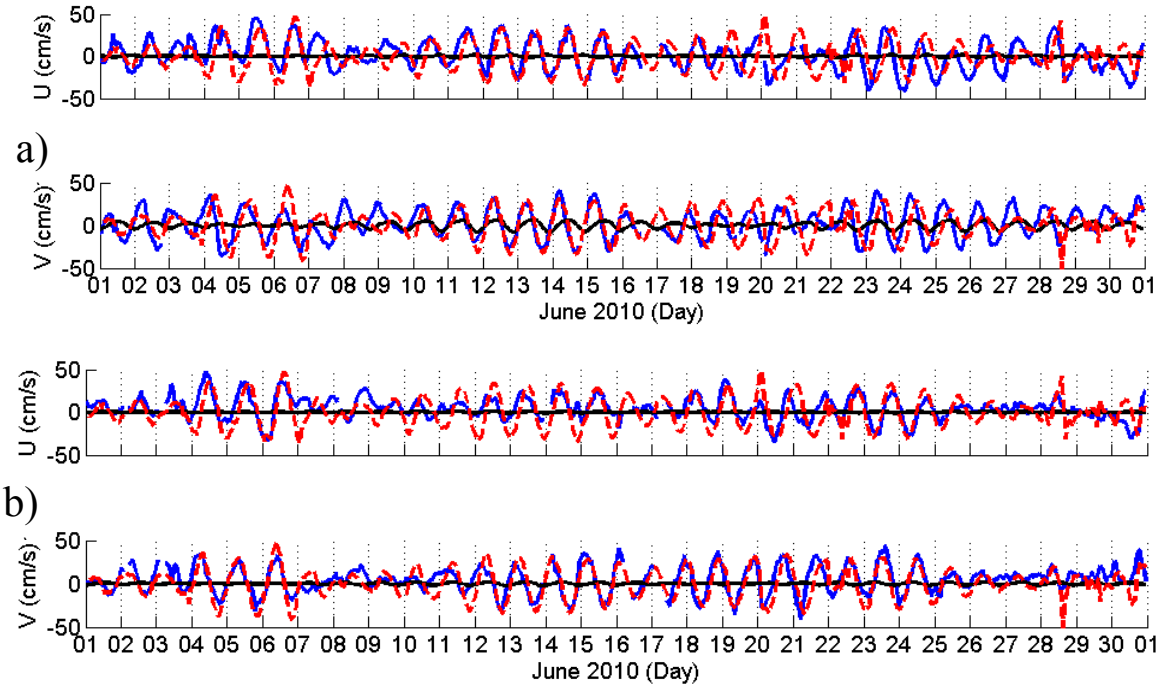

Figure 3.7. Pt. A (a) and B (b) June 2010 timeseries of Zi_{12} (red dashed lines), HF radar measured surface currents (blue lines), OTIS tidal prediction (black lines), for ***u*** (top) and ***v*** (bottom).

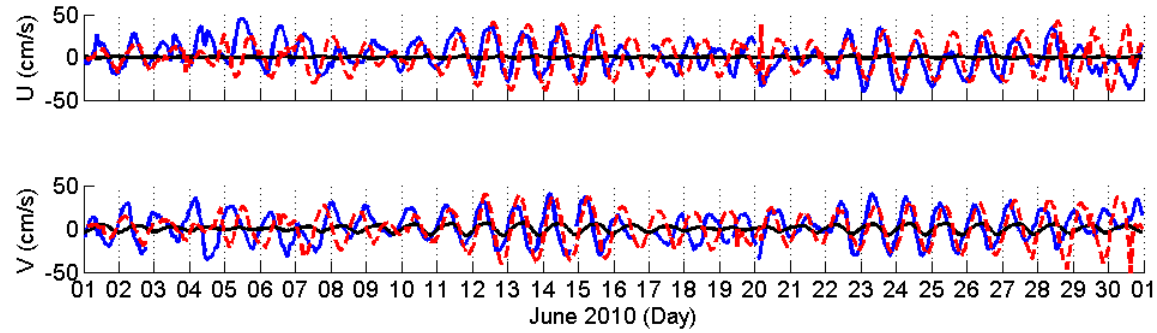

Figure 3.8. Pt. A June 2010 timeseries of Zi_{40} (red dashed lines), HF radar measured surface currents (blue lines), OTIS tidal prediction (black lines), for ***u*** (top) and ***v*** (bottom).

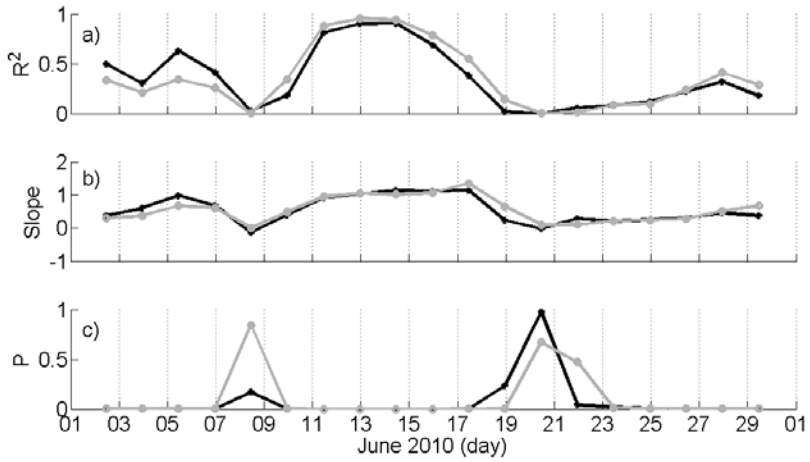

Figure 3.9. June 2010 running linear regression results comparing pt. A HF radar surface currents and Zi_{12}: a) normalized R^2, b) slope, and c) p-value. Black lines are for *u*-direction and gray lines are for *v*-direction. Overlapping three-day linear regressions were performed every 1.5 days. This figure corresponds with Figure 3.a.

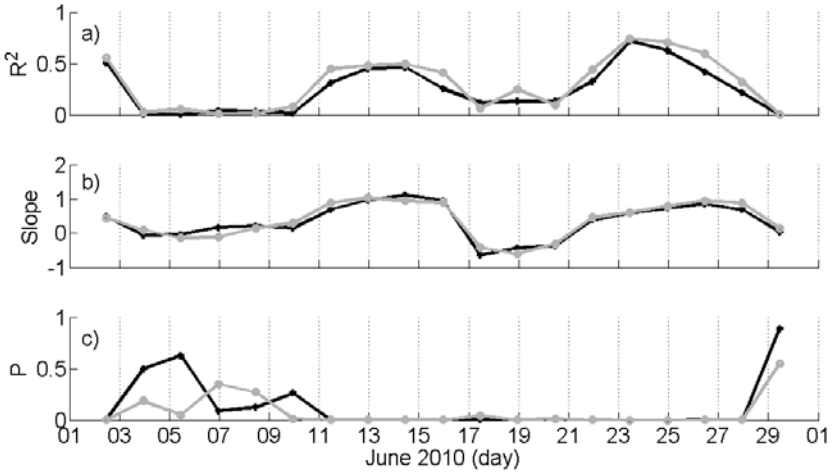

Figure 3.10. June 2010 running linear regression results comparing pt. A HF radar surface currents and Zi_{40}: a) normalized R^2, b) slope, and c) p-value. Black lines are for *u*-direction and gray lines are for *v*-direction. Overlapping three-day linear regressions were performed every 1.5 days. This figure corresponds with Figure 4.a.

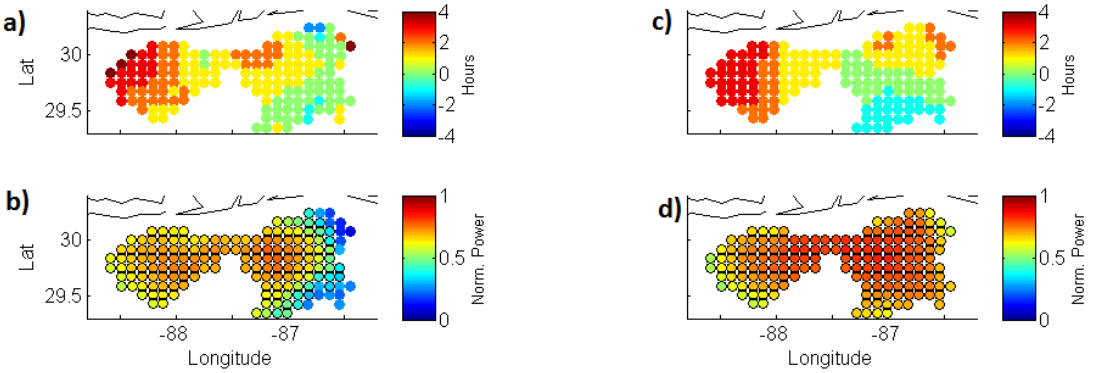

Figure 3.11. June 2010 cross-correlation between Zi_{12} and HF radar surface currents. Time lag in a) ***u***-direction and c) ***v***-direction. Normalized correlation in b) ***u***-direction and d) ***v***-direction. Black circles indicate data points above the 10% level of significance which is 0.3 based on 31 degrees of freedom.

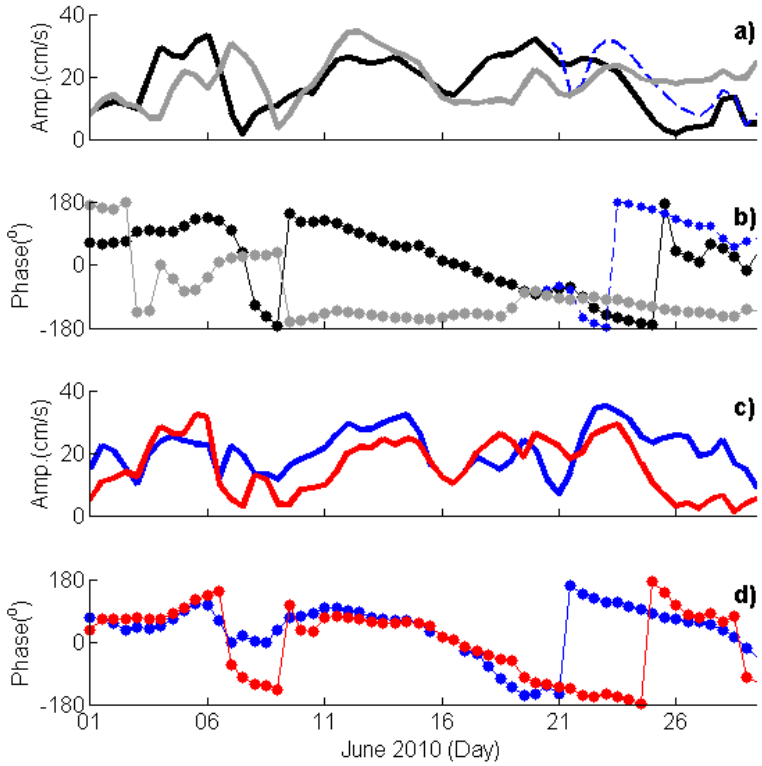

Figure 3.12. June 2010 Zi_{12} (black) and Zi_{40} (grey) CW diurnal Complex Demodulation a) amplitude and b) phase. HF radar Complex Demodulation c) amplitude and d) phase at locations A (blue lines), B (red lines). The blue lines in (a) and (b) are for the Zi_{12} calculation restarted on 20 June.

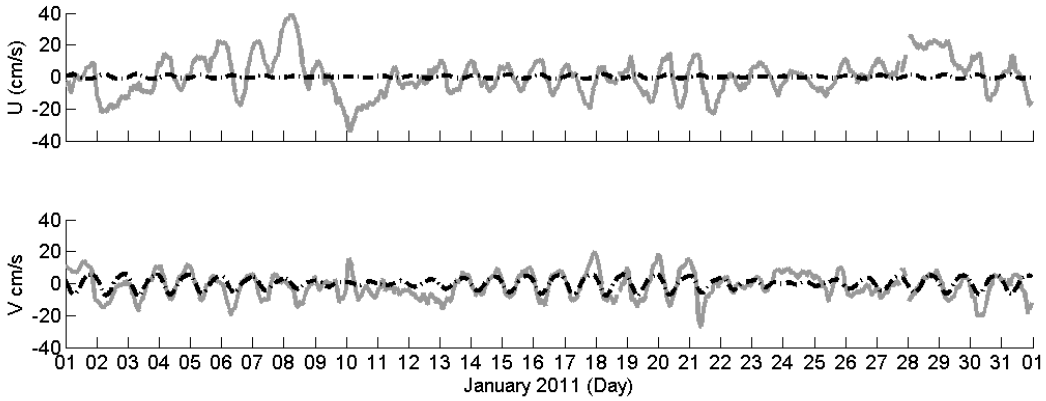

Figure 3.13. January 2011 ***u*** (top) and ***v*** (bottom) HF radar measured surface currents time-series at pt.A (gray lines) and OTIS tidal prediction (black dashed lines).

Chapter 4

The Influence of Vorticity on the Effective Frequency of Near-Diurnal Inertial Oscillations in the Northeastern Gulf of Mexico

Background

Inertial motions (also referred to as inertial oscillations or inertial waves) are typically attributed to the wind-forced oscillatory response of the homogeneous ocean on the rotating Earth [*Ekman*, 1905]. The frequency of the response, the local inertial frequency $f = 2\Omega sin\varphi$, is dependent on the latitude φ and Earth's angular rotation Ω. They are enhanced at the critical latitudes for inertial motions, φ = 30°N(S), where diurnal winds can resonate with the inertial motions that are diurnal at these latitudes [*Simpson et al.*, 2002]. Inertial motions are believed to contribute to mixing in the ocean through the generation of internal waves [*Kunze*, 1985; *Millot and Crépon*, 1981], divergence from their spatiotemporal variability [*Hyder et al.*, 2011], shear at the bottom of the mixed layer [*Zhang et al.*, 2009], and interaction with internal tides [*Davies and Xing*, 2003]. Mixing due to inertial motions can therefore occur locally due to divergence and shear, and remotely through the generation of internal waves.

The frequencies of near-inertial oscillations (NIOs) are primarily influenced by sub-inertial flow, which induces a Doppler shift in the oscillations (when observed in an Eulerian frame of reference), the buoyancy frequency, and sub-inertial relative vorticity [*Kunze*, 1985; *Mooers*, 1975; *Perkins*, 1972; *White*, 1972; *Young and Jelloul*, 1997]. Sub-inertial relative vorticity ζ shifts the "effective" inertial frequency f_{eff} from the local inertial frequency f according to the relation

$$f_{eff} = f + \zeta/2 \quad (1)$$

[*Kunze*, 1985; *Mooers*, 1975]. The f_{eff} determines the lower (upper) frequency limit above (below) which internal inertial waves are free to propagate (trapped). *Kunze* [1985] also determined that NIOs are trapped in regions of negative vorticity associated with barotropic flow, and are trapped and amplified in negative vorticity associated with baroclinic flow where they propagate downward. The derivation of (1), along with the dispersion relationship for NIOs generated in shear associated with baroclinic and barotropic jets, was performed by applying a ray path approach that incorporates the WKB approximation. In this application, the WKB approximation is valid when the NIO scales (λ) are smaller than the vorticity scales (L) and become less so as λ increases. However, *Kunze* [1985] found that, even when $\lambda \approx L$, errors were small when applying the WKB approximation which was corroborated with observations [*Kunze and Sanford*, 1984]. *Young and Jelloul* [1997] applied a "method of multiple scales" to derive a more general equation for NIOs that is valid for all scales of λ and L. For the case when NIO scales are greater than the spatial scales of the vorticity field ($\lambda < L$), NIOs will simultaneously be subjected to negative and positive vorticity which will cancel out their respective influence. The horizontal dispersion behavior of NIOs when $\lambda < L$ is often referred to as the "trapping" regime whereas when $\lambda > L$ it is referred to as the "strong dispersion" regime [*Young and Jelloul*, 1997]. Although there have been numerous modeling and observational studies on the influence of vorticity on f_{eff} that successfully verified (1) [*Kunze and Sanford*, 1984; *Poulain et al.*, 1992; *Rainville and Pinkel*, 2004], a notable exception was the failure by *D'Asaro* [1995] to verify the expected f_{eff} with the vorticity field interpolated from drifter data. The failure was speculated to be attributed to a failure of resolving the spatial scales of vorticity, and/or nonlinear wave-wave

interactions. *Young and Jelloul* [1997] added that the scales of the NIOs observed by *D'Asaro* [1995] were likely much larger than the scales of the mesoscale eddies and therefore (1) was not completely valid.

The northeastern Gulf of Mexico (NeGoM) (Fig. 1) has been identified as a region that exhibits spatiotemporal variability of large ubiquitous near-surface near-diurnal inertial oscillations (NDIOs) [*Gough et al.*, 2016; *Jarosz et al.*, 2007]. The magnitude and ubiquity of the NDIOs are attributed to diurnal wind-forced resonance at *f*, which is diurnal at 30°N, along with the presence of a shallow mixed layer that is easily forced by the wind. The NDIOs are therefore more prevalent during the summer when strong shallow stratification is present due to widespread semi-freshwater discharge and strong surface solar heating. *Gough et al.* [2016] observed abrupt phase changes and amplification of NDIOs over the outer Mississippi Bight Shelf (MBS) and speculated that the properties of the NDIOs could be influenced by shear in the flow. *Zhang et al.* [2010] also observed enhanced NDIO variability coupled with vorticity in this region. *Gough et al.* [2016] speculated that the NDIO spatiotemporal variability in the NeGoM could enhance mixing at the interface between regions of asynchronous oscillations where vertical motions are generated by local divergence. By comparing the inertial response to wind-forcing between NDBC buoys 42040 and 42012, it was suggested that spatiotemporal variability of the winds contributed to frequency and phase shifts of the NDIOs [*Gough et al.*, 2016]. This was particularly true at the end of June 2010 when the inertial response to wind-forcing determined from buoy 42040 (42012) matched the oscillations over the MBS (DeSoto Canyon Head (DCH) region). The frequencies of the oscillations were found to be blue-shifted, which is consistent with observations of NIOs

between 30°N and the equator [*Elipot et al.*, 2010; *Poulain et al.*, 1992].

Here we continue with the June 2010 HF radar surface current velocity data used by *Gough et al.* [2016] and focus on the NDIOs over the outer MBS and DC on 22-29 June when there was a distinctive vorticity field (Fig. 2) associated with the NDIO frequency and phase fields (Figs. 3 and 4). From the HF radar data, a unique simultaneous spatiotemporal perspective of the NDIOs and near-surface vorticity is provided. The relationship between the vorticity and the NDIOs is verified by comparing the predicted f_{eff} field due to vorticity from (1) with observed spatiotemporal changes in the observed NDIO frequency field. The observed frequencies are determined by performing complex demodulation analyses on HF radar surface current velocities. Additionally, oscillatory near-surface divergence due to spatial NDIO phase differences over the outer MBS and DeSoto Canyon (DC) regions are determined. The time of this study was during the Deepwater Horizon oil spill and the region of interest over the DC and outer MBS is approximately 50 km to the northeast from the Deepwater Horizon platform. During this time, oil from the spill was observed to flow northeastward along the outer MBS, through the region of interest, and eventually shoreward at the DeSoto Canyon Head (DCH) [*Dietrich et al.*, 2012]. It is speculated that the oil was subjected to vertical mixing generated by the oscillatory divergence over the outer MBS and DC.

HF Radar Data

The application of HF radar for measuring 2-D near-surface ocean current velocities are well documented [*D Barrick*, 1971; 1972; *D Barrick and Lipa*, 1979a; *Stewart and Joy*, 1974]. HF radars measure the near-surface current velocities both towards and away from each radar. These velocities, which are distributed on a circular

grid radiating from each radar, are typically referred to as “radial vectors”. The radial vectors from multiple radars can be “combined” to generate “total vectors” which are the ***u*** (east-west) and ***v*** (north-south) component of the measured near-surface current velocities distributed on a 2-D Cartesian grid. All processing of the HF radar data were performed with CODAR software (www.codar.com).

Hourly 2-D HF radar total vectors on a 9 km grid over the NeGoM were obtained by three radars from 22 to 29 June 2010 during the Deepwater Horizon oil spill. The three radars are labeled HBSB, SCRV, and OBSP in figure 4.1. The radars are maintained by the University of Southern Mississippi as part of the Central Gulf of Mexico Observing System (CenGOOS). They are CODAR-type long-range (approximately 5 MHz) HF radars that have a range of approximately 120 km, measure the top 2.5 m of the water column, and cover the coastal region over the MBS, DC, and DeSoto Canyon Head (DCH). The coverage almost reaches the site of the Deepwater Horizon oil spill.

Diurnal Complex Demodulation of HF Radar Surface Current Velocities

The method of complex demodulation is useful for determining frequency and phase shifts of inertial oscillations [*Gough et al.*, 2016; *Jarosz et al.*, 2007; *Perkins*, 1976; *Simpson et al.*, 2002], and is described in detail in *Emery and Thomson* [2001]. In summary, complex demodulation utilizes a least squares fit between the timeseries of an observed signal described by a vector in complex form (e.g. $V(t) = u(t) + iv(t)$) and a fabricated oscillatory timeseries generated by a fixed amplitude vector in complex form rotating CW and CCW at frequency ω described by $V_f(t) = A\, exp(\pm i\omega t)$ where A is the amplitude. The results of complex demodulation analysis return an amplitude and a phase

for both CW and CCW rotation. The amplitude is used to determine when the phase results are significant, and the phase is the phase difference between $V(t)$ and $V_f(t)$. If complex demodulation is performed on subsequent sections of $V(t)$, the frequency of the observed timeseries in relation to ω can be determined by the temporal slope of the phase results. A negative (positive) temporal phase slope implies that the observed oscillatory frequency is greater (less) than the fixed frequency ω.

"Diurnal" complex demodulation analyses were performed on overlapping 24 hour sections of the HF radar hourly complex velocities every 12 hours at each coordinate. The least squares fits were performed with a 24 hour complex time series of a fixed amplitude vector rotating diurnally ($\omega = 24^{-1}\text{hr}^{-1}$). This generated spatial maps of the phase relative to the fixed diurnal signal every 12 hours (not shown). A spatial map of the mean NDIO frequencies relative to the diurnal frequency was generated by averaging the temporal phase slopes over the entire time period at each coordinate (Fig. 3). Additionally, a map of the temporally averaged phase relative to the phase of a chosen coordinate (87.9°W, 29.4°N) was produced (Fig. 4). In the complex demodulation averaging analyses only phase values associated with amplitude results greater than 0.1 m/s were used. Since the NDIOs rotate CW, only the CW results are significant and therefore only the CW results are displayed.

Chlorophyll and Turbidity Satellite Imagery

1 km resolution (at nadir) level 2 Moderate Resolution Imaging Spectroradiometer (MODIS) chlorophyll concentration and turbidity satellite imagery from the Aqua satellite were obtained from the NASA Ocean Color data portal (http://oceancolor.gsfc.nasa.gov/cms/). High chlorophyll concentrations and high

turbidity are presumed to be associated with semi-freshwater discharge. Only one viable chlorophyll image (24 June 2010 at 19:20 UTC, Fig. 4.5) was available for the end of June 2010 due to widespread cloud coverage. Since the turbidity image mirrored the chlorophyll image only the chlorophyll image is used. Assuming regions of high chlorophyll (and turbidity) are associated with semi-freshwater discharge waters, the maps of chlorophyll can be used to determine the spatial extent of river outflow in the GoM. This can, in turn, be used to make implications on spatial stratification variability while also identifying fronts of scales larger than 1 km.

Overview of Observed Circulation, Vorticity, and Near-Inertial Oscillations

The mean flow for 22-29 June was typical for summer circulation in the northeastern Gulf of Mexico based on previous observational and modeling efforts [*He and Weisberg*, 2002b; *Smith and Jacobs*, 2005; *Wang et al.*, 2003; *Weisberg et al.*, 2005; *Yuan*, 2002]. Northeastward jet-like flow approximately 40 km wide associated with the large scale loop current system followed along the 100 m isobath that separates the MBS and DC (Fig. 2). As the jet-like flow entered the DCH it gradually dissipated and veered shoreward. The jet-like flow along the 100 m isobath between the MBS and DC generated a distinctive vorticity pattern with positive (negative) vorticity to the north (south) of the jet averaging 5 to 7 $\times 10^{-6}$ s^{-1} (-4 to -5 $\times 10^{-6}$ s^{-1}).

During this time, *Gough et al.* [2016] observed spatiotemporal variability in both phase and amplitude of the NDIOs over the NeGoM. The NDIOs over the MBS were out of phase with those over the DCH and found to be related to the inertial response to wind-forcing at buoy 42040 while those over the DCH were found to be related to the inertial response to wind-forcing at buoy 42012. An abrupt north-south phase change was

observed at the southern edge of the MBS which is the region of interest in this paper. Augmenting the observations by *Gough et al.* [2016], diurnal band-passed HF radar surface currents indicate, from west to east, a large region of NDIO amplitudes averaging 0.25-0.30 m/s over the MBS, a region of small amplitudes between the MBS and DCH averaging 0.10-0.15 m/s centered at 87.4°W, 29.5°N, and amplitudes over much of the DCH averaging 0.20-0.25 m/s (Fig. 6). Variability in the NDIO amplitudes from north to south over the MBS indicate there is a decrease in the oscillation amplitudes at the southern edge of the MBS and an increase over the DC at the very southern extent of the domain. Hövmöller diagrams of diurnal band-passed currents were generated for the 88.1°W longitudinal transect to capture the spatiotemporal variability of the NDIOs (Fig.7) not captured by the averaging. Figure 7 clearly shows the diurnal oscillations and figure 7(bottom) shows that the amplitudes of the NDIOs decrease abruptly south of 29°N on 23 June and that this abrupt decrease migrates northward to about 29.4°N by 27 June. Likewise, an abrupt increase in amplitudes over the southern extent of the coverage also migrated northward from just south of 28.75°N to 29°N for the same time period. The band of abrupt relatively weak (~20 cm/s) NDIOs between 29°N and 29.4°N corresponds with a band of strong frequency gradients (Fig. 8) and a band of negative vorticity (Fig. 9) within the same latitude zone.

Frequency and Phase Shifts of NDIOs along the Outer Mississippi Bight Shelf and DeSoto Canyon

Since f_{eff} becomes the intrinsic frequency of NIOs in the ocean, the background sub-inertial vorticity field along with f should be able to predict the NIO frequency field according to (1) when the WKB approximation is valid. The HF radar surface current

velocities provide a means to simultaneously calculate both the background vorticity field and the frequency field of the NIOs. Once the HF radar-derived vorticity field is determined, it can then be inserted into (1) to predict the expected f_{eff} field of NIOs. The observed NIO frequency field can be determined from complex demodulation analyses on HF radar surface current velocities. The 2-D f_{eff} field can then be compared to the observed 2-D NIO frequency field. Subsequently, the NIO frequency field can be compared to the NIO phase field (also a result of complex demodulation analyses) to make inferences about the influence of the observed frequency field on the phase field.

The NDIO frequency and phase fields (Figs. 3 and 4) exhibit a compelling spatial relationship with the vorticity field (Fig. 2) over the outer MBS and DC. The positive vorticity region over the outer MBS matches the regions of positive frequency shifts and negative phase shifts. The negative vorticity region over the DC generally matches the regions of negative frequency and phase shifts. In order to quantify the influence of vorticity on the NDIOs, the relative difference in vorticity between the identified regions of positive and negative vorticity are compared to the relative difference in frequency and phase shifts of the NDIOs. The relative difference is examined because this negates the influence of the general blue-shift in NDIOs that are typically observed in the NeGoM. Additionally, since the distance between the two regions of vorticity is approximately 20-40 km, the local inertial frequency difference due to latitude difference is expected to be small compared to the frequency difference due to the effects of vorticity. The predicted f_{eff} field therefore does not account for latitude difference.

Over the outer MBS the mean frequency shift from the diurnal frequency f_d ranged between 3 and 5 x 10^{-6} s^{-1} (Fig. 3). The corresponding positive vorticity region

over the outer MBS ranged between 4 and 7 x 10^{-6} s^{-1} (Fig. 2) which translates to a predicted shift in f_{eff} from f of 2 to 3.5 x 10^{-6} s^{-1}. Over the DC the mean frequency shift from f_d ranged between +1.5 and -1.5 x 10^{-6} s^{-1} and the corresponding region of strong negative vorticity ranged between -3 and -6 x 10^{-6} s^{-1} (or an f_{eff} shift from f of -1.5 to -3 x 10^{-6} s^{-1}). The predicted difference in f_{eff} between the positive and negative vorticity regions is therefore in the range of 3.5 to 6.5 x 10^{-6} s^{-1}, which agrees with the observed frequency difference between the two regions which ranged between 1.5 and 6.5 x 10^{-6} s^{-1}. Because (1) was able to successfully predict the observed frequencies of the NDIOs, it is implied that the NDIOs are exposed to a "trapping" regime where $\lambda < L$.

As would be expected, the NDIO phase field (Fig. 4) is related to the frequency field (Fig. 3) although with the available information it is not possible to verify the phase shifts are due solely to the frequency of the NDIOs. The NDIOs over the MBS lead those over the DC by as much as 90° which is surprisingly large. There are many mechanisms in addition to the influence of vorticity on f_{eff} that could influence the phase shift field: this includes spatial wind-forcing and stratification variability, internal waves and tides, and the influence of vorticity at scales that cannot be resolved by the 9 km resolution HF radar data. This last influence could be the result of small scale vorticity generated by thermal wind balance along density fronts. The 24 June MODIS chlorophyll concentrations exhibited a front that extended northeastward from the southeast corner of the domain (88.5°W, 28.7°N) and through the region of interest between the MBS and DC (Fig. 5). The high chlorophyll and turbidity observed on the northwest side of the front was likely associated with semi-fresh low-density discharge water. The magnitude and spatial scales of the vorticity associated with the front in thermal wind balance can be

estimated with estimates of the buoyancy frequency and depth of the mixed layer. The buoyancy frequency (N) and depth of the surface mixed layer (*H*) associated with the discharge water have been reported to be approximately 0.065 s^{-1} and 8 m [*Dzwonkowski and Park*, 2012; *Gough et al.*, 2016]. The Rossby radius of deformation, $R_d = NH/\pi f$, associated with the layer of discharge water would therefore be approximately 2.3 km and the vorticity field generated along the front in thermal wind balance would be at scales too small to be resolved by the HF radar data. The vorticity associated with the thermal wind can be estimated by first solving for the change in velocity across the front within the R_d using the thermal wind equation, $\partial u/\partial z = N^2 \partial z/f \partial y$ where f = 7.27 x 10^{-5}, $\partial z = H$ = 8 m, and $\partial y = 2.3$ km. The change in velocity across the front is $\partial u/\partial y$ which is the shear vorticity, is estimated to be 8.7 x 10^{-5} s^{-1}. This vorticity is relatively strong and could have an impact on the frequency and phase of inertial waves generated in, and/or passing through, the region as long stipulations for a "trapping" regime are met. Although the HF radar data are unable to spatially resolve the vorticity and frequency shift of currents along the front, it is possible for the HF radar data to capture the relative phase shift between both sides of the front since away from the front the frequency of the NDIOs will return to f_{eff}. This could explain the abrupt phase shift that occurs at about 29.2° N in figure 8. Considering that the vorticity within the front was predicted to be relatively large, the phase shift on either side of the front should also be large. However, the general shape of the frequency and phase fields (Figs. 3 and 4) along with the vorticity field (Fig. 2) suggests that the frequency shift associated with the large scale vorticity field is largely contributing to the phase field.

Oscillatory Divergence between the Mississippi Bight Shelf and the DeSoto Canyon

The abrupt phase difference of the NDIOs between the MBS and DC identifies where the two regions of asynchronous oscillations meet (Figs. 4 and 8). Oscillatory divergence patterns determined from bandpassed HF radar surface current velocities show that this region is a hot spot for strong oscillatory divergence (Fig. 10). Because the NDIOs are presumed to be confined to the mixed layer, the divergence they generate should also be confined to the mixed layer. Through continuity, the fluctuating divergence within the mixed layer will generate fluctuating vertical displacement of the pycnocline. The mean amplitudes of the divergence oscillations determined from diurnal bandpassed surface currents indicate that there is enhanced divergence between the MBS and DC where mean amplitudes reached 1 x 10^{-5} s^{-1}. A simple calculation of the vertical velocity of the pycnocline by applying continuity to an 8 m mixed layer depth experiencing divergence of 1 x 10^{-5} s^{-1} over a 5,000 by 5,000 m region produces a vertical velocity of 0.02 m/s (note that the HF radar data have been interpolated onto a 5 km Cartesian grid). Assuming the vertical velocity oscillations are sinusoidal, the vertical displacement of the pycnocline over 12 hours would be 3.24 m (and 6.48 m over 24 hours from the minimum to the maximum). Although these calculations are rudimentary, they provide insight into how the pycnocline may potentially be displaced by the inertial oscillations. Diurnal vertical displacement of the pycnocline of these magnitudes would likely generate internal waves, as speculated by *Hyder et al.* [2011], in the stratified environment of the NeGoM. Investigation of the hourly evolving divergence field of the band-passed surface currents (not shown) indicate that regions of strong divergence often migrate. If the divergence patterns were to migrate at a speed comparable to the speed of

internal waves, the internal wave amplitudes could potentially become further enhanced.

Summary and Discussion

The near surface NDIO frequency field (Fig. 3) has been shown to be related to the vorticity field (Fig. 2) over the outer MBS and DC for the time period 22-29 June 2010. The relationship was found to be consistent with (1) where the effective inertial frequency f_{eff}, which becomes the lower bound that internal inertial waves are free to propagate, is shifted by half of the background sub-inertial vorticity. The verification of (1) implies that the NDIOs in this region are within a "trapping" regime where NDIO scales are smaller than (and possibly similar to) the scales of the vorticity field. The spatial pattern of the frequency field in the region (Fig. 3) also matched the spatial pattern of the phase field (Fig. 4), suggesting that the frequency shift associated with the large scale vorticity is largely responsible for the phase shift in this region. Enhanced oscillatory divergence over the region between the MBS and DC (Fig. 10) was attributed to asynchronous inertial oscillations identified by an abrupt spatial phase shift. It was speculated that the vertical displacement of the pycnocline generated by the oscillatory divergence could directly enhance mixing in the region and also enhance mixing due to the generation of internal waves. At the time the HF radar observations were made (22-29 June 2010), oil from the Deepwater Horizon spill was advected by northeastward flow through the region of abrupt NDIO phase shifts between the MBS and DC (Figs. 4 and 8) before veering onshore at the DCH. It is therefore likely that oil from the spill was exposed to mixing generated by oscillatory divergence at the interface between the asynchronous NDIOs over the region. This would be particularly true for oil suspended in the surface mixed layer or entrained at the pycnocline. The observed mean surface flow is

typical for the NeGoM. The observations and implications of this study are therefore likely not the result of an isolated event.

Although the relationships between the large scale vorticity, frequency, and phase fields are compelling, the seemingly co-situated region of abrupt relatively small amplitudes, negative vorticity, and phase shifts between 28.8 and 29.4°N (Figs. 7, 9 and 8) are worth further discussion. The decrease in NDIO amplitudes within the band of negative vorticity is contrary to the expected amplification of NIOs in negative vorticity. It may be possible, that the decrease in amplitudes in the negative vorticity band is due to the downward propagation of internal waves. Another possibility is the trapping of NIO energy associated with coastal stratification [*Gough et al.*, 2016; *Xing and Davies*, 2004]. The abrupt decrease occurs where there was a front in the chlorophyll satellite imagery (Fig. 5) where it is presumed to be strongly stratified to the north of the front. The front intersects 88.1°W at 29.2°N on 24 June which corresponds to the abrupt change in NDIO amplitudes (Fig. 7) and phase gradients (Fig. 8). The enhanced amplitudes to the north of the front is consistent with the strong stratification and also consistent with northwest to southeast propagation of NDIOs the lowering of f_{eff} by negative thermal wind vorticity hindering northwest to southeast propagating NDIOs. The NDIO scales would need to be relatively small ($< R_d \approx 2.3$ km) in order for the NDIOs to exhibit "trapping" regime behavior. With the information available it is not possible to investigate this further.

With the exception of the region of interest between the outer MBS and DC, there was not complete agreement between the frequency shift (Fig. 3) and the vorticity (Fig. 2) fields throughout the domain. The decrease in positive vorticity over the inner MBS did not correspond with an expected frequency shift in the observed NDIOs.

Additionally, the shape of the negative vorticity field over the DC did not exactly match the shape of the frequency shift field. *D'Asaro* [1995] pointed out a number of issues that could lead to a failure of observed inertial frequencies to agree with the background vorticity's influence on the effective inertial frequency: Relatively weak vorticity may not effectively influence f_{eff}, the vorticity field may not be completely represented if it occurs at scales smaller than the observational resolution or if smoothing is applied, and there could be non-linear wave-wave interaction between internal waves and inertial oscillations. The influence on the NDIO frequency by Doppler shift and buoyancy frequency was not extensively investigated which could account for disagreement between f_{eff} and observed NDIO frequencies. Additionally, (1) is dependent on the WKB approximation which stipulates that the internal inertial wavelengths be smaller than the spatial scale of the vorticity field. It is also possible WKB stipulations were not always met and that the NDIOs were within a "dispersive" regime.

Future observational work in this region on NDIO variability should include instrumentation that is capable of resolving multiple scales of the NDIO and vorticity fields in three dimensions. This is not an easy task which is evident by the prevalence of theoretical and modeling studies in comparison to observational studies. We have shown that HF radar is a useful tool for observing the 2-D spatiotemporal variability of NIOs. The limitations of HF radar data, particularly in resolving small scale and vertical structures, could be mitigated by simultaneously incorporating in-situ ADCP, CTD, and drifter observations.

Chapter 4 Figures

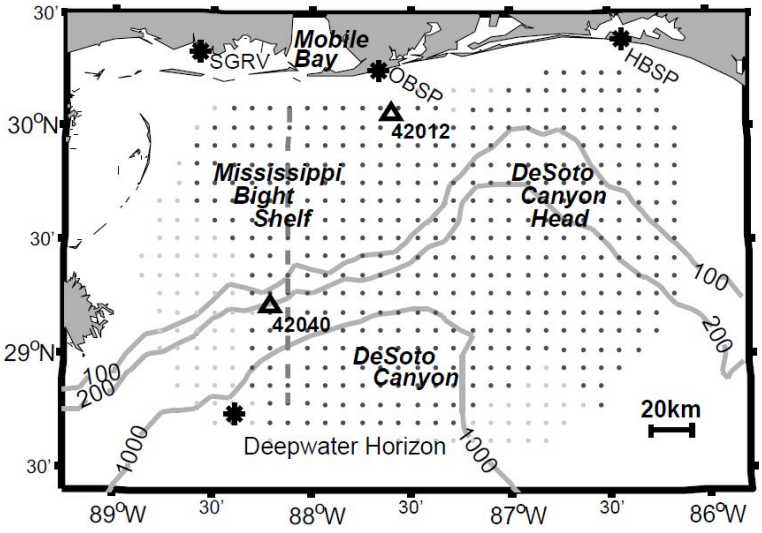

Figure 4.1. Northeastern Gulf of Mexico map with 100, 200, and 1000 m isobaths. HF radar 9 km grid points with above (below) 80% temporal coverage are indicated by dark (light) grey dots. Stars on coastline represent the HF radar locations. NDBC buoy 42040 and 42012 are labeled. The north-south dashed line indicates the Hovmoller diagram transect along 88.1°W. The Deepwater Horizon platform is identified by a black star.

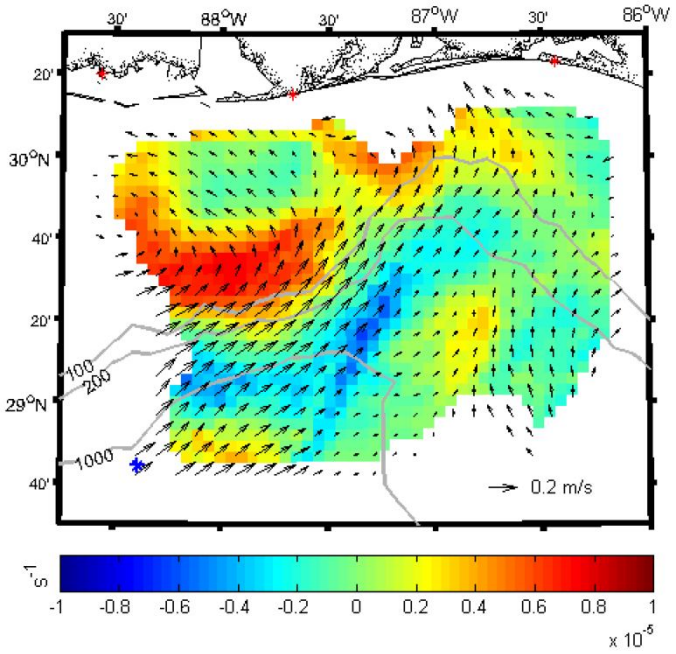

Figure 4.2. Mean flow (black vectors) and vorticity (color contours) from HF radar near-surface current velocities, 22-29 June, 2010.

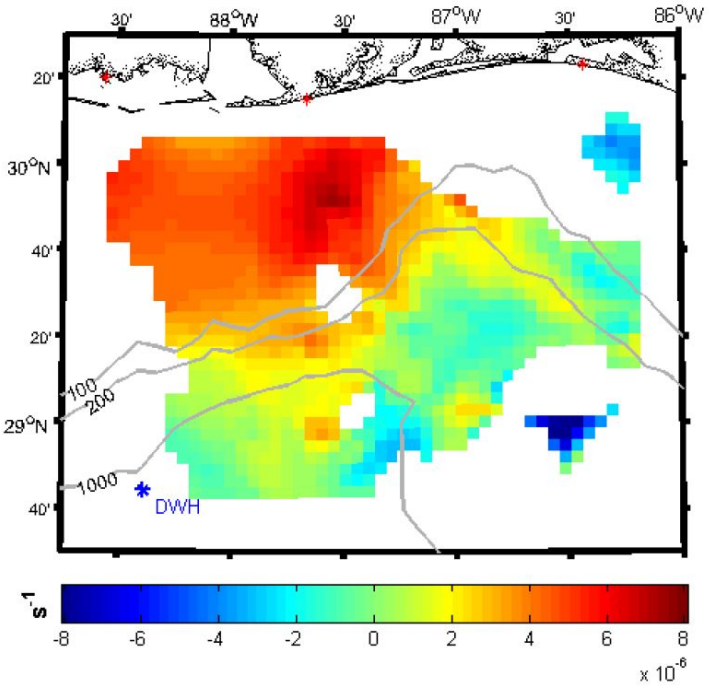

Figure 4.3. Map of mean NDIO frequency shift relative to the diurnal frequency from CW diurnal complex demodulation analyses.

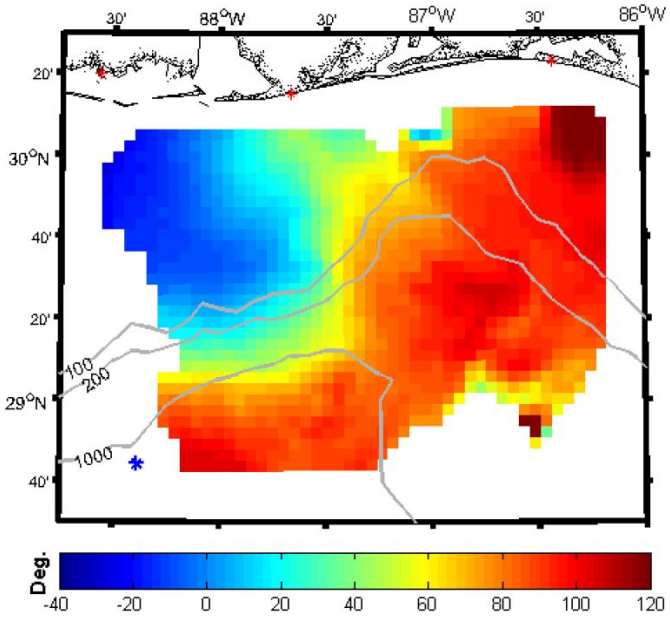

Figure 4.4. Map of mean NDIO phase relative to the phase at coordinate at 87.9°W, 29.4°N. Determined from CW diurnal complex demodulation analyses.

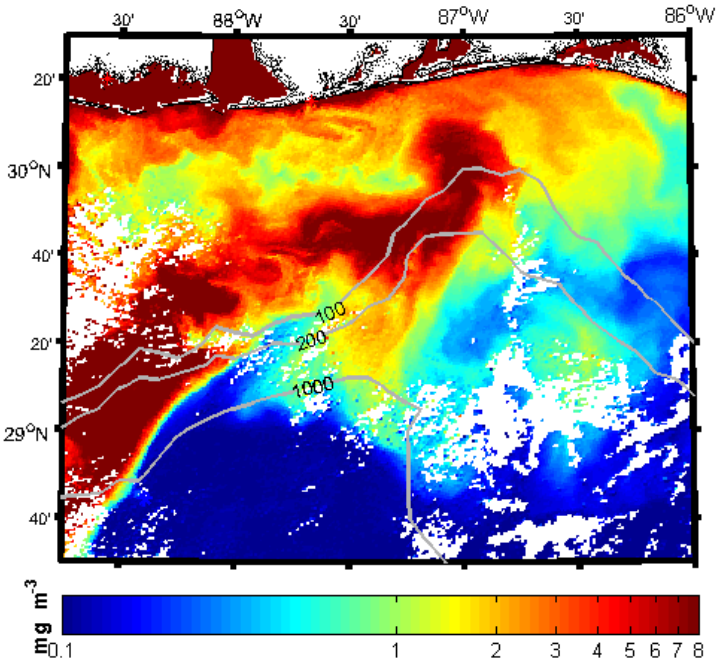

Figure 4.5. MODIS chlorophyll concentration satellite image for 24 June 2010 19:20 UTC.

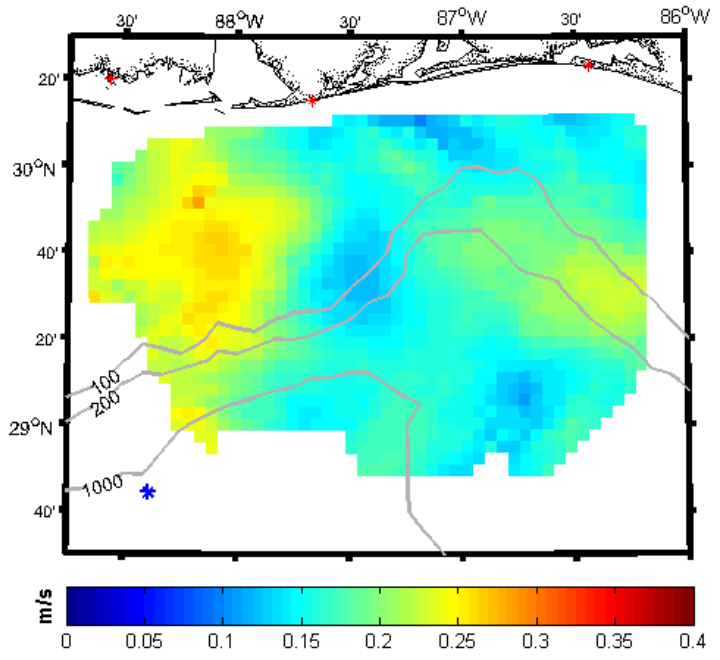

Figure 4.6. Mean amplitude of NDIOs from band-passed [0.85-1.15 cpd] HFR surface current velocities.

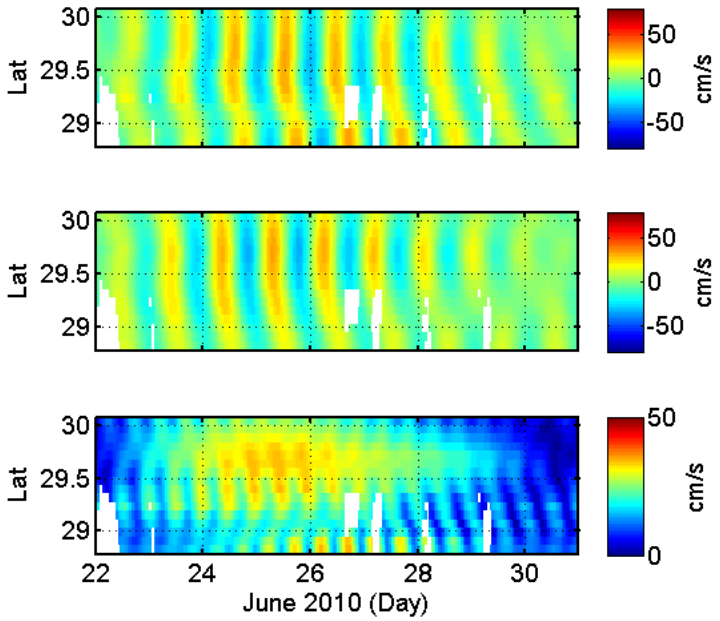

Figure 4.7. Hovmoller diagram of bandpassed [0.85 – 1.15 cpd] surface current velocities along longitude 88.1°W for the (top) ***u***-direction, (middle) ***v***-direction, and (bottom) magnitude.

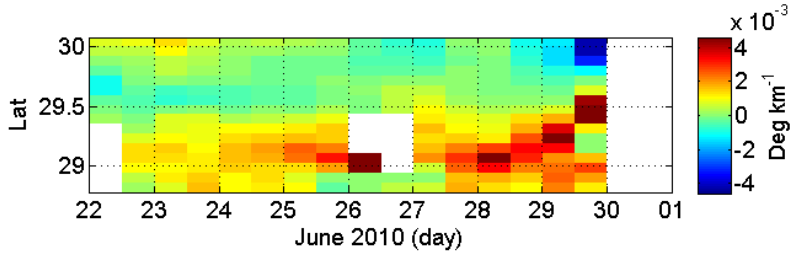

Figure 4.8. Hovmoller diagram of NDIO north-south phase gradient along the 88.1°W Longitude transect averaged over 12 hour sections of time from CW complex demodulation analysis.

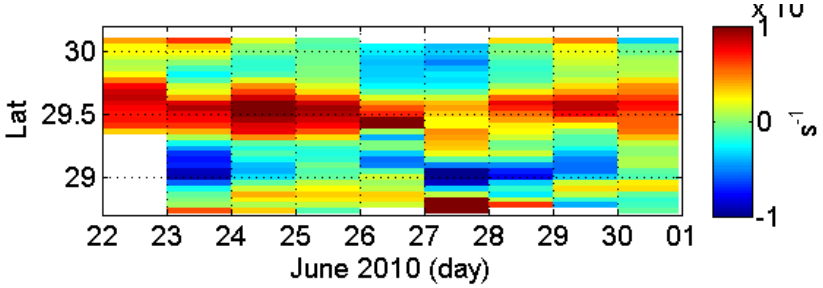

Figure 4.9. Daily averaged vorticity Hovmoller diagram along 88.1°W Longitude transect.

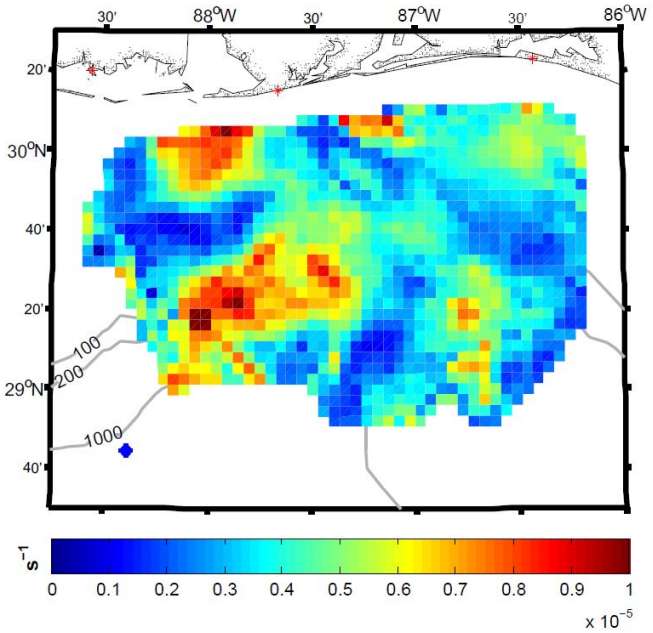

Figure 4.10. Mean amplitude of divergence oscillations from bandpassed [0.85 – 1.15 cpd] HF radar surface current velocities.

Chapter 5

Concluding Remarks

Although the investigated regions and phenomena in parts I and II are different, the underlying goal is the same. This goal is to contribute to the understanding of how near-surface ocean circulation disperses and mixes floating material such as pollutants, plankton, or algae in coastal regions. In part I the focus was on attracting LCSs which were used to describe the nature of near-surface trajectories in the dynamic upwelling environment off the California coast. Retention zones and regions of confluence were identified by the LCSs. In part II, regions of potentially enhanced vertical mixing were highlighted by spatiotemporal variability in the ubiquitous near-inertial oscillations in the northeastern Gulf of Mexico. It was speculated that the enhanced mixing by the near-inertial oscillations was generated by shear at the bottom of the mixed layer and pycnocline displacement caused by mixed layer oscillatory divergence. Another common thread between parts I and II was the implementation of HF radar to obtain near-surface current velocities. HF radar is a unique observational tool in that it provides a 2-D perspective of time-evolving near-surface currents. Additionally, near real time hourly HF radar data are currently available for a large portion of the coastal United States. The results described in this study can therefore be implemented in near real time applications in addition to scientific research.

References

Abascal, A. J., S. Castanedo, V. Fern, M. I. Ferrer, and R. Medina (2011), Oil Spill Trajectory Forecasting and Backtracking Using Surface Currents from high-frequency (HF) Radar Technology, paper presented at OCEANS 2011 IEEE - Spain, 6-9 June 2011.

Abascal, A. J., S. Castanedo, R. Medina, I. J. Losada, and E. Alvarez-Fanjul (2009), Application of HF Radar Currents to oil Spill Modelling, *Marine Pollution Bulletin*, *58*(2), 238-248, doi:http://dx.doi.org/10.1016/j.marpolbul.2008.09.020.

Ardhuin, F., L. Marie, N. Rascle, P. Forget, and A. Roland (2009), Observation and Estimation of Lagrangian, Stokes, and Eulerian Currents Induced by Wind and Waves at the Sea Surface, in *Journal of Physical Oceanography*, edited, pp. 2820-2838, American Meteorological Society, doi:10.1175/2009jpo4169.1.

Arthur, R. S. (1965), On the Calculation of Vertical Motion in Eastern Boundary Currents from Determinations of Horizontal Motion, *J. Geophys. Res.*, *70*(12), 2799-2803, doi:10.1029/JZ070i012p02799.

Austin, J. A., and S. J. Lentz (2002), The Inner Shelf Response to Wind-Driven Upwelling and Downwelling*, *Journal of Physical Oceanography*, *32*(7), 2171-2193, doi:10.1175/1520-0485(2002)032<2171:tisrtw>2.0.co;2.

Bakun, A., and C. S. Nelson (1991), The Seasonal Cycle of Wind-Stress Curl in Subtropical Eastern Boundary Current Regions, *Journal of Physical Oceanography*, *21*(12), 1815-1834, doi:10.1175/1520-0485(1991)021<1815:tscows>2.0.co;2.

Barrick, D. (1971), Dependence of second-order Doppler sidebands in HF sea echo upon sea state, paper presented at Antennas and Propagation Society International Symposium, 1971, Sep 1971.

Barrick, D. (1972), First-order Theory and Analysis of MF/HF/VHF Scatter from the Sea, *Antennas and Propagation, IEEE Transactions on*, *20*(1), 2-10, doi:10.1109/tap.1972.1140123.

Barrick, D., and B. Lipa (1979a), A Compact Transportable HF Radar System for Directional Coastal Wave Field Measurements, in *Ocean Wave Climate*, edited by M. Earle and A. Malahoff, pp. 153-201, Springer US, doi:10.1007/978-1-4684-3399-9_7.

Barrick, D. E., and B. J. Lipa (1979b), A Compact Transportable HF Radar System for Directional Coastal Wave Field Measurements, *Ocean Wave Climate*, *M.D. Earle and A. Malahoff (eds.), Plenum Press, New York*, 153-201.

Barth, J. A., S. D. Pierce, and R. L. Smith (2000), A Separating Coastal Upwelling Jet at Cape Blanco, Oregon and its Connection to the California Current System, *Deep Sea Research Part II: Topical Studies in Oceanography*, *47*(5â€“6), 783-810.

Beardsley, R. C., and S. J. Lentz (1987), The Coastal Ocean Dynamics Experiment Collection - an Introduction, *J. Geophys. Res.-Oceans*, *92*(C2), 1455-1463.

Berta, M., L. Ursella, F. Nencioli, A. M. Doglioli, A. A. Petrenko, and S. Cosoli (2014), Surface transport in the Northeastern Adriatic Sea from FSLE analysis of HF radar measurements, *Continental Shelf Research*, *77*, 14-23, doi:http://dx.doi.org/10.1016/j.csr.2014.01.016.

Breaker, L. (2005), Ocean Fronts off California: A New Product from GOES Satellite Data, *Sea Grant California: Coastal Ocean Research*.

Brink, K. H. (1983), The Near-surface Dynamics of Coastal Upwelling, *Progress in Oceanography*, *12*(3), 223-257, doi:http://dx.doi.org/10.1016/0079-6611(83)90009-5.

Brink, K. H. (1992), Cold-water filaments in the California Current System, *South Afr. J. Mar. Sci.-Suid-Afr. Tydsk. Seewetens.*, *12*, 53-60.

Brink, K. H., R. C. Beardsley, J. Paduan, R. Limeburner, M. Caruso, and J. G. Sires (2000), A View of the 1993–1994 California Current Based on Surface Drifters, Floats, and Remotely Sensed Data, *Journal of Geophysical Research: Oceans*, *105*(C4), 8575-8604, doi:10.1029/1999jc900327.

Brink, K. H., and T. J. Cowles (1991), The Coastal Transition Zone Program, *J. Geophys. Res.-Oceans*, *96*(C8), 14637-14647.

Capet, X. J., P. Marchesiello, and J. C. McWilliams (2004), Upwelling Response to Coastal Wind Profiles, *Geophysical Research Letters*, *31*(13), L13311, doi:10.1029/2004gl020123.

Carbajal, N., and T. Pohlmann (2004), Comparison Between Measured and Calculated Tidal Ellipses in the German Bight, *Ocean Dynamics*, *54*, 520-530.

Carter, G. S. (2010), Barotropic and Baroclinic M2 Tides in the Monterey Bay Region, *Journal of Physical Oceanography*, *40*(8), 1766-1783, doi:10.1175/2010JPO4274.1.

Castelao, R. M., T. P. Mavor, J. A. Barth, and L. C. Breaker (2006), Sea surface temperature fronts in the California Current System from geostationary satellite observations, *J. Geophys. Res.-Oceans*, *111*(C9), 13, doi:C09026 10.1029/2006jc003541.

Chapman, R. D., and H. C. Graber (1997), Validation of HF Radar Measurements, *Oceanography*, *10*(2), 76-79, doi:http://dx.doi.org/10.5670/oceanog.1997.28.

Chapman, R. D., L. K. Shay, H. C. Graber, J. B. Edson, A. Karachintsev, C. L. Trump, and D. B. Ross (1997), On the Accuracy of HF Radar Surface Current Measurements: Intercomparisons with Ship-based Sensors, *J. Geophys. Res.-Oceans*, *102*(C8), 18737-18748.

Chen, C. S., R. O. Reid, and W. D. Nowlin (1996), Near-inertial Oscillations over the Texas Louisiana shelf, *J. Geophys. Res.-Oceans*, *101*(C2), 3509-3524, doi:10.1029/95jc03395.

Chen, C. S., and L. Xie (1997), A Numerical Study of Wind-induced, Near-inertial Oscillations over the Texas-Louisiana Shelf, *J. Geophys. Res.*, *102*(C7), 15583-15593, doi:10.1029/97jc00228.

Cordero, S. G., B. K. Haus, and H. C. Graber (2009), Surface Signature of the Chesapeake Bay Outflow Variability Observed with Coastal Radar, *Journal of Coastal Research*, 1254-1263, doi:doi:10.2112/08-1027.1.

Coulliette, C., F. Lekien, J. D. Paduan, G. Haller, and J. E. Marsden (2007), Optimal Pollution Mitigation in Monterey Bay Based on Coastal Radar Data and Nonlinear Dynamics, *Environmental Science & Technology*, *41*(18), 6562-6572, doi:10.1021/es0630691.

D'Asaro, E. A. (1985), The Energy Flux from the Wind to Near-inertial Motions in the Surface Mixed Layer, *Journal of Physical Oceanography*, *15*(8), 1043-1059.

D'Asaro, E. A. (1995), Upper-Ocean Inertial Currents Forced by a Strong Storm. Part III: Interaction of Inertial Currents and Mesoscale Eddies, *Journal of Physical Oceanography*, *25*(11), 2953-2958, doi:10.1175/1520-0485(1995)025<2953:UOICFB>2.0.CO;2.

D'Asaro, E. A., C. C. Eriksen, M. D. Levine, C. A. Paulson, P. Niiler, and P. Van Meurs (1995), Upper-Ocean Inertial Currents Forced by a Strong Storm. Part I: Data and Comparisons with Linear Theory, *Journal of Physical Oceanography*, *25*(11), 2909-2936, doi:10.1175/1520-0485(1995)025<2909:UOICFB>2.0.CO;2.

Daddio, E., W. J. Wiseman, and S. P. Murray (1978), Inertial Currents Over the Inner Shelf Near 30°N, *Journal of Physical Oceanography*, *8*(4), 728-733, doi:10.1175/1520-0485(1978)008<0728:ICOTIS>2.0.CO;2.

Davies, A. M., and J. Xing (2003), On the Interaction Between Internal Tides and Wind-Induced Near-inertial Currents at the Shelf Edge, *Journal of Geophysical Research: Oceans*, *108*(C3), 3099, doi:10.1029/2002JC001375.

Davis, R. E. (1985), Drifter Observations of Coastal Surface Currents During CODE: The method and descriptive view, *Journal of Geophysical Research: Oceans*, *90*(C3), 4741-4755, doi:10.1029/JC090iC03p04741.

Dietrich, J. C., et al. (2012), Surface Trajectories of Oil Transport along the Northern Coastline of the Gulf of Mexico, *Continental Shelf Research*, *41*, 17-47, doi:10.1016/j.csr.2012.03.015.

DiMarco, S. F., M. K. Howard, and R. O. Reid (2000), Seasonal Variation of Wind-Driven Diurnal Current Cycling on the Texas-Louisiana Continental Shelf, *Geophysical Research Letters*, *27*(7), 1017-1020, doi:10.1029/1999gl010491.

Dorman, C. E., and C. D. Winant (1995), Buoy Observations of the Atmosphere Along the West-Coast of the United-States, 1981-1990, *J. Geophys. Res.-Oceans*, *100*(C8), 16029-16044.

Dzwonkowski, B., and K. Park (2012), Subtidal Circulation on the Alabama Shelf during the Deepwater Horizon Oil Spill, *J. Geophys. Res.-Oceans*, *117*, 15, doi:C03027 10.1029/2011jc007664.

Ekman, V. W. (1905), On the Influence of the Earth's Rotation on Ocean Currents, *Ark. Mat. Aston. Fys.*, *2*(11), 1-53.

Elipot, S., and R. Lumpkin (2008), Spectral Description of Oceanic Near-surface Variability, *Geophysical Research Letters*, *35*(5), L05606, doi:10.1029/2007GL032874.

Elipot, S., R. Lumpkin, and G. Prieto (2010), Modification of Inertial Oscillations by the Mesoscale Eddy Field, *Journal of Geophysical Research: Oceans*, *115*(C9), n/a-n/a, doi:10.1029/2009JC005679.

Emery, W. J., and R. E. Thomson (2001), Chapter 5 - Time-series Analysis Methods, in *Data Analysis Methods in Physical Oceanography*, edited by W. J. E. E. Thomson, pp. 371-567, Elsevier Science, Amsterdam, doi:http://dx.doi.org/10.1016/B978-044450756-3/50006-X.

Flament, P., L. Armi, and L. Washburn (1985), The Evolving Structure of an Upwelling Filament, *J. Geophys. Res.*, *90*(C6), 11765-11778, doi:10.1029/JC090iC06p11765.

Fontana, R. (2013), Physical Processes and their Influence on Zooplankton Composition and Foraging Opportunities for Seabirds in a Strong, Persistent Upwelling Region: Gulf of the Farallones-Cordell Bank (California), 143 pp, UC Davis, Bodega, CA.

Foo, E. C. (1981), A Two-Dimensional Diabatic Isopycnal Model;Simulating the Coastal Upwelling Front, *Journal of Physical Oceanography*, *11*(5), 604-626, doi:doi: 10.1175/1520-0485(1981)011%3C0604:atddim%3E2.0.co;2.

Fu, L. L. (1981), Observations and Models of Inertial Waves in the Deep Ocean, *Reviews of Geophysics*, *19*(1), 141-170.

García-Reyes, M., and J. Largier (2012), Observations of Increased Wind-driven Coastal Upwelling off Central California, *J. Geophys. Res.*, *115*(C4), C04011, doi:10.1029/2009jc005576.

Garrett, C. (2001), What is the "Near-Inertial" Band and Why Is It Different from the Rest of the Internal Wave Spectrum?, *Journal of Physical Oceanography*, *31*(4), 962-971, doi:10.1175/1520-0485(2001)031<0962:WITNIB>2.0.CO;2.

Garrett, C., and W. Munk (1972), Oceanic Mixing by Breaking Internal Waves, *Deep Sea Research and Oceanographic Abstracts*, *19*(12), 823-832, doi:http://dx.doi.org/10.1016/0011-7471(72)90001-0.

Gildor, H., E. Fredj, J. Steinbuck, and S. Monismith (2009), Evidence for Submesoscale Barriers to Horizontal Mixing in the Ocean from Current Measurements and Aerial Photographs, in *Journal of Physical Oceanography*, edited, pp. 1975-1983, American Meteorological Society, doi:10.1175/2009jpo4116.1.

Gonella, J. (1972), A Rotary-component Method for Analysing Meteorological and Oceanographic Vector Time Series, *Deep Sea Research and Oceanographic Abstracts*, *19*(12), 833-846, doi:http://dx.doi.org/10.1016/0011-7471(72)90002-2.

Gough, M. K., N. Garfield, and E. McPhee-Shaw (2010), An Analysis of HF Radar Measured Surface Currents to Determine Tidal, Wind-forced, and Seasonal Circulation in the Gulf of the Farallones, California, United States, *J. Geophys. Res.-Oceans*, *115*, doi:C04019
10.1029/2009jc005644.

Gough, M. K., A. J. H. M. Reniers, J. H. MacMahan, and S. D. Howden (2016), Resonant Near-surface Inertial Oscillations in the Northeastern Gulf of Mexico, *Journal of Geophysical Research: Oceans*, n/a-n/a, doi:10.1002/2015JC011372.

Gouillon, F., S. L. Morey, D. S. Dukhovskoy, and J. J. O'Brien (2010), Forced Tidal Response in the Gulf of Mexico, *Journal of Geophysical Research: Oceans*, *115*(C10), C10050, doi:10.1029/2010JC006122.

Halle, C. M., and J. L. Largier (2011), Surface Circulation Downstream of the Point Arena Upwelling Center, *Continental Shelf Research*, *31*(12), 1260-1272.

Haller, G. (2002), Lagrangian Coherent Structures from Approximate Velocity Data, *Phys. Fluids*, *14*(6), 1851-1861, doi:10.1063/1.1477449.

Haller, G., and F. J. Beron-Vera (2012), Geodesic Theory of Transport Barriers in Two-Dimensional Flows, *Physica D: Nonlinear Phenomena*, *241*(20), 1680-1702, doi:http://dx.doi.org/10.1016/j.physd.2012.06.012.

Haller, G., and A. C. Poje (1998), Finite Time Transport in Aperiodic Flows, *Physica D*, *119*(3-4), 352-380, doi:10.1016/s0167-2789(98)00091-8.

Hamilton, P., T. J. Berger, J. J. Singer, E. Waddell, J. H. Churchill, R. R. Leben, T. N. Lee, and W. Sturges (2000), Desoto Canyon Eddy Intrusion Study; Final Report Volume I: Executive Summary. OCS Study MMS 2000-079, edited by M. M. S. U.S. Department of the Interior, Gulf of Mexico OCS Region, p. 37 pp., New Orleans, LA.

Harrison, C. S., and G. A. Glatzmaier (2010), Lagrangian Coherent Structures in the California Current System: Sensitivities and Limitations, *Geophysical & Astrophysical Fluid Dynamics*, *106*(1), 22-44, doi:10.1080/03091929.2010.532793.

Haus, B. K., H. C. Graber, L. K. Shay, and T. M. Cook (2003), Alongshelf Variability of a Coastal Buoyancy Current during the Relaxation of Downwelling Favorable Winds, *Journal of Coastal Research*, *19*(2), 409-420, doi:10.2307/4299181.

Haza, A., T. Özgökmen, A. Griffa, A. Molcard, P.-M. Poulain, and G. Peggion (2010), Transport Properties in Small-scale Coastal Flows: Relative Dispersion from VHF Radar Measurements in the Gulf of La Spezia, *Ocean Dynamics*, *60*(4), 861-882, doi:10.1007/s10236-010-0301-7.

He, R., and R. H. Weisberg (2002a), Tides on the West Florida Shelf, *Journal of Physical Oceanography*, *32*(12), 3455-3473, doi:10.1175/1520-0485(2002)032<3455:TOTWFS>2.0.CO;2.

He, R., and R. H. Weisberg (2002b), West Florida Shelf Circulation and Temperature Budget for the 1999 Spring Transition, *Continental Shelf Research*, *22*(5), 719-748, doi:http://dx.doi.org/10.1016/S0278-4343(01)00085-1.

Hendershott, M. C. (1973), Inertial Oscillations of Tidal Period, *Progress In Oceanography*, *6*(0), 1-27.

Hsueh, Y., and Y. Golubev (2001), A Numerical Model Calculation of the Flow in DeSoto Canyon in Response to Northerly Wind Bursts in Winter., *Gulf of Mexico Science*, *1*, 44-59.

Huh, O. K., W. J. Wiseman, Jr., and L. J. Rouse, Jr. (1981), Intrusion of Loop Current Waters Onto the West Florida Continental Shelf, *J. Geophys. Res.*, *86*(C5), 4186-4192, doi:10.1029/JC086iC05p04186.

Huyer, A., P. M. Kosro, J. Fleischbein, S. R. Ramp, T. Stanton, L. Washburn, F. P. Chavez, T. J. Cowles, S. D. Pierce, and R. L. Smith (1991), Currents and Water Masses of the Coastal Transition Zone off Northern California, June to August 1988, *J. Geophys. Res.*, *96*(C8), 14809-14831, doi:10.1029/91jc00641.

Hyder, P., J. H. Simpson, J. Xing, and S. T. Gille (2011), Observations over an Annual Cycle and Simulations of Wind-forced Oscillations near the Critical Latitude for Diurnal–inertial Resonance, *Continental Shelf Research*, *31*(15), 1576-1591, doi:http://dx.doi.org/10.1016/j.csr.2011.06.001.

Jarosz, E., Z. R. Hallock, and W. J. Teague (2007), Near-inertial Currents in the DeSoto Canyon region, *Continental Shelf Research*, *27*(19), 2407-2426.

Kaplan, D. M., C. Halle, J. Paduan, and J. L. Largier (2009), Surface Currents During Anomalous Upwelling Seasons off Central California, *J. Geophys. Res.-Oceans*, *114*, 17, doi:C1202610.1029/2009jc005382.

Kaplan, D. M., and J. Largier (2006), HF Radar-derived Origin and Destination of Surface Waters off Bodega Bay, California, *Deep-Sea Res. Part II-Top. Stud. Oceanogr.*, *53*(25-26), 2906-2930.

Kaplan, D. M., J. Largier, and L. W. Botsford (2005), HF Radar Observations of Surface Circulation off Bodega Bay (Northern California, USA), *Journal of Geophysical Research*, *110*, C10020, doi: 10010.11029/12005JC002959.

Kaplan, D. M., and F. Lekien (2007), Spatial Interpolation and Filtering of Surface Current Data Based on Open-boundary Modal Analysis, *J. Geophys. Res.-Oceans*, *112*(C12), 20, doi:C12007
10.1029/2006jc003984.

Kohut, J. T., and S. M. Glenn (2003), Improving HF Radar Surface Current Measurements with Measured Antenna Beam Patterns, *Journal of Atmospheric and Oceanic Technology*, *20*(9), 1303-1316, doi:10.1175/1520-0426(2003)020<1303:ihrscm>2.0.co;2.

Kunze, E. (1985), Near-Inertial Wave Propagation In Geostrophic Shear, *Journal of Physical Oceanography*, *15*(5), 544-565, doi:10.1175/1520-0485(1985)015<0544:NIWPIG>2.0.CO;2.

Kunze, E., and T. B. Sanford (1984), Observations of Near-Inertial Waves in a Front, *Journal of Physical Oceanography*, *14*(3), 566-581, doi:10.1175/1520-0485(1984)014<0566:OONIWI>2.0.CO;2.

Large, W. G., and S. Pond (1981), Open Ocean Momentum Flux Measurements in Moderate to Strong Winds, *Journal of Physical Oceanography*, *11*(3), 324-336, doi:10.1175/1520-0485(1981)011<0324:OOMFMI>2.0.CO;2.

Largier, J. L., et al. (2006), WEST: A Northern California Study of the role of Wind-Driven Transport in the Productivity of Coastal Plankton Communities, *Deep-Sea Res. Part II-Top. Stud. Oceanogr.*, *53*(25-26), 2833-2849.

Largier, J. L., B. A. Magnell, and C. D. Winant (1993), Subtidal Circulation over the Northern California Shelf, *J. Geophys. Res.-Oceans*, *98*(C10), 18147-18179.

Lekien, F., C. Coulliette, A. J. Mariano, E. H. Ryan, L. K. Shay, G. Haller, and J. Marsden (2005), Pollution Release Tied to Invariant Manifolds: A Case Study for the Coast of Florida, *Physica D: Nonlinear Phenomena*, *210*(1-2), 1-20, doi:http://dx.doi.org/10.1016/j.physd.2005.06.023.

Lentz, S. J. (1992), The Surfac Boundary-Layer In Coastal Upwelling Regions, *Journal of Physical Oceanography*, *22*(12), 1517-1539, doi:10.1175/1520-0485(1992)022<1517:tsblic>2.0.co;2.

Li, X., W. Pichel, P. Clemente-Colon, V. Krasnopolsky, and J. Sapper (1998), Validation of Coastal Sea and Lake Surface Temperature Measurements Derived from NOAA/AVHRR Data, in *Fifth International Conference on Remote Sensing for Marine and Coastal Environments*, edited, Research and Data Systems Corporation, San Diego, CA.

Lipa, B., B. Nyden, D. S. Ullman, and E. Terrill (2006), SeaSonde radial velocities: Derivation and internal consistency, Ieee-Inst Electrical Electronics Engineers Inc.

Liu, Y., R. H. Weisberg, C. R. Merz, S. Lichtenwalner, and G. J. Kirkpatrick (2010), HF Radar Performance in a Low-Energy Environment: CODAR SeaSonde Experience on the West Florida Shelf, *Journal of Atmospheric and Oceanic Technology*, *27*(10), 1689-1710, doi:10.1175/2010jtecho720.1.

Long, R. M. (2007), Surface Current Measurements During Safe Seas 2006: Comparison and Validation of Measurements from High-Frequency Radar and the Quick Release Environmental Buoy. Proceedings of the MTS/IEEE OCEANS'07 Conference, Vancouver, BC, Canada, October 2007

McWilliams, J. C., F. Colas, and M. J. Molemaker (2009), Cold Filamentary Intensification and Oceanic Surface Convergence Lines, *Geophysical Research Letters*, *36*(18), L18602, doi:10.1029/2009gl039402.

Millot, C., and M. Crépon (1981), Inertial Oscillations on the Continental Shelf of the Gulf of Lions—Observations and Theory, *Journal of Physical Oceanography*, *11*(5), 639-657, doi:10.1175/1520-0485(1981)011<0639:IOOTCS>2.0.CO;2.

Mooers, C. N. K. (1975), Several Effects of a Baroclinic Current on the Cross-stream Propagation of Inertial-internal Waves, *Geophysical Fluid Dynamics*, *6*(3), 245-275, doi:10.1080/03091927509365797.

Morey, S. L., J. J. O'Brien, W. W. Schroeder, and J. Zavala-Hidalgo (2002), Seasonal Variability of the Export of River Discharged Freshwater in the Northern Gulf of Mexico, paper presented at OCEANS '02 MTS/IEEE, 29-31 Oct. 2002.

Morey, S. L., W. W. Schroeder, J. J. O'Brien, and J. Zavala-Hidalgo (2003), The Annual Cycle of Riverine Influence in the Eastern Gulf of Mexico Basin, *Geophysical Research Letters*, *30*(16), n/a-n/a, doi:10.1029/2003gl017348.

Nencioli, F., F. d'Ovidio, A. M. Doglioli, and A. A. Petrenko (2011), Surface Coastal Circulation Patterns by in-situ Detection of Lagrangian coherent structures, *Geophys. Res. Lett.*, *38*(17), L17604, doi:10.1029/2011gl048815.

Niiler, P. P. (1969), On Ekman Divergence in an Oceanic Jet, *Journal of Geophysical Research*, *74*(28), 7048-&, doi:10.1029/JC074i028p07048.

Noble, M. A., and S. R. Ramp (2000), Subtidal Currents over the Central California Slope: Evidence for Offshore Veering of the Undercurrent and for Rirect, Wind-driven Slope Currents, *Deep Sea Research Part II: Topical Studies in Oceanography*, *47*(5-6), 871-906.

Ohlmann, C., P. White, L. Washburn, B. Emery, E. Terrill, and M. Otero (2007), Interpretation of Coastal HF Radar–Derived Surface Currents with High-Resolution Drifter Data, *Journal of Atmospheric and Oceanic Technology*, *24*(4), 666-680, doi:10.1175/JTECH1998.1.

Olascoaga, M. J. (2010), Isolation on the West Florida Shelf with Implications for Red Tides and Pollutant Dispersal in the Gulf of Mexico, *Nonlin. Processes Geophys.*, *17*(6), 685-696, doi:10.5194/npg-17-685-2010.

Olascoaga, M. J., F. J. Beron-Vera, L. E. Brand, and H. Koçak (2008), Tracing the Early Development of Harmful Algal Blooms on the West Florida Shelf with the Aid of Lagrangian Coherent Structures, *Journal of Geophysical Research: Oceans*, *113*(C12), n/a-n/a, doi:10.1029/2007jc004533.

Olascoaga, M. J., I. I. Rypina, M. G. Brown, F. J. Beron-Vera, H. Koçak, L. E. Brand, G. R. Halliwell, and L. K. Shay (2006), Persistent Transport Barrier on the West Florida Shelf, *Geophys. Res. Lett.*, *33*(22), L22603, doi:10.1029/2006gl027800.

Paduan, J. D., K. C. Kim, M. S. Cook, and F. P. Chavez (2006), Calibration and Validation of Direction-finding high-frequency Radar ocean Surface Current Observations, *IEEE J. Ocean. Eng.*, *31*(4), 862-875.

Paduan, J. D., and L. K. Rosenfeld (1996), Remotely Sensed Surface Currents in Monterey Bay from Shore-based Radar (Coastal Ocean Dynamics Applications Radar), *Journal of Geophysical Research*, *101*(C9), 20,699-620,686.

Pallàs-Sanz, E., T. M. S. Johnston, and D. L. Rudnick (2010), Frontal Dynamics in a California Current System shallow front: 1. Frontal Processes and Tracer Structure, *J. Geophys. Res.*, *115*(C12), C12067, doi:10.1029/2009jc006032.

Perkins, H. (1972), Inertial Oscillations in the Mediterranean, *Deep Sea Research and Oceanographic Abstracts*, *19*(4), 289-296, doi:http://dx.doi.org/10.1016/0011-7471(72)90022-8.

Perkins, H. (1976), Observed Effect of an Eddy on Inertial Oscillations, *Deep Sea Research and Oceanographic Abstracts*, *23*(11), 1037-1042, doi:http://dx.doi.org/10.1016/0011-7471(76)90879-2.

Pickett, M. H., and J. D. Paduan (2003), Ekman Transport and Pumping in the California Current based on the U.S. Navy's High-resolution Atmospheric Model (COAMPS), *Journal of Geophysical Research: Oceans*, *108*(C10), 3327, doi:10.1029/2003jc001902.

Platzman, G. W. (1972), Two-Dimensional Free Oscillations in Natural Basins, *Journal of Physical Oceanography*, *2*(2), 117-138, doi:10.1175/1520-0485(1972)002<0117:tdfoin>2.0.co;2.

Poje, A. C., et al. (2014), Submesoscale Dispersion in the Vicinity of the Deepwater Horizon Spill, *Proceedings of the National Academy of Sciences*, *111*(35), 12693-12698, doi:10.1073/pnas.1402452111.

Pollard, R. T. (1970), On the Generation by Winds of Inertial Waves in the Ocean, *Deep Sea Research and Oceanographic Abstracts*, *17*(4), 795-812, doi:http://dx.doi.org/10.1016/0011-7471(70)90042-2.

Pollard, R. T., and R. C. Millard (1970), Comparison between Observed and Simulated Wind-generated Inertial Oscillations, *Deep Sea Research and Oceanographic Abstracts*, *17*(4), 813-821, doi:http://dx.doi.org/10.1016/0011-7471(70)90043-4.

Poulain, P. M., D. S. Luther, and W. C. Patzert (1992), Deriving Inertial Wave Characteristics from Surface Drifter Velocities: Frequency Variability in the Tropical Pacific, *Journal of Geophysical Research: Oceans (1978–2012)*, *97*(C11), 17947-17959.

Rainville, L., and R. Pinkel (2004), Observations of Energetic High-Wavenumber Internal Waves in the Kuroshio, *Journal of Physical Oceanography*, *34*(7), 1495-1505, doi:10.1175/1520-0485(2004)034<1495:OOEHIW>2.0.CO;2.

Reid Jr, J. L. (1962), Observations of Inertial Rotation and Internal Waves, *Deep Sea Research and Oceanographic Abstracts*, *9*(7–10), 283-289, doi:http://dx.doi.org/10.1016/0011-7471(62)90011-6.

Reid, R. O., R. E. Whitaker, T. A, M. U. D. o. Oceanography, and U. S. A. E. W. E. Station (1981), *Numerical Model for Astronomical Tides in the Gulf of Mexico*, Texas A & M University, Department of Oceanography.

Reniers, A. J. H. M., J. H. MacMahan, F. J. Beron-Vera, and M. J. Olascoaga (2010), Rip-current Pulses tied to Lagrangian Coherent Structures, *Geophys. Res. Lett.*, *37*(5), L05605, doi:10.1029/2009gl041443.

Rotunno, R. (1983), On the Linear Theory of the Land and Sea Breeze, *Journal of the Atmospheric Sciences*, *40*(8), 1999-2009, doi:10.1175/1520-0469(1983)040<1999:otltot>2.0.co;2.

Roughan, M., N. Garfield, J. Largier, E. Dever, C. Dorman, D. Peterson, and J. Dorman (2006), Transport and Retention in an Upwelling Region: the Role of Across-shelf Structure, *Deep Sea Research Part II: Topical Studies in Oceanography*, *53*(25-26), 2931-2955.

Seim, H. E., B. Kjerfve, and J. E. Sneed (1987), Tides of Mississippi Sound and the Adjacent Continental Shelf, *Estuarine, Coastal and Shelf Science*, *25*, 143-156.

Shadden, S. C., F. Lekien, and J. E. Marsden (2005), Definition and Properties of Lagrangian Coherent Structures from Finite-time Lyapunov Exponents in Two-Dimensional Aperiodic Flows, *Physica D*, *212*(3-4), 271-304, doi:10.1016/j.physd.2005.10.007.

Shadden, S. C., F. Lekien, J. D. Paduan, F. P. Chavez, and J. E. Marsden (2009), The Correlation Between Surface Drifters and Coherent Structures Based on High-frequency Radar Data in Monterey Bay, *Deep Sea Research Part II: Topical Studies in Oceanography*, *56*(3-5), 161-172.

Simpson, J. H., P. Hyder, T. P. Rippeth, and I. M. Lucas (2002), Forced Oscillations near the Critical Latitude for Diurnal-Inertial Resonance, *Journal of Physical Oceanography*, *32*(1), 177-187, doi:10.1175/1520-0485(2002)032<0177:fontcl>2.0.co;2.

Smith, S. R., and G. A. Jacobs (2005), Seasonal Circulation Fields in the Northern Gulf of Mexico Calculated by Assimilating Current Meter, Shipboard ADCP, and Drifter Data Simultaneously with the Shallow Water Equations, *Continental Shelf Research*, *25*(2), 157-183, doi:http://dx.doi.org/10.1016/j.csr.2004.09.010.

Steger, J. M., F. B. Schwing, C. A. Collins, L. K. Rosenfeld, N. Garfield, and E. Gezgin (2000), The Circulation and Water Masses in the Gulf of the Farallones, *Deep Sea Research Part II*, *47*, 907-946.

Stewart, R. H., and J. W. Joy (1974), HF Radio Measurements of Surface Currents, *Deep Sea Research and Oceanographic Abstracts*, *21*(12), 1039-1049, doi:http://dx.doi.org/10.1016/0011-7471(74)90066-7.

Teague, W. J., H. W. Wijesekera, E. Jarosz, A. Lugo-Fernández, and Z. R. Hallock (2014), Wavelet Analysis of Near-inertial Currents at the East Flower Garden Bank, *Continental Shelf Research*, *88*(0), 47-60, doi:http://dx.doi.org/10.1016/j.csr.2014.06.013.

Wang, D.-P., L.-Y. Oey, T. Ezer, and P. Hamilton (2003), Near-Surface Currents in DeSoto Canyon (1997-99): Comparison of Current Meters, Satellite Observation, and Model Simulation, *Journal of Physical Oceanography*, *33*(1), 313-326, doi:10.1175/1520-0485(2003)033<0313:nscidc>2.0.co;2.

Webster, F. (1968), Observations of Inertial-period Motions in the Deep Sea, *Reviews of Geophysics*, *6*(4), 473-490, doi:10.1029/RG006i004p00473.

Weisberg, R. H., R. He, Y. Liu, and J. I. Virmani (2005), West Florida Shelf Circulation on Synoptic, Seasonal, and Interannual Time Scales, in *Circulation in the Gulf of Mexico: Observations and Models*, edited, pp. 325-347, American Geophysical Union, doi:10.1029/161GM23.

White, W. B. (1972), Doppler Shift in the Frequency of Inertial Waves Observed in Moored Spectra, *Deep Sea Research and Oceanographic Abstracts*, *19*(8), 595-600, doi:http://dx.doi.org/10.1016/0011-7471(72)90042-3.

Whitt, D. B., and L. N. Thomas (2014), Resonant Generation and Energetics of Wind-Forced Near-Inertial Motions in a Geostrophic Flow, *Journal of Physical Oceanography*, *45*(1), 181-208, doi:10.1175/JPO-D-14-0168.1.

Wing, S. R., L. W. Botsford, J. L. Largier, and L. E. Morgan (1995), Spatial Structure of Relaxation Events and Crab Settlement in the Northern California Upwelling System, *Mar. Ecol.-Prog. Ser.*, *128*(1-3), 199-211.

Wing, S. R., L. W. Botsford, S. V. Ralston, and J. L. Largier (1998), Meroplanktonic Distribution and Circulation in a Coastal Retention Zone of the Northern California Upwelling System, *Limnology and Oceanography*, *43*, 1710-1721.

Wright, G. (2008), Validation of High Rrequency Radar used in Ocean Surface Current Mapping via in-situ Drifting Buoys, 88 pp. pp, Naval Postgraduate School, Monterey.

Wyatt, L. (1986), The Measurement of the Ocean Wave Directional Spectrum from HF Radar Doppler Spectra, *Radio Science*, *21*(3), 473-485.

Xing, J., and A. M. Davies (2004), On the Influence of a Surface Coastal Front on Near-Inertial Wind-induced Internal Wave Generation, *Journal of Geophysical Research: Oceans*, *109*(C1), C01023, doi:10.1029/2003JC001794.

Yan, H., and R. A. Anthes (1987), The Effect of Latitude on the Sea Breeze, *Monthly Weather Review*, *115*(5), 936-956, doi:10.1175/1520-0493(1987)115<0936:teolot>2.0.co;2.

Young, W., and M. B. Jelloul (1997), Propagation of Near-inertial Oscillations through a Geostrophic Flow, *Journal of Marine Research*, *55*(4), 735-766.

Yuan, D. (2002), A Numerical Study of Barotropicly Forced Intrusion in DeSoto Canyon, *J. Geophys. Res.*, *107*(C2), 3010, doi:10.1029/2001jc000793.

Zelenke, B., M. A. Moline, G. B. Crawford, N. G. III, B. H. Jones, J. L. Largier, J. D. Paduan, S. R. Ramp, E. J. Terrill, and L. Washburn (2009), Evaluating Connectivity between Marine Protected Areas Using CODAR High-Frequency Radar, in *Oceans 2009, Marine Technology for Our Future: Global and Local Challenges*, edited, pp. 2261-2270.

Zhang, X., S. F. Dimarco, D. C. Smith Iv, M. K. Howard, A. E. Jochens, and R. D. Hetland (2009), Near-resonant Ocean Response to Sea Breeze on a Stratified Continental Shelf, *Journal of Physical Oceanography*, *39*(9), 2137-2155.

Zhang, X., D. C. Smith, S. F. DiMarco, and R. D. Hetland (2010), A Numerical Study of Sea-Breeze-Driven Ocean Poincare Wave Propagation and Mixing near the Critical Latitude, *Journal of Physical Oceanography*, *40*(1), 48-66, doi:10.1175/2009jpo4216.1.